
Extreme precipitation in Northern Italy: genesis, classification and predictability

Federico Grazzini



München 2021

Extreme precipitation in Northern Italy: genesis, classification and predictability

Federico Grazzini

Dissertation
an der Fakultät für Physik
der Ludwig–Maximilians–Universität
München

vorgelegt von
Federico Grazzini
aus Lucca

München, 10. Mai 2021

Erstgutachter: Prof. Dr. George C. Graig

Zweitgutachter: Prof. Dr. Volkmar Wirth

Tag der mündlichen Prüfung: 29. Juni 2021

Contents

Zusammenfassung	viii
Abstract	x
1 Introduction	1
1.1 Societal relevance of extreme precipitation events (EPEs)	1
1.2 Atmospheric processes generating clouds and precipitation	3
1.3 The Mediterranean: an extreme precipitation hot spot. Why?	5
1.4 Rossby waves	8
1.5 Rossby wave packets and severe weather	9
1.6 The EPE breakdown into its main atmospheric components	11
1.7 Atmospheric predictability	14
1.8 Summary and research goals	15
2 Data and Methods	17
2.1 Target domain	17
2.2 Warning areas and EPE definition	19
2.3 Datasets for atmospheric variables	19
2.3.1 ECMWF Era-Interim	20
2.3.2 ECMWF Era5	20
2.3.3 ECMWF EPS reforecast	21
2.3.4 Choice of the atmospheric predictors	21
2.3.5 Convective adjustment timescale computation	22
2.4 Machine Learning algorithm description	23
2.5 Statistical method and scores	23
2.5.1 Silhouette score (SIL)	23
2.5.2 Homogeneous sample selection	23
2.5.3 Statistical significance assessment	24
2.5.4 Normalised Precipitation Spread (NPS)	24
2.5.5 Potential Predictability Index (PPI)	24
2.6 Diagnosis of Rossby wave packet amplitude	24
2.7 PV tendency framework	25

3	Scientific publications	27
3.1	EPE systematic classification with machine-learning (Part I)	29
3.2	An archetypal EPE: The Piedmont 1994 case study	47
3.3	EPE Large-scale drivers and dynamical precursors (Part II)	61
4	EPE predictability	83
4.1	Potential predictability	83
4.2	Summary	86
5	Conclusions	89
5.1	EPE classification	90
5.2	The 1994 Piedmont flood	90
5.3	Dynamical precursors	91
5.4	Predictability	92
A	Appendix	95
A.1	Table of Warning Areas thresholds	95
A.2	List of benchmark cases	97
A.3	List of Abbreviations	100
	Bibliography	103
	Danksagung	111

List of Figures

1.1	Historical floods recorded in Europe	2
1.2	Example of flash flood in Genoa	5
1.3	Back-building quasi-stationary MCS	7
1.4	Jet streams and Rossby waves	10
1.5	Rossby wave packet dynamics	12
1.6	Atmospheric scales of motion	13
1.7	Rossby waves, moisture transport and EPEs	14
2.1	Target domain and warning areas	18
4.1	EPE Normalized Precipitation Spread	85
4.2	EPE predictability measured by potential predictability index	86
4.3	NPS spatial differences on Warning Areas	87

Zusammenfassung

Die Wettervorhersage ist eine grundlegende wissenschaftliche Herausforderung und für die Gesellschaft von großer Bedeutung. Die Vorhersage von Extremwetterereignissen ist eine der herausragenden Leistungen der Wissenschaft. Trotz des enormen Gesamtfortschritts der modernen Meteorologie kann die präzise Vorhersage bestimmter kritischer Phänomene, wie z. B. extremer Niederschläge, auch bei kürzeren Vorhersagezeiträumen noch unsicher sein. Diese Forschung zielt darauf ab, die relevanten atmosphärischen Prozesse für die Bildung von Extremniederschlägen zu identifizieren. Wir untersuchen die Beziehung zwischen vorhersagbarer großskaliger Dynamik, die die richtigen Bedingungen für die Bildung von Extremereignissen schafft, und schnellen kleinskaligen Prozessen, wie Konvektion, die die Vorhersagbarkeit schnell zerstören und eine Herausforderung für eine korrekte Vorhersage darstellen. Mit dem Ziel, gemeinsame dynamische Zustände zu identifizieren, haben wir eine systematische Untersuchung vieler (> 800) extremer Niederschlagsereignisse (EPEs) entworfen, die zwischen 1979 und 2015 in Nord- und Mittelitalien. Durch die optimale Kombination von ECMWF-Reanalysen meteorologischer Felder und hochaufgelöstem, gerastertem Tagesniederschlag (ARCIS) klassifizieren wir mit einem maschinellen Lernansatz extreme Niederschlagsereignisse in drei Kategorien (Cat1, Cat2, Cat3). Die Kategorien unterscheiden sich nicht nur lokal und spiegeln erfolgreich die Niederschlagsprozesse in der Region wider (frontaler und orographischer Niederschlag, frontaler Niederschlag und eingebettete tiefe Konvektion, tageszeitliche oder schwach erzwungene Konvektion), sondern auch in der dynamischen Entwicklung ihres Vorläufers: der atmosphärische Rossby-Welle und des zugehörigen Wellenpakets. Bisher ist dies der erste Versuch, EPEs nach physikalischen Prozessen zu klassifizieren und mit der Vorhersagbarkeit in Verbindung zu bringen. Wir zeigen, dass EPEs, die in Cat1 und Cat2 fallen, mit Wellenpaketen aus der oberen Atmosphäre, assoziiert sind, die sich aus entfernten Regionen ausbreiten, während bei EPEs in Cat3 lokale Instabilität dominiert. Die stärksten EPEs, die meist in Cat2 fallen, sind durch eine wiederkehrende dynamische Entwicklung gekennzeichnet, die aus einer erheblichen stromaufwärts gerichteten Wellenverstärkung im Nordatlantik besteht, die vermutlich auf diabatische Heizquellen zurückzuführen ist. Cat2-Ereignisse sind in der untersuchten Region besser vorhersagbar als gemäßigte Ereignisse, die in die beiden anderen Kategorien fallen. Dieses Ergebnis hat wichtige praktische Implikationen. Es zeigt, dass nicht alle extremen Niederschlagsereignisse den gleichen Grad an Vorhersagbarkeit haben. Die Unsicherheit hängt nicht von der Intensität des Phänomens ab, sondern von der jeweiligen dynamischen Entwicklung.

Abstract

Weather prediction is a fundamental scientific challenge and crucial to society. Predicting extreme weather events is one of the outstanding achievements of science. Despite the enormous progress made by modern meteorology, the precise prediction of certain critical phenomena, like extreme precipitation, can still be uncertain even at shorter time ranges. This research aims to identify the relevant atmospheric processes for the formation of extreme precipitation. We investigate the relationship between the predictable large-scale dynamics that create the right conditions for the genesis of extreme events, and fast small-scale processes, such as convection, which rapidly destroy predictability and pose a challenge for a correct forecast. In the aim to identify common dynamical states, we designed a systematic investigation on extreme precipitation events (EPEs), based on a very large number of episodes (> 800), which occurred between 1979 and 2015 in northern-central Italy, used as a test region. Through the optimal blending of ECMWF reanalysis of meteorological fields and high resolution gridded daily precipitation (ARCIS), we classify, with a machine learning approach, extreme precipitation events into three categories (Cat1, Cat2, Cat3). The categories do not only differ locally, successfully reflecting the precipitation processes on the region (frontal and orographic precipitation, frontal precipitation and embedded deep convection, diurnal or weakly forced convection), but also in the dynamical evolution of their precursor: the upper-level wave, and the associated wave packet. So far, this is the first attempt to classify EPEs on physical processes and make connections with predictability. We show that EPEs falling in Cat1 and Cat2 are associated with upper-level wave packets propagating from remote regions, while for EPEs in Cat3 local instability is dominating. The strongest EPEs, mostly populating Cat2, are characterised by a recurrent dynamic evolution consisting of a substantial upstream wave amplification in the N. Atlantic, arguably due to diabatic heating sources. Cat2 events are more predictable than moderate events falling into the other two categories in the region under investigation. This original result has important practical implications. It shows that not all extreme precipitation events have the same level of predictability. The uncertainty does not depend on the intensity of the phenomenon but on the particular dynamic evolution.

Chapter 1

Introduction

Just as water is fundamental to life, precipitation amount and distribution are largely driving society and ecosystems developments. Precipitation is a key component of the water cycle, and is main factor of recharge of the fresh water reserves of the planet. Human practices have evolved to fit the expected patterns of precipitation intensity, amount, and timing. Besides, runoff from heavy precipitation events shapes the landscape, as floods and flash floods modify the morphology of the land carving valleys and depositing sediment on floodplains. As human activities have continued to expand, more infrastructures has been built, especially in flat areas and flood plains, raising the risk exposure to extreme events. Accurate and timely prediction of high impact weather, and in particular, extreme precipitation events, is essential therefore to limit losses of life and property as well as a proper water resource management. Although predictability is fundamentally limited by the chaotic nature of the atmosphere, recent research in atmospheric dynamics has provided new insights into the processes the limit the accuracy of forecasts, still open questions remain how to improve the forecast of these critical events. This research aims to characterise different atmospheric processes which influence extreme precipitation elucidating the balance between large-scale and more predictable motions and fast processes acting at the local scale, which pose a challenge for a correct forecast.

1.1 Societal relevance of extreme precipitation events (EPEs)

The prediction of extreme precipitation is a fundamental scientific challenge and of key importance to society, not only for civil protection purposes but also for water management optimisation. Extreme weather events have become a leading research topic in many academic fields due to their significant impacts on populations and ecosystems as well as projections of their frequency increase in a changing climate (IPCC (2014), Chapter 14). Extreme precipitation presents a great concern because it can generate life-threatening floods and secondary hazards, including soil erosion, landslides, infrastructural damages, and urban flash flooding. In the European countries, the total reported economic losses

caused by weather extremes, over the period 1980-2017, amounted to approximately EUR 453 billion (in 2017 Euro values). The most expensive weather extremes in the EU Member States include the 2002 flood in Central Europe (over EUR 21 billion), the 2003 drought and heatwave (almost EUR 15 billion), and the 1999 winter storm Lothar and October 2000 flood in Italy and France, both EUR 13 billion (European Environment Agency, 2017). A comprehensive reconstruction of European floods carried out by Paprotny et al. (2018) from a database covering the period 1870-2016, encompassing 37 European countries, shows that more than half of the events occurred in only three countries, namely Italy (36%), Spain (15%) and France (10%) (Fig. 1.1). Floods characteristics are different across Europe. The same authors show that in southern Europe, flash floods constituted the majority of flood events, and were most prevalent between September and November. In central and western Europe, river floods were more frequent than flash floods, with flood losses concentrated between June and August. In northern Europe, floods were mostly caused by snow melt and rarely resulted in significant losses.

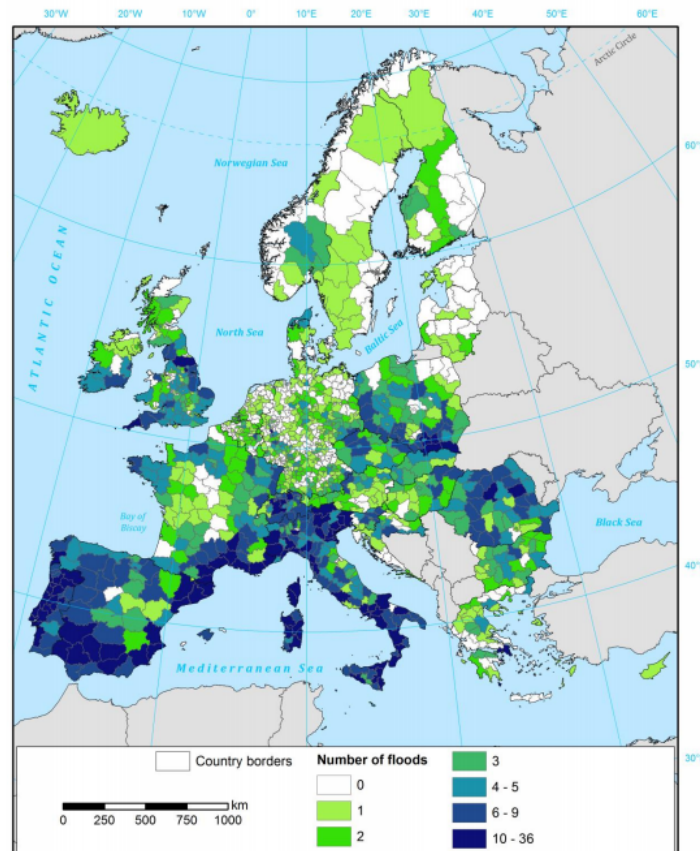


Figure 1.1: Total number of floods recorded in the HANZE database between (1870-2016). From Paprotny et al. 2018

We recall that a flash flood is caused by heavy rainfall in a short time, generally less than 6 hours, while river floods are caused by rising water on an existent watercourse due

to persistent rainfall over a large proportion of the river basin. The critical aspect for the former is intensity, while the latter is persistence and large spatial extent. The typology and seasonality of floods in Europe are hinting therefore to a different meteorological forcing. Different precipitation distribution is producing different hydrological response; fast, unpredictable and localised in case of heavy rain and flash floods typical of summer months, more predictable and slowly evolving, in for winter cases associated with fronts and mid latitude cyclones . Forecasting strategies have to correctly handle this different typology of phenomena, and the related uncertainties, to be effective. The main challenge of this work is to investigate a statistically significant number of extreme precipitation events (EPEs), defined as the highest percentile of daily precipitation (see section 2.2 for an exact definition), to gain insights on the dynamical reasons and consequences of their differences. For this purpose, we decided to focus our study on northern and central Italy which is one of the areas of Europe with the highest frequency of EPEs (Isotta et al., 2014) and with a good mixture of events typology. As a reflection of different precipitation regimes, Paprotny et al. (2018) show that Italy as a whole has 75% of floods which includes flash flood and the remaining 25% as river floods only. The choice of northern central Italy as study area permits therefore to assemble a significant large dataset of heterogeneous cases which allow a robust subdivision of cases in different categories.

1.2 Atmospheric processes generating clouds and precipitation

In this section, we briefly recall the main processes of cloud and precipitation formation. Cloud forms in the air which become saturated respect to liquid water or ice. Water vapour condensate (or brine) forming liquid droplets (or ice crystals) in suspension. Precipitation forms as smaller droplets coalesce with other rain drops or ice crystals within a cloud. Condensation is generally due to adiabatic expansion and cooling of air parcels during ascent.

Air parcels ascent can be obtained in different ways and each of them produces distinctive clouds forms and precipitation which can be grouped in three types :

- In the ascending branch of mid-latitude cyclones, as stable air masses are forced to rise along slantwise surfaces in association with synoptic fronts. *Stratiform clouds* are produced. Gentle vertical motions (order cm/s) responsible for condensation are related to large spatial (and temporal scales) and precipitation is usually widespread and continuous (several hours) of moderate to weak intensity
- Forced lifting of air as it passes over hills or mountains produces *orographic clouds*. Vertical velocities are tightly dependent upon the speed and direction of the horizontal flow impinging on the barrier and they can reach several m/s. Precipitation can be intense but typically restricted to the upwind side of the mountain barrier and up to the crest. Precipitation can last several hours or days according to the persistence of the flow.

- Strong local ascent occurs when warm air parcel becomes buoyant respect the surrounding atmospheric environment, that is when the atmosphere presents a vertically unstable stratification. In these conditions *convective clouds* are forming with updraft velocities in the order of 10m/s. Such clouds extend throughout the depth of the troposphere and coincide with vigorous condensation often leading to heavy precipitation. The strength of convection is proportional to the positive buoyant energy, usually defined as convective available potential energy (CAPE). However very often a stable layer close to the surface is present preventing convection. A convective inhibition (CIN) energy should be then overcome (by mechanical lifting or surface heating for example) to start convection. The lifetime of precipitation from a single convective cloud is generally less than 1 hour, however, in very unstable environment convective clouds tend to form clusters and organize in mesoscale convective systems (MCS) which can last longer and produce heavy precipitation for several hours.

An extreme precipitation event could be due to one or a mixture of the three types of processes, according to the different meteorological conditions. In all conditions necessary ingredients are upward vertical motions and steady moisture convergence able to sustain the condensation process for a sufficient period. In addition, also the microphysical properties which control the precipitation production efficiency ε are important. Following Loriaux et al. (2017), these components are conceptualized in the following approximation of the precipitation rate:

$$P \approx -\varepsilon \int_{z_t}^{z_b} w_c \frac{\partial q_{s,c}}{\partial z} \rho dz$$

This equation states that the precipitation rate P is determined by precipitation efficiency ε , times the vertically integrated condensation rate in the cloud. The condensation rate consists of a dynamic and thermodynamic contribution through the updraft velocity w_c and the vertical derivative of the saturation specific humidity $q_{s,c}$ following the parcel. Faster vertical velocities associated with convective systems will produce higher precipitation rates in thunderstorms, although more localized than in frontal structure. Forecasting experience shows that the maximum intensity of precipitation originating from stratiform precipitating systems, such as passing fronts, can reach 10 mm/h. In the case of intense interaction with orography, very rarely get to 30 mm/h (at our latitudes) for pure orographic mechanical uplift without the presence of convection. However, stratiform precipitation is more persistent and therefore can still generate significant event cumulative values. In the case of deep convection, instantaneous intensity of precipitation can reach higher values, order of few hundred mm/h, with hourly accumulations of more than 100 mm/h. The highest hourly rainfall ever recorded in Italy (and probably in Europe) is 181 mm/h, measured in the Genoa area during the devastating flash-flood of the 9 October 2014 (Poletti et al., 2017).

Since the interplay between the dynamic and thermodynamic component could generate events with very different properties, one of the main goal of this study is to design a method

to separate events with different precipitation characteristics and to evaluate the respective contribution of large-scale dynamics and local processes.

1.3 The Mediterranean: an extreme precipitation hot spot. Why?

The distinctive geographical location and the morphology of the Mediterranean basin make the region prone to heavy precipitation and flash floods. The Mediterranean Sea acts as a reservoir of the intense summer heat and as a moisture source from which convective and baroclinic atmospheric systems could draw their energy. The steep orography surrounding the sea favours the lifting of low-level moist airflow, enhancing precipitation. Typical of the Mediterranean climate is the very irregular distribution of precipitation through the year. Long periods of droughts (summer months) followed intense burst of precipitation, more frequent in autumn and winter. Accumulations of several hundred mm in 24h are possible as well as hourly values exceeding 100mm/h. The occurrence of these heavy precipitation amounts on small and steep river catchments often causes devastating flash floods, especially in the densely urbanised areas, as testify the example of Genoa, a city heavily exposed to this kind of events as documented in Fig. 1.2.



Figure 1.2: The Fereggiano stream rushing through streets of Genoa on the 4th of November 2011 after the precipitation on the nearby hills locally exceed 300mm/3h (Arpal Liguria, 2012)

In Autumn, the lowering in latitude of the Atlantic storm-track allows cold air to move on the warm Mediterranean Sea surface where usually an unstable stratification is still present. This is the perfect setting which trigger wide spread and intense precipitation due to the presence of both deep convection and stratiform precipitation falling from frontal systems. The highest peaks in precipitation are undoubtedly originated by quasi-stationary mesoscale convective systems (MCSs) which can occur in summer as isolated precipitation systems over land. Still, they become a more regular feature over sea and coastal regions at the end of summer and in Autumn, in association with an increase in frequency of synoptic upper-level waves. Convection can develop, in the ascending branch of an incoming trough, when a moist conditionally unstable marine boundary layer is advected inland and forced to ascend over the orography (Duffourg et al., 2018).

As examples of these situation characterised by persistent MCSs developing in a pre-frontal synoptic environment there are many cases reported in the literature: the dramatic flash-flood events in Vaison-la-Romaine in September 1992 (300 mm in 4 h; S en esi et al. (1996)), Piedmont in November 1994; (Buzzi et al. (1998)), Liguria in October and November 2011 (450–500 mm in 6–12 h; Rebora et al. (2013)), Gard in September 2002 (about 700 mm in 24 h; Delrieu et al. (2005)), and Valencia in November 1987 (more than 800 mm in 24 h; Romero et al. (2000)). These amounts are very significant if compared with the respective precipitation climatology. Each of these events alone correspond to one third up to half of all the rain that is falling in these location in an entire year.

A distinctive feature of Mediterranean convective systems, unlike in more continental areas, is their tendency to organise in quasi-stationary MCSs (Bluestein and Jain, 1985), with a characteristic V-shaped anvil signature in the infrared satellite images (Fig. 1.3a). These systems results from renewed convective development, or back-building, at the vertex of the V, which faces the low-level marine flow (Ducrocq et al., 2014).

The dynamical equilibrium between the slowly varying upper-level wave and MSCs is producing the ideal conditions which ensure continuous moisture convergence at the vertex of the convective system, where fast upward motions are located. The interaction between the upper-level flow and the local circulation in the storm with a constant renewal of convective cells at the same location, as illustrated in the schema of Figure 1.3b, could produce impressive precipitation amount for a prolonged time, even several hours. This interactions only occurs in specific dynamic conditions and it is extremely important to anticipate this dangerous phenomena recognizing those situations.

Water vapour flux convergence is also a crucial ingredient to attain extreme precipitation. The Mediterranean region is peculiar in this respect with the convergence of different sources of humidity. In the Autumn, the Mediterranean Sea is still warm with high evaporation rates which accounts for 40% to 60% of the water vapour feeding the convective systems Duffourg and Ducrocq (2013), Sodemann and Zubler (2010). The remaining moisture originates from the Northern Atlantic or transported from the subtropical Atlantic across North Africa (Turato et al., 2004). Winschall et al. (2014) have shown a great case to case variability in moisture supply for Mediterranean EPE. They show that water vapour coming from the North and subtropical Atlantic is a major contributor for stratiform precipitation, while Mediterranean moisture sources are more important for pure convective

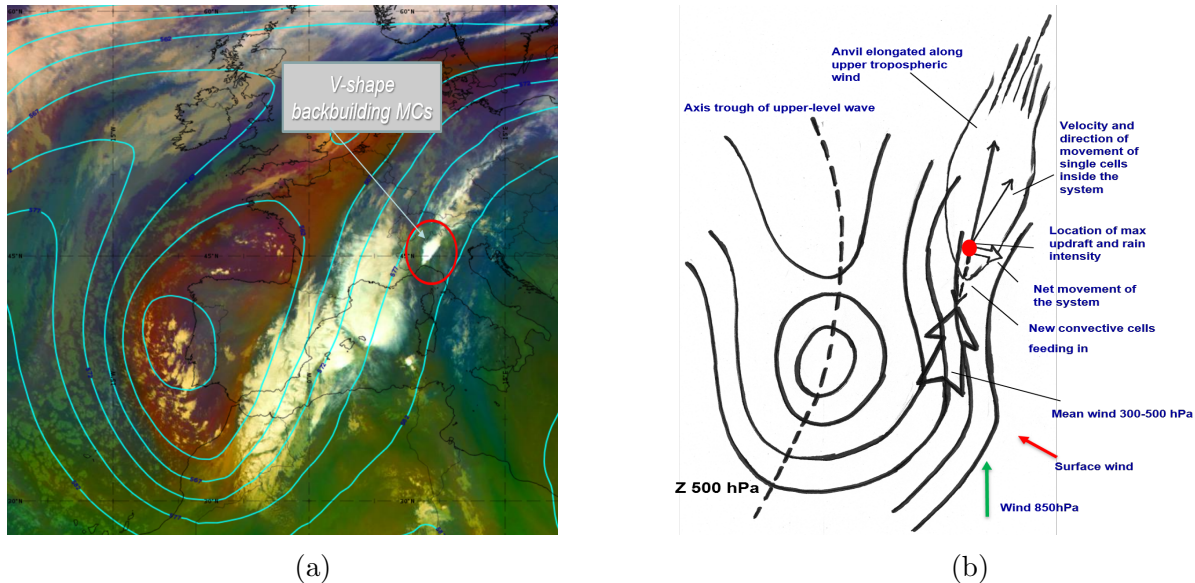


Figure 1.3: Panel (a) example of back-building quasi-stationary MCS developing in the warm air-mass ahead a large amplitude upper-level wave. Cyan isolines are geopotential heights at 500 hPa, while Meteosat-10 RGB composite is displayed in colours (reddish-purple indicating polar air, greenish colours showing subtropical air masses). The picture (courtesy of Eumetrain ePort-viewer), refers to 22-10-2019 00UTC when severe flash floods were reported between Liguria and Piedmont regions (N-Italy) due the MCS inside the red circle. More than 400mm in 12h were recorded at two observing stations of the regional networks. Panel (b) Schema of the genesis and maintenance of V-shape back building convective systems respect to the upper-level driving flow. The figure has been adapted by Grazzini F. and Selvini A. from MeteoFrance publication on Mediterranean convective systems (Rivrain, J.C. 1997)

events. The export of tropical moisture from subtropical Atlantic is reported to be relevant for extreme cases, as noted by Krichak et al. (2015).

Aiming at exploring the physical mechanisms beyond the formation of the extreme precipitation events in the Mediterranean area, among the most intense in the mid-latitudes, a number of international research projects and field campaign has been conducted over the years: the Mesoscale Alpine Program (MAP; Bougeault et al. (2001)) the Mediterranean Experiment (MEDEX, Jansa et al. (2014)) and Hydrological cycle in the Mediterranean Experiment (HyMEX), with a specific field campaign designed to improve the present state of knowledge of Mediterranean HPEs and flash-flooding events (Ducrocq et al., 2014).

Despite continuous improvements in the forecasts for such severe events the accuracy of the forecast is still partly insufficient compared to the actions required for effective warning procedures. Our ability to predict them remain limited because of the influence of processes occurring on fine scales or evolving fast, like convection, turbulence or microphysics. Non-linear interactions of these processes with the large-scale dynamics could play an important

role. Advances in the identification of the predominant mechanisms, and particularly of their interactions across scales, are desirable and could be obtained with the analysis of a large sample of cases. In that respect, the Mediterranean region, and in particular the Alpine area, with such high frequency of extremes offers a unique opportunity to build a very large dataset of EPEs which could be fundamental for understanding and improve our capabilities to predict these high-impact weather events.

1.4 Rossby waves

In the previous section, we discussed the characteristics of EPEs as local phenomena, often concentrated over small areas. However in many cases, they exhibit a tight connection with the state of the mid-latitude hemispheric flow, and in particular with its undulations or upper-level waves. Tropospheric upper-level waves are of paramount importance since they transfer energy, moisture and momentum across long distances, so they are also very relevant for EPE formation. Carl Gustav Rossby (1898-1957) derived its kinematic description for a barotropic fluid (density is function of pressure only) and therefore they are also named Rossby waves. We can discuss their property through its most straightforward formulation for a two dimensional inviscid flow of constant depth. Linearising the equation of motion (vorticity equation) around a basic state with a purely zonal flow of constant speed U , and assuming as a perturbation a comparably small plain wave, we can derive the dispersion relation for Rossby waves:

$$\omega = Uk - \frac{k\beta}{k^2 + l^2}$$

where ω is the frequency of the oscillation, β represents the northward gradient of the planetary vorticity $\partial f/\partial y$ ($f = 2\Omega \sin\varphi$ is the Coriolis parameter, Ω is the angular speed of rotation of the Earth, and φ is the latitude), k and l are the zonal and meridional wavenumbers (Vallis, 2017).

From the dispersion relation we compute the phase speed c_p^x and the group velocity c_g^x

$$c_p^x = \frac{\omega}{k} = U - \frac{\beta}{k^2 + l^2} \quad c_g^x = \frac{\partial\omega}{\partial k} = U + \frac{\beta(k^2 + l^2)}{(k^2 + l^2)^2} \quad (1.1)$$

Assuming a wave propagating only along the x-axis (zonal direction, $l = 0$) c_p^x reduce to :

$$c_p^x = U - \frac{\beta L^2}{4\pi^2}$$

where we substitute k with the wavelength $L = 2\pi/k$. From this equation we can easily see that Rossby waves moves eastward with the zonal flow, retarded by a combination of the rotation of the earth and the wavelength, more so the lower the latitude and the longer the wave. They tend therefore to move against the basic flow, which at upper-level in the mid-latitude is predominantly westerly. The larger is the advection of planetary vorticity (long

waves), the stronger is the tendency of the wave to *retrogress* respect the mean flow. Very long waves (planetary waves) in fact can remain stationary or even move westward, while smaller waves (transient synoptic waves, $L \approx 1000\text{km}$) usually move eastward.

The phase speed depends on of the horizontal wave number, meaning that Rossby waves are dispersive. In particular, from (1.1), we notice a very important property : $c_g^x > c_p^x$, the group velocity is higher than phase speed. This means that the envelope of Rossby waves moves eastward faster than individual troughs and ridges. Wave group energy flows faster than single waves along the tropospheric jet streams, giving rise to a very important concept in synoptic meteorology: the *downstream development* of new disturbances (Holton and Hakim, 2012). Due to downstream development, Rossby waves are often zonally confined (Chang, 1993), and they move in groups formed by a finite number of trough and ridges, which are often referred to as Rossby wave packets (RWPs). Although there is not a consistent terminology regarding different groups of atmospheric travelling waves, after Wirth et al. (2018), we will call Rossby wave trains the very low-frequency variety, composed by planetary waves with zonal wave numbers $s=1,2,3$, while we call RWPs the transient synoptic-scale variety, more relevant for our study.

In a more realistic description of 3D atmosphere, and with density which depends also on temperature and not only on pressure (baroclinic atmosphere), Rossby waves are *potential vorticity* conserving motion. The Rossby- Ertel Potential vorticity (PV) is a very relevant quantity in meteorology that essentially measures the ratio of the absolute vorticity $\zeta_a = \zeta_\theta + f$ (where ζ_θ is the vertical component of the relative vorticity on atmospheric parcel) to the effective depth of the vortex delimited by two isentropic (θ) surfaces, which can also be tilted, due to the horizontal gradient of the isentropes. It can be computed as:

$$PV = -g \frac{\partial \theta}{\partial p} \zeta_a$$

where g is the gravity acceleration, p is pressure, and θ is potential temperature. PV is a function of the absolute vorticity and the static stability ($-g \frac{\partial \theta}{\partial p}$) term. For adiabatic frictionless flow PV is invariant and can only be changed by diabatic processes. Rossby waves, in a baroclinic atmosphere, amplifies along a potential vorticity gradient.

1.5 Rossby wave packets and severe weather

Extreme weather and EPE are very often occurring in connection with Rossby waves (Boers et al., 2019), and the wave is often part of an RWP during its decay stage, as shown in the example displayed in Fig. 1.4. The significance of RWPs for weather forecasting is well recognised, and special attention is given to the role of these wave packets in the formation of high-impact weather events. Such interest arises from the hypothesis that weather events inherit predictability from large-scale dynamics, so understanding RWP could improve the prediction of severe weather and EPEs.

RWPs can be interpreted, in fact, as the large-scale carrier of meteorological activity, accounting, with their propagation, for a large part of the observed synoptic-scale and

lower-frequency variability of mid-latitude atmospheric circulation. It is still debatable if RWPs have to be treated as a physical entity or simply as a compact and idealised way to describe a succession of waves. Indeed, their identification and characterisation is a practical way to trace the transport of energy that connects successive weather systems (Persson, 2017). This implies that the RWP can be seen as a long-range precursor to the local extreme weather event. A link between transient RWPs and extreme weather, like surface cyclones, extreme temperatures; up to floods, precipitation and heavy snowfall has been documented by many authors and a full review of this dynamical linkage is described in Wirth et al. (2018). The specific connection between RWPs and EPEs over the Alpine area is also known and it has been investigated by several works e.g. Grazzini (2007); Martius et al. (2008); Nuissier et al. (2011).

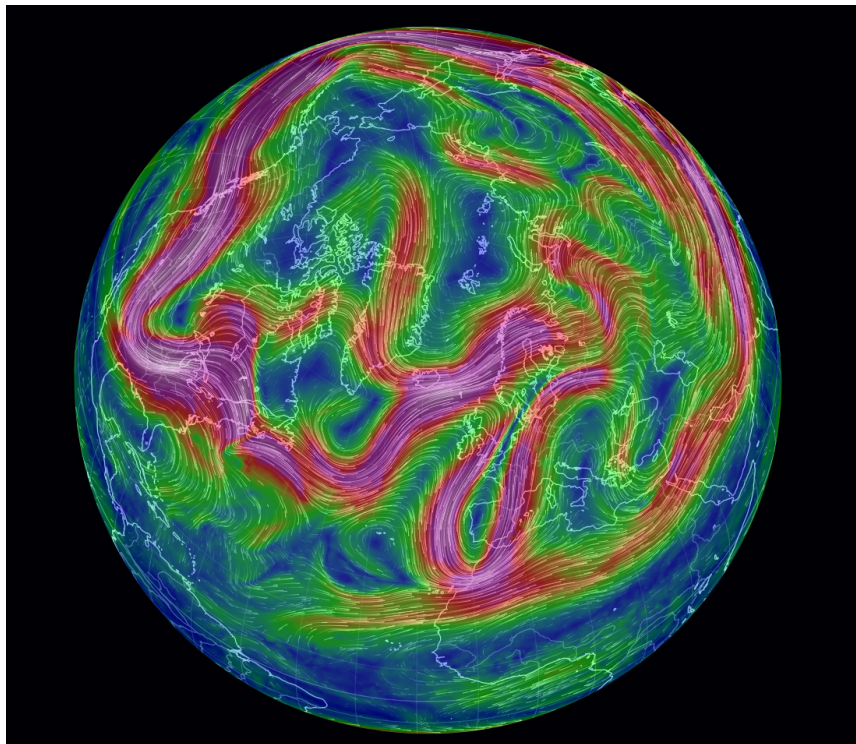


Figure 1.4: Wind streamlines at upper level (250 hPa) depicting the Rossby wave on the western Mediterranean on 22 October 2019 00UTC, the same date shown in figure 1.2.2. As can be seen, the wave, which is positioned almost at the end of a band of very high winds (which marks the polar jet), is relatively narrow and highly amplified, and it will soon break leading to a cut-off low of the Mediterranean. Courtesy of earth.nullschool.net

There are different types of RWPs associated with different spatio-temporal scales, a different type of forcing and properties of background flow. Sometimes RWPs are very short-lived and composed only by a wave couplet, or in other conditions, RWPs may last several days, propagating along great circles or channelled in the zonal direction in case of a strong jet. Wavelike disturbances are always present in the midlatitude atmosphere, but it

is only under particular and favourable atmospheric conditions that the RWPs can remain coherent for several days and connect remote regions of the atmosphere. The propagation and extension of RWPs are mostly controlled by the intensity and localisation of the large-scale background PV gradient, which acts as a waveguide (Wirth et al., 2018). Orlanski and Sheldon (1995) showed that ultimately the propagation of RWPs is maintained by energy extracted, through baroclinic conversion, from the mean flow available potential energy. In particular, strong baroclinic growth is observed in the centre of the wave packet where waves are mature. This energy is irradiated downstream through ageostrophic geopotential fluxes which are responsible for the downstream development of a new wave at the leading edge of the wave packet, as illustrated in Fig. 1.5. The propagation continues until the RWPs encounter a region of weakening background PV gradient which tends to produce a wave breaking and a termination of the storm track. Continental Europe and the Mediterranean are at the end of the storm track, and they are characterised by weaker baroclinicity compared with the Atlantic. However downstream development can force wave development in less baroclinic areas as often occur over the Mediterranean sea where cyclones development are part of the final stage of the Atlantic storm-track (Trigo et al. (1999), Rezaeian et al. (2016)). Finally, RWPs can be initiated by a variety of processes involving diabatic heating in the mid-lower troposphere, due, for example, to pre-existing synoptic disturbances such as extratropical cyclones, bursts of organised tropical convective systems associated with Madden-Julian Oscillation (MJO) propagation, flow distortion from orography, or recycling from previous waves in the jet-stream waveguide (Grazzini and Vitart, 2015).

1.6 The EPE breakdown into its main atmospheric components

The scientific challenge of weather forecast comes from the complex interactions of different physical processes and different scales of atmospheric motion that combine over thousands of kilometres and many days to produce a highly localised event such as an EPE. Forecasting the weather is like a tug of war between processes that are predictable against those which are unpredictable Bauer et al. (2015). Large-scale slowly evolving flow, anomalies in the ocean or in the soil state, can be predictable over many days and force the atmosphere towards a certain state, while on the opposite, convective situations dominated by fast processes, or turbulence can inject chaotic noise which propagate upscale and it can severely reduce predictability. For example Hohenegger et al. (2006) shows that the predictability of the three alpine heavy precipitation cases differs tremendously, ranging from highly predictable to virtually unpredictable.

This 'battle' has been schematized in Fig. 1.6 with the green arrow that represent the flow of energy propagating from the large-scales (say 1 day and with a length-scale greater than 1000km) to smaller scales, and upscale energy propagation, visualised by the orange arrow, with fast growing instabilities which reduce predictability. The position

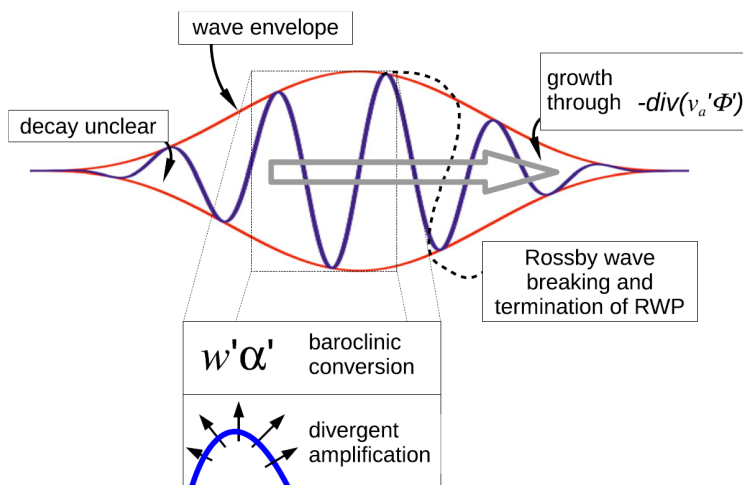


Figure 1.5: Schematic illustrating the processes that influence the propagation and dispersion of an RWP. The leading edge is dominated by the convergence of ageostrophic geopotential flux (grey arrow) from upstream mature system (downstream development). In the centre, the downstream ageostrophic flow is balanced by baroclinic growth and convergence of the ageostrophic geopotential flux from the upstream part. In the upstream part, there is a decay since the ageostrophic flux is not balanced anymore by the weaker baroclinic conversion. Courtesy of Wirth et al. 2018 (fig.9)

predictability barrier (indicated by the grey box), which is moving back or forward in every event, is the result of these opposite forces. A common approach to investigate the predictability of this complex phenomenon, as EPEs are, is to separate scales and try to identify recurring large-scale patterns for extreme event class, assuming that the large-scale controls the probability of occurrence of given extreme event (Messori et al., 2018).

The control of the large-scale on EPEs appears evident in many circumstances, and an association between a Rossby wave and heavy precipitation in the Alpine area has been previously identified by several authors (Massacand et al. (1998), Plaut and Simonnet (2001), Grazzini and Van der Grijn (2003)). In addition, Grazzini (2007) has shown that large-scale alpine precipitation events tend to be more predictable than average conditions, and the highest predictability is obtained when wave packets can propagate from far upstream, from the Pacific Ocean. In a recent paper, Vries (2020) shows that moisture availability (often analyzed in isolation) is strictly connected with the dynamics of Rossby waves in their breaking phase. Rossby wave breaking can initiate extreme precipitation events through steering intense moisture transport towards a given region in which the presence of orographic barriers or coastal boundaries could further enhance the response to the dynamic anomaly. The described interplay between upper-level wave, wave breaking and moisture transport is as nicely depicted in the schematic of Fig. 1.7, adapted from Vries (2020). The upper-level wave is defined by the 2 PV units (PVU) ($1\text{PVU} = 10^{-6}\text{Kkg}^{-1}\text{m}^2\text{s}^{-1}$) isoline, in blue. The circulation associated with the wave

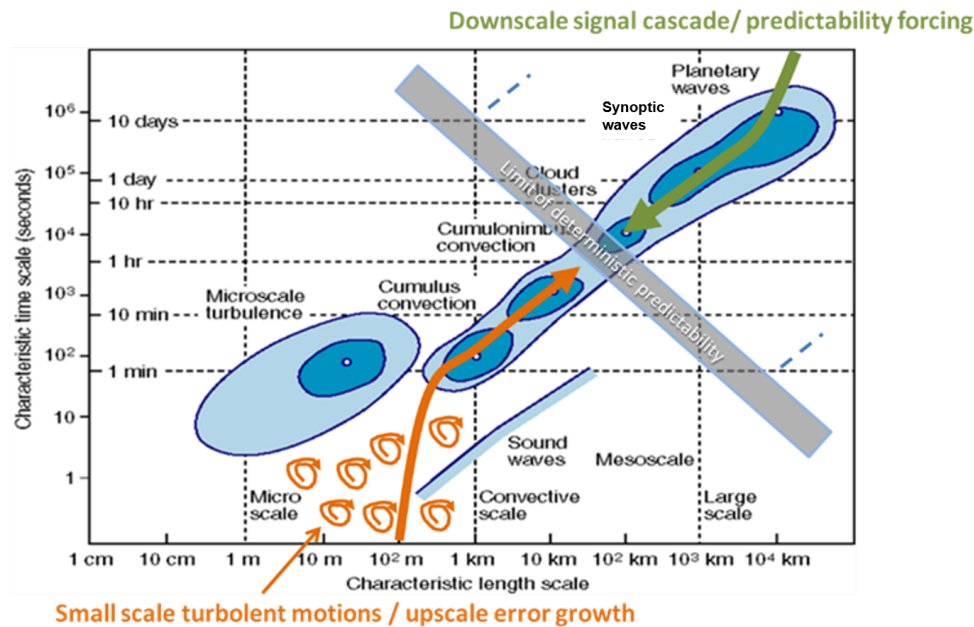


Figure 1.6: Schematic illustrating the main contrasting factors regulating predictability. Large-scale predictability forcing could be modulated by the presence of RWPs. Upscale error growth could be detected using the convective time scale.

produce a strong water vapour inflow in the ascending branch of the wave structure (green area), where typically are located rising motions due to upper-level divergence. The superposition of a strong water vapour flow in a dynamically active area creates the ideal conditions for the development of EPE, and even more is high orography is present. Vries (2020) shows in fact that Rossby wave breaking is associated with $> 90\%$ of EPEs near high topography and over the Mediterranean, whereas intense moisture transport is linked to $> 95\%$ of EPEs over many coastal zones. Combined Rossby wave breaking and intense moisture transport contributes up to 70% of EPEs.

This reinforces the hypothesis that EPEs are very tied to large scale dynamical "slow" evolution and a good prediction of Rossby waves and RWPs could lead to pre-warnings days ahead. However, detailed precipitation prediction, at a local scale, could remain uncertain even in the short-term due to intrinsic limitations introduced by upscale error growth from convective instability for example. Atmospheric flows are in fact characterised by both chaotic dynamics and recurrent large-scale patterns, or in other terms, this indicates the presence of atmospheric states close to an attractor. This may result in a reliable prediction of the severe weather synoptic pattern but in a still very uncertain precipitation localisation. For examples studies have shown the fast error growth due to the incorrect representation of Mesoscale Convective Systems (MCS) in the numerical weather prediction model, typically occurring over the US, could propagate along the waveguide to disrupt the forecast over Europe a few days later (Grazzini and Isaksen (2002), Rodwell et al. (2013), Parsons et al. (2019)).

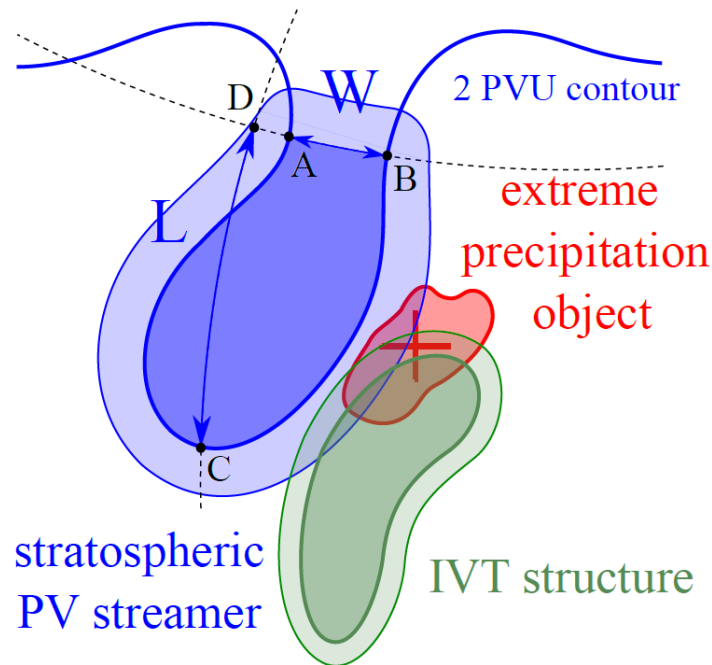


Figure 1.7: Schematic representation of Rossby wave breaking (upper tropospheric PV streamer in blue) and intense moisture transport (vertically integrated water vapour transport (IVT) in green) in a idealised synoptic-scale processes leading to EPE (read area). Adapted from De Vries, 2020

1.7 Atmospheric predictability

The predictability of weather is fundamentally limited by the chaotic nature of atmospheric motions (Lorenz, 1963) which are ranging across very different spatio-temporal scales. In addition to the accuracy of model representation, predictability depends on the precise knowledge of initial conditions on all scale of motions. Since it is not possible to determine the current state of the atmosphere exactly, small errors in unresolved motions can grow fast and contaminate the resolved scales after a finite amount of time (Lorenz, 1969a). That implies that there is an upper limit to the forecast skill, a limit beyond which the forecast error cannot get any smaller by improving the forecast system in all his components (data assimilation + model formulation). The limit of predictability will occur at a time when the error growth saturates and the predicted state deviates as much from the verifying state as a randomly selected, but dynamically and statistically possible state (Froude et al., 2013). For middle-atmosphere quantities like geopotential height of 500 hPa isosurface, in which most of the signal resides in the synoptic scale of motions, the upper limit of *potential predictability* has been estimated to be in the order of 15 days, as first proposed by Edward Lorenz in 1969. Research in this field has been consolidated since then, and yet it suggests

that the predictability limit for mid-latitude weather exist and is intrinsic to the underlying dynamical system, even if the forecast model and the initial conditions are nearly perfect. Currently, a skillful forecast lead time of mid-latitude instantaneous weather hardly goes beyond 10 days; a forecast time or *skill horizon* which can be considered as the *practical predictability* limit (Zhang et al., 2019).

However, predictability is highly regime dependent and different atmospheric variables have different forecast skill or *practical predictability* since they could be more or less sensible to instabilities in atmospheric processes. The prediction of precipitation amounts is influenced by many atmospheric processes ranging from the large scale, to the meso and convective scale, and including micro-physic and cloud dynamics. Precipitation reflects highly localized processes exhibiting large spatial variability. Its predictability is also highly sensitive to the nature dominant process involved, with weakly forced convective cases being very difficult to predict even at short range (Keil et al., 2020).

The prediction of precipitation is therefore still challenging with a practical predictability well below the 10 day limit. This sensitivity of predictability is even more critical in case of EPE. For example the probabilistic skill of direct grid-point precipitation, is about 2 day (global average) for high precipitation thresholds indicative of extreme events (Hewson and Pilloso, 2020) while the average skill over Europe computed over all precipitation events is about 4.5 days (ECMWF operational verification page, SEEPS score Rodwell et al. (2010)). For Italy a detailed verification of precipitation forecasts in the ECMWF high resolution run and COSMO local area model is carried out every season by ARPAE, using the dense network of precipitation observation as a reference. These routine verification also reveal that a useful skill in precipitation (Threat Score greater than 0.5) can be achieved only 1 to 2 days in advance for high thresholds representative of EPEs (e.g. greater than 20mm/24 for an area average) and limited to winter and autumn. However, in spring and especially in summer the skill horizon of the aggregated precipitation forecast is even shorter due to the prevailing convective nature.

1.8 Summary and research goals

A deeper understanding of how the large-scale predictable atmospheric motions regulates local dynamics and precipitation processes is fundamental to make significant progress in extreme precipitation and flood forecasting. An association between a Rossby wave and heavy precipitation in the Alpine area have been previously identified by several authors, assuming that EPEs are very tied to large-scale dynamical evolution. However in previous studies no difference was made on the type of extreme precipitation assuming the same linkage between the large-scale and precipitation occurred in each event. In reality, forecasting experience and analysis of cases studies shows that there is a large case to case variability and this linkage may change dramatically, according for example with the presence of convection and local forcing.

With this study we want to fill this gap, carrying out a more systematic investigation, on many heterogeneous cases. In particular we focus on the relationship between the pre-

dictable large-scale dynamics that create the right conditions for the genesis of extreme events, and fast small-scale processes, such as convection, which rapidly destroy predictability and pose a challenge for a correct forecast. In doing so we want also to take in account for different kind EPEs which may be characterized by different dynamical evolution and linkage with local scale processes. This effort to break down a complex sequence of events in a few defined processes could improve our understanding of the main drivers, and it pose the basis for a predictability estimate based on the processes. This would represent a major step forward in the practice of weather forecasting since the current estimate of uncertainty, based on a numerical approach (running many slightly perturbed simulations), it not conveying to the forecast user the reason (dynamical process) of the uncertainty.

To achieve this goal, we rely on a large data set of heavy precipitation events, more than 800 between 1979 and 2015. A target region of Northern-Central Italy has been chosen due to the relative high frequency of EPEs and the availability of high-resolution gridded observational dataset. The first step was to design an original and objective method to classify EPEs according to the different atmospheric setting and processes in which they originate. This classification, which will be addressed in the first scientific paper included in this dissertation will serve as the backbone for the rest of project and it is instrumental to the hypothesis that different categories of extremes exhibit different predictability according to the driving processes. The second scientific papers will describe a case study as an exemplary case of one of the three categories of EPE found. The detailed analysis of different large-scale evolution leading to EPEs is discussed in the third paper. Finally, the predictability dependencies on the EPE category and the relative large-scale patterns are discussed in Chapter 4.

Chapter 2

Data and Methods

In this chapter we describe the datasets and the analysis methods used through the entire research project and in the scientific papers. We introduce the target domain and the homogeneous areas used to aggregate precipitation. Then we move on the reanalysis datasets, discussing the choice of the of atmospheric predictors for the characterization and classification of EPE. Moving on the description of the methods, we describe the machine learning algorithms used for EPE classification. Later we present the diagnostic of Rossby wave packets and the potential vorticity tendency framework used to study the dynamical precursors of EPE. Finally we define the predictability measures used to asses predictability and other statistical methods.

2.1 Target domain

As we discussed in the introduction, we focus our analysis to northern–central Italy, an area very prone to these phenomena with numerous cases documented and described in the literature. Isotta et al. (2014) show that this region is one of the areas in Europe with the highest fraction of high-intensity precipitation days compared to the total number of wet days. Fig. 2.1 describes the geographical features of the area under investigation as long as the areas used for precipitation averages. We choose to work with climatologically homogenous areas rather than regular boxes of fix dimension. This choice is physically motivated by a different response of precipitation processes respect to orography and region exposition to the dominant flow. The areas used for precipitation averaging are the warning areas defined by Italian Civil Protection (see next section for a definition) for northern and central Italy. Labels indicate the name of each warning area which is composed of an abbreviation of the administrative region followed by an alphanumeric code. The use of these areas, as units for precipitation averages, is also motivated by potentially easier transfer of outcomes of this research into operational forecast practices for warnings.

The blue rectangular box represents the target domain used for averaging upper-level atmospheric variables derived from atmospheric reanalyses. The target domain is larger compared with individual warning areas. The averaging of this larger domain is done to

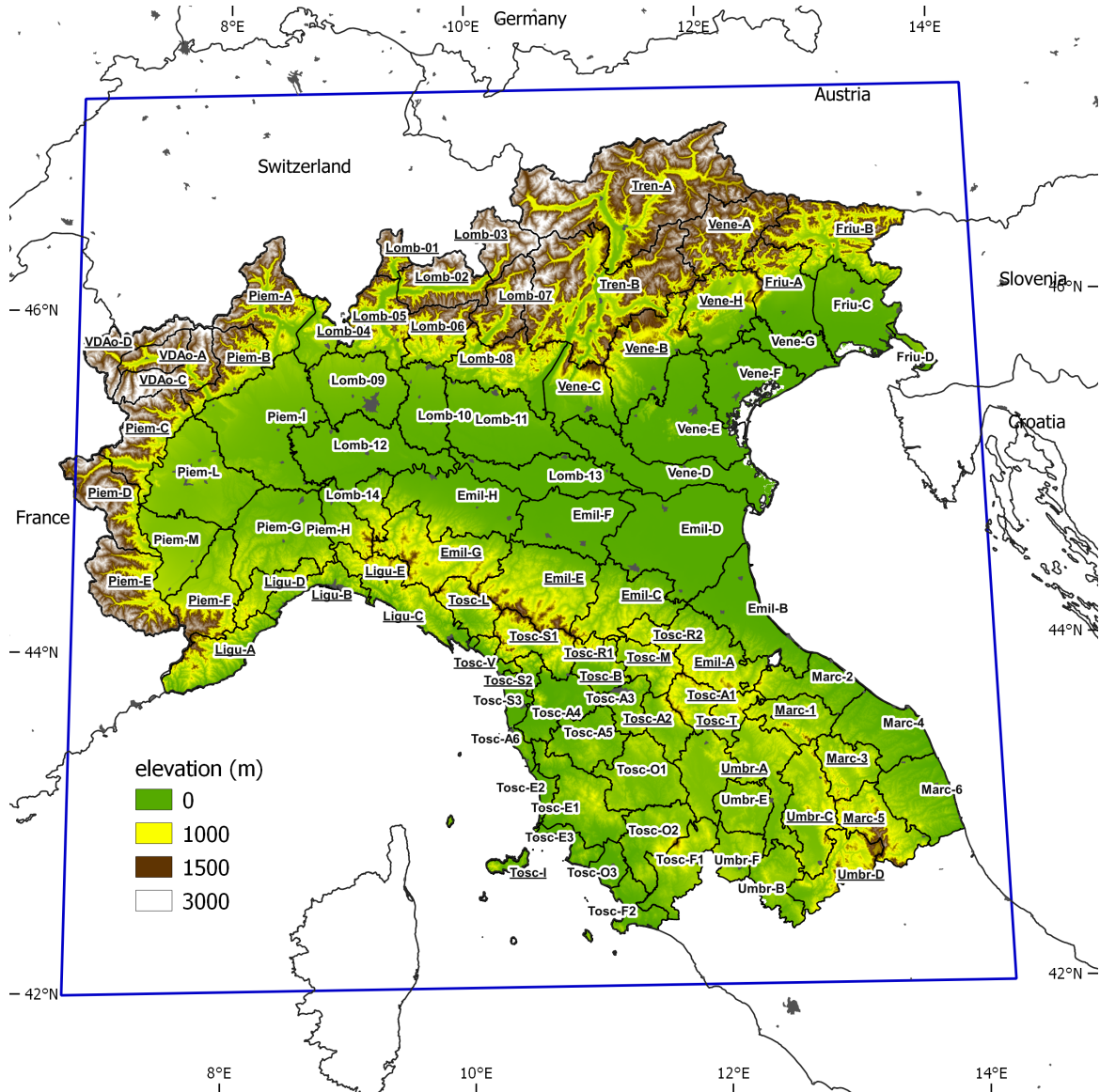


Figure 2.1: The figure shows the 94 warning areas of north-central Italy (as defined by Italian Civil Protection) used for precipitation averaging. Labels indicate the name of each warning area which is composed of an abbreviation of the administrative region followed by an alphanumeric code. Underlined names indicate areas characterised by significant orography (see the elevation legend). The blue rectangular box represents the target domain used for averaging atmospheric variables. Latitudes and longitudes for reference are included along the inner border of the figure

capture the synoptic scale component associated with EPEs, which we assume to present a smoother variation on that area on the timescale of one day. Our final goal in fact, is to study how the upper-level flow forcing could induce different precipitation characteristics at the surface, conditional on the dynamics and the thermodynamic stratification.

2.2 Warning areas and EPE definition

Since EPEs are at the core of our research project, it is essential to base our analysis on a high-density and reliable observational dataset covering a sufficient number of years to infer statistics of rare events. In that respect, the recently compiled ARCIS (Archivio Climatologico per l'Italia centro-Settentrionale, Climatological Archive for Central–Northern Italy) dataset appear the optimal choice. This is a gridded precipitation dataset (with a resolution of 5km) derived from 1,762 rain-gauges that belong to different networks of 11 Italian regions plus several stations of adjacent Alpine regions, recently assembled by the regional services (Pavan et al., 2019). The area covered is north-central Italy, at a daily temporal resolution for the period 1961–2015. Input data are checked for quality, time consistency, synchronicity, and statistical homogeneity. Data are spatially interpolated using a modified Shepard scheme. The 24h accumulation period follows the best practice of the Italian Hydrological Service reporting between 8 and 8 UTC of the following day.

Precipitation is aggregated over warning-area units (WA) provided by the Italian Department of Civil Protection, where they are used operationally for the national warning system. WAs are defined by a suitable aggregation of subregional hydrological basins. The goal is to obtain homogeneous areas with respect to the type and intensity of meteorological phenomena within a given territory. North-central Italy is subdivided into 94 WAs (see Fig. 2.1) with the naming convention being an abbreviation of the administrative region followed by an alphanumeric code. Their area extension ranges from the smallest domain in Tuscany of 192 km² (Tosc-S3) to the largest domain in Trentino Alto-Adige Alpine region of 7,398 km² (Tren-A). The mean area extension is 1,750 km². First, we compute the daily spatially average precipitation and spatial standard deviation for each WA for the period 1979–2015. Secondly, we compute precipitation percentiles considering wet days only (daily accumulation greater than or equal to 1 mm). EPEs are subsequently defined as days with daily precipitation greater than or equal to the 99th percentile across one or more WAs. A description of each area, including their precipitation percentiles value, is provided in Table S1 in the Appendix. Note that with this upscaling approach, we are implicitly disregarding localised events smaller than roughly 300 km².

2.3 Datasets for atmospheric variables

Above we have described the gridded precipitation dataset, here we introduce the datasets for the free atmosphere. Required atmospheric variables are obtained from reanalyses and reforecasts of the European Centre for Medium-range Weather Forecasts (ECMWF).

ECMWF uses its state of the art Integrated Forecast System (IFS), not only to provide member states with timely operational forecasting products, but also to reanalyse past observations. This complex data-assimilation procedure allow to create a global and homogeneous 3D description of the recent history of the atmosphere, land surface, and oceans. The IFS is a comprehensive and complex Earth-system model that includes a mathematical formulation of the atmospheric motions (momentum, thermodynamic and continuity equations) plus many parametrized physical processes like cloud microphysics, but also its chemical composition, the marine environment and land processes. Another fundamental part of the IFS is the data assimilation procedure. It is a sophisticated global variational procedure which is used to produce, using all available observations and previous short range forecast valid at a given time, the best possible estimate of the atmospheric state (initial conditions) to start the new forecast simulations. The combination of state of the art modelling and optimal use of historical observations make the reanalysed fields a very powerful tool for diagnostic and process studies, and key elements also to produce global climatologies. In the following sections, we are going to describe briefly the main dataset used.

2.3.1 ECMWF Era-Interim

ERA-Interim is a global atmospheric reanalysis that is available from 1 January 1979 to 31 August 2019. The data assimilation system used to produce ERA-Interim is based on a 2006 release of the IFS (Cy31r2). The system includes a 4-dimensional variational analysis (4D-Var) with a 12-hour analysis window. The spatial resolution of the data set is approximately 80 km (T255 spectral) on 60 levels in the vertical from the surface up to 0.1 hPa (Dee et al., 2011). We retrieved field at 6 h intervals, temporally accumulated to daily resolution and spatially averaged over a box covering north-central Italy (blu box in Fig. 2.1). ARCIS and ECMWF reanalysis datasets are used for the common period 1979–2015 ERA-Interim reanalysis was initially used in the first part of the work (Part I), in the classification algorithm, described in Chapter 3. Later an upgraded reanalysis was released by ECMWF, ERA5 (see next section for a description). We recomputed the classification with the new reanalysis. The EPE list and classification is essentially unchanged since it is based on area-averaged values and it is not sensitive to small local changes. ERA5 fields were used trough for all the rest of the study.

2.3.2 ECMWF Era5

ERA5 is the new global ECMWF reanalysis covering the period 1979- to within 5 days of realtime. The period will be further expanded in the past, starting from 1950 to real time. ERA5 provides hourly estimates of a large number of atmospheric, land and oceanic climate variables. The data cover the Earth on a 30km grid and resolve the atmosphere using 137 levels from the surface up to a height of 80km. ERA5 includes information about uncertainties for all variables at reduced spatial and temporal resolutions. It combines increased amounts of historical observations into global estimates using advanced modelling

and data assimilation systems. It was produced using 4D-Var data assimilation with IFS cycle CY41R2 the one introduced in operation in 2016. Vertical resolution is also increased to 137 hybrid sigma/pressure (model) levels in the vertical, with the top level at 0.01 hPa. The IFS is coupled to a soil model and an ocean wave model (Hersbach et al., 2020).

2.3.3 ECMWF EPS reforecast

For the evaluation of predictability we use a reduced version of the operation ensemble forecast, the so-called reforecast suite, designed to compute the model climatologies for the medium and long-range operational forecast. The ECMWF reforecast suite is based on an 11-member ensemble running biweekly for 46-day, with the latest IFS cycle (Vitart et al., 2019). Every Monday and Thursday the system is run on the same day and months of the past 20 years. For instance, if the starting date of the real-time forecast is 29 March 2021, the corresponding climatology is a 11-member ensemble starting on 29 March 2020, 29 March 2019, ..., 29 March 2002. The 11-member ensemble is thus integrated with 20 different starting dates (same day and month, but different years) producing about 220 runs for each given date. The re-forecast, being run operationally and archived since 2018, allows to cover EPE dates going back to year 2000. The combination of the availability of the re-forecast, which is bi-weekly, and the distribution of EPE from 2015 to 2000, gives a sample of between 30 and 40 cases, which is a just sufficient to base our statistic. Despite the limitation of not being available on a daily basis, which reduce the number of forecasts validating on a given date, this dataset allows comparing the predictability of past dates with an up to date and homogeneous forecasting system. If we had used the archived full operational ensemble we wouldn't be able to compare events belonging to different years since the average skill of the model has increased steadily from the early days of numerical weather prediction, roughly 1 day per decade (Bauer et al., 2015).

2.3.4 Choice of the atmospheric predictors

Since we propose an categorization method based on dynamic upper-air fields and the thermodynamic state, the choice of predictors representing these processes is critical. We select eight possible predictors which describe the EPE environment, including variables sensitive to flow conditions and variables representative of thermodynamic conditions. The choice has been made through a combination of established variables described in the literature or previous case-studies with predictors typically used by forecasters in their operational experience. Their names and abbreviations are listed and fully described in Table 1 below. In particular, the use of CAPE, the convective adjustment timescale τ (see section 2.4.1) and vertically integrated water vapour transport (IVT), accounting for water vapour fluxes (Lavers and Villarini, 2015), are already well establish in literature. In addition, Θ_{e850} and the total column water vapour (TCWV) are used for describing air-mass types. $\Delta\Theta_{e500-850}$ and BS500-925 (Bulk Shear) are also included, providing further information on the convective environment.

For each day in the 37-year period, spatial averages across the target domain are computed for these variables. Initial tests showed that maximum/minimum values for fields describing the convective environment have better discriminatory power than their mean daily values. Thus, maximum values of spatial averages of Tau, CAPE, BS500-925 and minimum values of $\Delta\Theta_{e500-850}$, all available at 6-hourly temporal resolution, are used instead of daily means.

TABLE 1 ERA-Interim variables chosen as predictors to represent the large-scale flow associated with EPEs. For each EPE day, variables are spatially averaged over the Target Domain and aggregated daily as reported in the table

Variable	Description	Units
Tau _{dmax}	Daily maximum of convective adjustment time-scale	h
CAPE _{dmax}	Daily maximum of CAPE	J/kg
IVTe	Daily mean of zonal component of integrated water vapour transport (surface up to 300 hPa)	kg m ⁻¹ s ⁻¹
IVTn	Daly mean of meridional component of integrated water vapour transport (surface up to 300 hPa)	kg m ⁻¹ s ⁻¹
θ_{e850}	Daily mean of equivalent potential temperature at 850 hPa	K
$\Delta\theta_{e500-850_dmin}$	Daily minimum of delta θ_e (500–850)hPa	K
TCWV	Daily mean of total column water vapour	kg/m ²
BS _{500_925_dmax}	Daily maximum of wind bulk shear 500–925 hPa	m/s

2.3.5 Convective adjustment timescale computation

The convective adjustment timescale (Tau) is used to discriminate between atmospheric states that differ by the rate of removal of conditional instability: equilibrium and non-equilibrium regimes (Done et al., 2006). In the equilibrium regime, the generation of CAPE is balanced by widespread convective heating associated with synoptic forcing, while in the non-equilibrium regime CAPE can rise to larger values since convection is limited by high convection inhibition (CIN) and its initiation is associated with local circulations in the boundary layer (weak large-scale forcing). Values between 3 and 12h can be used as a threshold to discriminate between these regimes with a value of 6 h mostly used (Molini et al. (2011);Keil et al. (2014);Kober et al. (2014)). Following Zimmer et al. (2011), Tau is computed as

$$Tau = \frac{1}{2} \frac{C_p \rho T_0}{L_v g} \frac{CAPE}{P}$$

at 3 h intervals and averaged over the target domain. The first part of the equation is constant: L_v is the latent heat of vaporization, ρ is the air density, C_p the specific heat at constant pressure, g the acceleration of gravity and T_0 a reference temperature. $CAPE$ and precipitation P are time dependent and are extracted from short-term forecasts of ERA-Interim at 3 h intervals since these are not analysed fields. P is divided accordingly to obtain hourly precipitation rates needed for the computation. We omit grid-points with hourly rain rates lower than 0.2 mm/h. This empirically determined threshold allows a good balance between avoiding very low intensities that would produce spurious high values of Tau , and providing enough data points for a robust estimate. The domain-averaged Tau is set to zero if there are less than 10% precipitating grid points.

2.4 Machine Learning algorithm description

The machine-learning classification is performed using modules of the Scikit-Learn library written in Python (Pedregosa et al., 2011). In particular, based on the set of eight predictors, we use the Kmeans method of the `sklearn.cluster` module to classify EPEs in three categories. Kmeans clustering is an unsupervised machine learning algorithm. In contrast to traditional supervised machine learning algorithms, Kmeans attempts to classify data without having first been trained with labeled data. The algorithm assigns every data point to one of the K predefined groups (3 in our case) following a minimization, in multidimensional space, between cluster centroid and points. To check whether it is possible to reduce the number of predictors, we use the `RandomForestClassifier` (`sklearn.ensemble` module) to simulate the classification obtained by Kmeans. This ensemble learning method fits a number of decision trees (in our case 100 estimators or trees) to various sub-samples of the dataset and uses averaging to improve the accuracy. In this way, through the feature importance, we can estimate the sensitivity of Kmean classification with respect to chosen predictors and then re run the Kmean without the unnecessary predictors (those with a low feature importance). Essentially these two algorithm are applied in a two step method with the `RandomForestClassifier` which help to refine the Kmeans classification.

2.5 Statistical method and scores

2.5.1 Silhouette score (SIL)

As an objective metric to judge the cluster separation into three categories, we used the Silhouette score (SIL), implemented in the `silhouette score` method part of the `Sklearn` metrics module. This score measures, along each dimension (i.e. each predictor in a normalised space), how tightly the events are grouped inside each cluster (cohesion) compared to the remaining clusters (separation). It ranges from -1 (wrong clustering) to 1 (fully separated clusters) with values equal to 0 indicating that a given element has the same distance from the other cluster centroids (overlapping). The Silhouette score is computed for all classification methods and averaged over all elements falling in each category.

2.5.2 Homogeneous sample selection

Given that the EPE sample size in the three categories is not equal (361, 344, and 182 cases in category 1, 2, and 3, respectively), for the purpose of comparison, a sample of 100 events in each category is selected. The selection of the 100 representative cases is slightly different through the study. In the classification part (Part I) the selection is based on the top 100 ranking events in each category based on the Silhouette score. While in the study of the dynamic precursors, before ranking according to SIL, we selected only independent events. For events that lasted for more than one day, we only consider the first day. In addition, if two events are not at least 3 days apart, we discard the second one so that

the events we consider are to some extent meteorologically independent. From the filtered samples, we then select the 100 most representative ones of each EPE category based on a SIL ranking. This modified selection removes approximately 10% of the EPEs that were identified in Part I.

2.5.3 Statistical significance assessment

Statistical significance in the composite maps and Hovmöller diagrams is assessed using a Monte Carlo approach (Martius et al., 2008). In particular, the value at a grid point is statistically significant at the $\alpha=0.10$ level, if it belongs to the highest or lowest 5% tail of a distribution created by reconstructing the mean 300 times using random selections of an equal number of dates.

2.5.4 Normalised Precipitation Spread (NPS)

It is computed from the ECMWF EPs reforecast of daily precipitation averaged over each warning area only for areas containing at least 3 grid points, discarding smaller areas. NPS is the ratio of the the interquartile (IQR) of daily ensemble members average precipitation over each area and the median. This spread normalised measure is commonly used to asses the spread of precipitation in a ensemble systems.

2.5.5 Potential Predictability Index (PPI)

Following the method described by Lavers et al. (2014), potential predictability is computed as the coefficient of determination r^2 , or the square of the linear Pearson correlation coefficient, between the two series containing, for each forecasts steps (+ 24h to +168h, every 24h), the forecast fc and the "truth" t precipitation averaged each warning area WA_i . For example ensemble member 1 is considered "truth" while ensemble mean of members 2-11 is taken as a forecast. The process is repeated eleven times for all ensemble members. For each area and time steps we obtain 11 pairs of time series containing t and fc for all EPE cases of the last 20 years (about 30 cases for each forecast step). Final PPI is computed as average of r^2 of all ensemble members and over the areas, separating those being flat or being prominently mountainous. A third kind of average is done computing precipitation averages not on single warning areas but over the whole northern-central Italy domain (all).

2.6 Diagnosis of Rossby wave packet amplitude

The diagnosis of RWP amplitude (E) follows the approach of Zimin et al. (2003), with a few distinctions in the input variable and filtering steps. First, the 300hPa meridional wind anomaly at every latitude is zonally filtered to wavelengths 2,000–10,000km using a Tukey window in spectral space as in Fragkoulidis et al. (2018). Using the anomaly field excludes

the effect of stationary waves from the analysis and the zonal filtering restricts to the more relevant scales of a transient RWP evolution, that is, the typically small contribution from transient planetary waves and small-scale features is effectively discarded. Subsequently, a meridional convolution with a Hann window (Harris, 1978) of 7° length at half maximum is applied in order to account for possible nonphysical discontinuities from the latitude-wise application of the zonal filtering. Discarding the negative frequencies and applying an inverse Fourier transform to the meridional wind signal at every latitude results in a complex representation of this signal. The modulus of this so-called “analytic signal” corresponds to the envelope, E , of meridional wind, that is, the RWP amplitude. Finally, a weak smoothing is applied to the E field by discarding zonal wavelengths below 4,000km.

2.7 PV tendency framework

The spatio-temporal evolution of the upper-tropospheric flow preceding EPEs is investigated by analysing the potential vorticity (PV) tendencies, as introduced by Teubler and Riemer (2016). This framework was previously applied, among other studies, to investigate the amplification of a North Atlantic ridge–trough couplet, associated with a severe precipitation event on the northern side of the Alps (Piaget et al., 2015).

The framework is based on the hydrostatic form of PV on isentropic surfaces. Anomalies in PV, PV' , are calculated as deviations from a 30 day mean background state \overline{PV} . Following the concept of baroclinically coupled Rossby waves (Hoskins et al., 1985) the PV anomalies are separated into upper-level and low-level PV anomalies. The associated wind field perturbation is derived by piecewise PV inversion under nonlinear balance (Charney (1955); Davis (1992)). From that we calculate PV tendencies due to the advection of the PV background by (a) the upper-level wind field perturbation, which physically represents downstream development and by (b) the low-level wind field perturbation, which represents baroclinic interaction. We add the (negligible) advection term by the background flow to (a) and refer to this, in the following, as quasi-barotropic propagation. Additionally we derive the divergent flow by Helmholtz-partitioning. Similar to the advective tendencies from piecewise PV inversion we calculate the advection of the PV background by the divergent flow and additionally the PV tendency accounting for an area change of the anomalies due to divergent flow (compare tendencies from equation 6 in Teubler and Riemer (2020)). In the following, a vertical average of the PV tendencies between 315 and 350K (every 5 K) is considered to account for the seasonal cycle. A more detailed description of the PV tendency framework and a comparison to the more commonly used eddy kinetic energy framework can be found in Wirth et al. (2018).

Chapter 3

Scientific publications

The core of this dissertation is composed by three scientific publications which are included here in chronological order after a short description, the main goal and authors contribution.

1) Grazzini, F, Craig, GC, Keil, C, Antolini, G, Pavan, V. (2020a): *Extreme precipitation events over northern Italy. Part I: A systematic classification with machine-learning techniques.* *Q J R Meteorol Soc.* 2020; 146: 69– 85. <https://doi.org/10.1002/qj.3635>.

This publication explains the original method for classifying extreme precipitation events in three categories. The classified events are used as a basis for composites in all the successive steps of the research. *Author contribution:* FG and GC designed the research. FG designed and wrote the scripts (including machine-learning code). GA and VA handled the ARCIS archive and provided pre-processed data. CK provided a contribution on the interpretation and use of convective time scale concept. All authors discussed results and manuscript draft.

2) Grazzini, F., Fragkoulidis, G., Pavan, V. et al. (2020b): *The 1994 Piedmont flood: an archetype of extreme precipitation events in Northern Italy.* *Bull. of Atmos. Sci. and Technol.* 1, 283–295. <https://doi.org/10.1007/s42865-020-00018-1>

In this article we revisit an extreme event (which caused enormous losses in Northern Italy) in the context of our new classification methodology, showing that is falling in the most severe category. Through the analysis of this case we try to identify possible strategies for the use of real-time classification. *Author contribution:* FG outlined the research. FG and GF run scripts and produced Fig. 2-6, GA and VP took care of Fig.1 and handling of the observational database. FG and GF discussed the results and contributed mainly in the writing although all authors contributed to the manuscript draft.

3) Grazzini, F, Fragkoulidis, G, Teubler, F, Wirth, V, Craig, GC. (2021): *Extreme precipitation events over northern Italy. Part II: Dynamical precursors.* *Q J R Meteorol Soc.* ; 1– 21. <https://doi.org/10.1002/qj.3969>

Through composite analysis, we did a systematic investigation of the dynamical precursors and drivers of the EPE in the different categories. For the first time we apply an advanced PV tendencies framework on a large number of cases. We obtained detailed insights on the dynamical evolution prior different EPE categories. These information provide an interpretative framework for the predictability differences in presented in Chapter 4. *Author contribution:* FG outlined the research. GF and GC and VW contributed to the refinement of the study. FG and GF run scripts and produced figures, with the exception of Fig. 12-14, which were made by FT which also implement and handled the PV tendency diagnostic. FG , GF and FT discussed the results and contributed mainly in the writing although all authors contributed to the manuscript draft.

3.1 EPE systematic classification with machine-learning (Part I)

RESEARCH ARTICLE

Extreme precipitation events over northern Italy. Part I: A systematic classification with machine-learning techniques

Federico Grazzini^{1,2}  | George C. Craig¹ | Christian Keil¹  | Gabriele Antolini² | Valentina Pavan²

¹Meteorologisches Institut,
Ludwig-Maximilians-Universität, München,
Germany

²Operational Department, ARPAE-SIMC,
Regione Emilia-Romagna, Bologna, Italy

Correspondence

Federico Grazzini, Meteorologisches
Institut, Ludwig-Maximilians-Universität,
München, Germany.
Email: federico.grazzini@lmu.de

Funding information

Ludwig-Maximilians-Universität München

Abstract

Extreme precipitation events (EPEs) are meteorological phenomena of major concern for society. They can have different characteristics depending on the physical mechanisms responsible for their generation, which in turn depend on the large and mesoscale conditions. This work provides a systematic classification of EPEs over northern–central Italy, one of the regions in Europe with the highest frequency of these events. The EPE statistics have been deduced using the new high-resolution precipitation dataset ArCIS (Climatological Archive for Central–Northern Italy), that gathers together a very high number of daily, quality-controlled and homogenized observations from different networks of 11 Italian regions. Gridded precipitation is aggregated over Italian operational warning-area units (WA). EPEs are defined as events in which daily average precipitation in at least one of the 94 WAs exceeds the 99th percentile with respect to the climate reference 1979–2015. A list of 887 events is compiled, significantly enlarging the database compared to any previous study of EPEs. EPEs are separated into three different dynamical classes: Cat1, events mainly attributable to frontal/orographic uplift; Cat2, events due to frontal uplift with (equilibrium) deep convection embedded; Cat3, events mainly generated by non-equilibrium deep convection. A preliminary version of this classification is based on fixed thresholds of environmental parameters, but the final version is obtained using a more robust machine-learning unsupervised K-means clustering and random forest algorithm. All events are characterized by anomalously high integrated water vapour transport (IVT). This confirms IVT as an important large-scale predictor, especially for Cat2 events, which is shown to be the most important category in terms of impacts and EPE area extension. Large IVT values are caused by upper-level waves associated with remotely triggered Rossby wave packets, as shown for two example Cat2 events.

KEYWORDS

ArCIS, atmospheric rivers, extreme precipitation, large-scale precursors, machine learning, precipitation classification, Rossby wave packets, waves to weather

This is an open access article under the terms of the Creative Commons Attribution License, which permits use, distribution and reproduction in any medium, provided the original work is properly cited.

© 2019 The Authors. *Quarterly Journal of the Royal Meteorological Society* published by John Wiley & Sons Ltd on behalf of the Royal Meteorological Society.

1 | INTRODUCTION

Prediction of extreme precipitation events (EPEs) is a fundamental scientific challenge and of key importance to society, not only for civil protection purposes but also for water management optimization. EPEs result from interactions of different physical processes on a wide range of spatial and temporal scales and this complexity poses challenges for their skilful forecast. Large-scale slowly evolving flow can be predictable over many days, but convective situations, dominated by fast processes, can be characterized by upscale error growth that can severely reduce predictability (Hohenegger *et al.*, 2006). A deeper understanding of how the large-scale atmospheric flow interacts (especially in terms of error propagation) with local dynamical and precipitation processes is fundamental to make significant progress in extreme precipitation and flood forecasting. This interaction has been shown to change on a case-to-case basis (Craig and Selz, 2018).

Several atmospheric and geographical factors can contribute to the development of EPEs. A key element is moisture availability and its transport, a necessary condition to achieve extreme daily accumulations (Lavers and Villarini, 2015). Other factors include presence and organization of convection, thermal and moisture stratification, precipitation efficiency, air-stream ascent mechanism and interaction with orography, proximity to the sea and vertical wind shear. The Mediterranean area is located at the end of the Atlantic storm track and, with the combination of a warm sea (especially in autumn) surrounded by high orography, presents a perfect laboratory to study the relative contribution of the different factors (Khodayar *et al.*, 2018). A number of studies have already identified large-scale precursors of Mediterranean EPEs. Several authors highlighted the presence of an upper-level trough (Rossby wave) that enables, on its eastward movement, a warm-moist southerly airflow over the western Mediterranean basin (Massacand *et al.*, 1998; Grazzini, 2007; Martius *et al.*, 2008; Nuissier *et al.*, 2011; Pinto *et al.*, 2013). In addition, Pfahl *et al.* (2014) and Raveh-Rubin and Wernli (2015) have shown that more than 50% of these moist airflows are classifiable as a Warm Conveyor Belt (WCB), pointing to the importance of baroclinic instability and large-scale lifting for extreme precipitation in this region. The analysis of moisture supply for EPEs confirms a prominent role of large-scale transport with important contributions, especially in convective cases, from local sources. For example, Winschall (2013) and Winschall *et al.* (2014) have shown a high event-to-event variability in moisture supply. They identify water vapour coming from remote origins such as the North and subtropical Atlantic as a major contributor for stratiform precipitation, while a greater contribution comes from local moisture sources, like evaporation from the Mediterranean Sea, when Mesoscale Convective Systems (MCS) produce heavy precipitation. Within the WCB of extratropical

cyclones, strong moisture advection usually occurs in narrow filaments of high integrated water vapour, called atmospheric rivers. Studies have indicated that atmospheric rivers can be a precursor of heavy precipitation in mountainous areas, also in Europe as shown by Lavers and Villarini (2013).

Given this large body of previous studies highlighting both large-scale components and significant contributions of local convective processes leading to EPEs (Ducrocq *et al.*, 2014), it is desirable to condense this knowledge by developing a systematic classification of EPE. Inevitably, such a classification will introduce simplifications with respect to physical processes acting in nature, but it may prove useful to gain a deeper understanding. In an operational context, this may help forecasters to build conceptual models for different kinds of EPEs, while in research it will allow us to study predictability for each specific category separately. Some authors have already dealt with precipitation classification methods, first looking only at precipitation data (Llasat, 2001; Pinto *et al.*, 2013), or combining two-dimensional (2D) radar data and neural network classification algorithms to discriminate between frontal and convective precipitation (Walther and Bennartz, 2006). Molini *et al.* (2011) classified severe rainfall events based on hydro-meteorological and dynamical criteria over a period of 3 years.

Expanding the Molini *et al.* (2011) approach we propose a categorization method which considers dynamic upper-air variables and the thermodynamic state, in addition to precipitation data. Our goal is to discriminate between three categories of EPE: those of frontal origin, those generated by deep convection, and an intermediate category. In this respect, a machine-learning approach provides an innovative framework to achieve this classification. Among its advantages are easy-to-generalize methods, efficient handling of a large number of predictors, integration of physical understanding into statistical models and exploration of additional information from the data, as shown in a series of applications related to high-impact weather recognition by McGovern *et al.* (2017). K-means clustering has been widely used for clustering weather patterns (see e.g. a similar approach applied to precipitation over Greece by Houssos *et al.* (2008)). However, the combination of K-means, plus random forest refinement (see sections 2.1 and 4.2 for a brief description of the two algorithms) used here, is novel. The result of this combination is to produce a better separation of EPEs into three different categories, outperforming the subjective classification.

We restrict our analysis to northern–central Italy, an area very prone to these phenomena with numerous cases documented and described in the literature. Isotta *et al.* (2014) shows that this region is one of the areas in Europe with the highest fraction of high-intensity precipitation days compared to the total number of wet days. Our EPE database contains 887 events spanning a period of 37 years (1979–2015),

thus significantly increasing the number of cases compared to previous studies. For instance, this is a 10-fold increase compared to Molini *et al.* (2011).

After having described in detail the datasets used and the choice of the predictors in section 2, we present the EPEs classification focusing on the seasonal distribution of the events and commenting on its connection with seasonality of the large-scale forcing in section 3. In section 4 we show the clustering criteria. In section 5 we discuss the results, illustrate the characteristics of the different EPE categories, and focus in particular on events classified in category 2 for which we show two example cases. We conclude in section 6.

2 | DATA AND METHODS

This study is based upon three complementary data sources:

1. ECMWF ERA-Interim reanalyses for atmospheric fields (Dee *et al.*, 2011)
2. Northern–central Italy daily precipitation dataset ArCIS
3. Italian warning-area shape data (provided by Italian Department of Civil Protection) used to compute precipitation area averages

ArCIS (Archivio Climatologico per l'Italia centro-Settentrionale, Climatological Archive for Central–Northern Italy) is a gridded precipitation dataset (5 km × 5 km) derived from 1,762 rain-gauges that belong to different networks of 11 Italian regions plus a number of stations of adjacent Alpine nations. The area covered is north-central Italy, at daily temporal resolution for the period 1961–2015. Input data are checked for quality, time consistency, synchronicity and statistical homogeneity. Data are interpolated using a modified Shepard scheme. A full description of the dataset can be found in Pavan *et al.* (2019). The 24 h accumulation period follows the best practice of the Italian Hydrological Service reporting between 0800 and 0800 UTC. That means that the nominal time of precipitation records is shifted by plus one day with respect to most of the hours in which rain has potentially been accumulated. This is taken into account, subtracting one day when comparing with daily mean reanalysis data. Precipitation is aggregated over warning-area units (WA) provided by the Italian Department of Civil Protection, where they are used operationally for the national warning system. WAs are defined¹ by a suitable aggregation of subregional hydrological basins. The goal is to obtain homogeneous areas with respect to the type and intensity of meteo-hydrological phenomena within a given territory. North-central Italy is subdivided into 94

WAs (displayed in Figure 1) with the naming convention being an abbreviation of the administrative region followed by an alphanumeric code. Their area extension ranges from the smallest domain in Tuscany of 192 km² (Tosc-S3) to the largest domain in Trentino Alto-Adige Alpine region of 7,398 km² (Tren-A). The mean area extension is 1,750 km². First, we compute the daily spatially average precipitation and spatial standard deviation for each WA for the period 1979–2015. Secondly, we compute precipitation percentiles considering wet days only (daily accumulation greater than or equal to 1 mm). EPEs are subsequently defined as days with daily precipitation greater than or equal to the 99th percentile across one or more WAs. A description of each area, including their precipitation percentiles value, is provided in Table S1 in File S1. Note that with this upscaling approach we are implicitly disregarding localized events smaller than roughly 300 km².

Fields from European Centre for Medium-range Weather Forecasts (ECMWF) ERA-Interim reanalyses are retrieved at 6 h intervals, temporally accumulated to daily resolution and spatially averaged over a box covering north-central Italy (indicated by the blue rectangle in Figure 1 and hereafter called target domain). Upper-air fields are averaged over the target domain, rather than on single warning areas, since our final goal is to study how a given upper-level flow forcing produces different precipitation characteristics at the surface conditional on the dynamics and the thermodynamic stratification. ArCIS and ECMWF ERA-Interim datasets are used for the common period 1979–2015.

2.1 | Choice of atmospheric predictors

The choice of predictors was obtained through a combination of established variables described in the literature or previous case-studies with predictors typically used by forecasters in their operational experience. We select eight possible predictors which describe the EPE environment, including variables sensitive to flow conditions and variables representative of thermodynamic conditions. Their names and abbreviations are listed and fully described in Table 1. In particular, the use of CAPE, the convective adjustment time-scale Tau (see section 2.2) and IVT accounting for water vapour fluxes (Lavers and Villarini, 2015) are well documented. In addition, θ_{e850} and TCWV are used for describing air-mass types. $\Delta\theta_e$ and BS₅₀₀₋₉₂₅ (Bulk Shear) are also included, providing further information on the convective environment. For each day in the 37-year period, spatial averages across the target domain are computed for these variables. Initial tests showed that maximum/minimum values for fields describing the convective environment have better discriminatory power than their mean daily values. Thus, maximum values of spatial averages of Tau, CAPE, BS₅₀₀₋₉₂₅ and minimum values of $\Delta\theta_{e500-850}$, all available at 6-hourly temporal resolution, are used instead of daily means.

¹WAs definition can be found here (in Italian): http://www.protezionecivile.gov.it/attivita-rischi/schede-tecniche/dettaglio/-/asset_publisher/default/content/zone-di-aller-3.

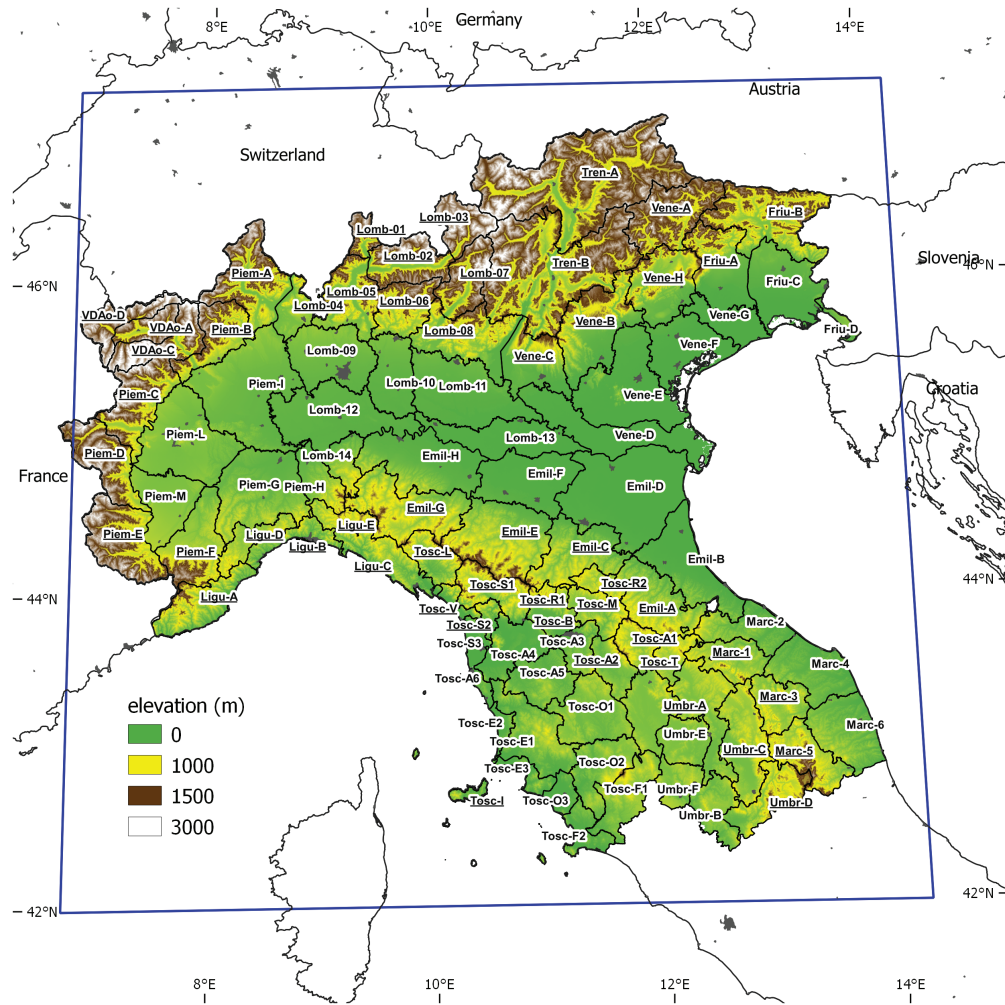


FIGURE 1 The figure shows the 94 warning areas of north-central Italy (as defined by Italian Civil Protection) used for precipitation averaging. Labels indicate the name of each warning area which is composed of an abbreviation of the administrative region followed by an alphanumeric code. Underlined names indicate areas characterized by significant orography (see the elevation legend). The blue rectangular box represents the target domain used for averaging atmospheric variables. Latitudes and longitudes for reference are included along the inner border of the figure

TABLE 1 ERA-Interim variables chosen as predictors to represent the large-scale flow associated with EPEs. For each EPE day, variables are spatially averaged over the Target Domain and aggregated daily as reported in the table

Variable	Description	Units
τ_{dmax}	Daily maximum of convective adjustment time-scale	h
$CAPE_{dmax}$	Daily maximum of CAPE	J/kg
IVTe	Daily mean of zonal component of integrated water vapour transport (surface up to 300 hPa)	$kg\ m^{-1}\ s^{-1}$
IVTn	Daily mean of meridional component of integrated water vapour transport (surface up to 300 hPa)	$kg\ m^{-1}\ s^{-1}$
θ_{e850}	Daily mean of equivalent potential temperature at 850 hPa	K
$\Delta\theta_{e500-850_dmin}$	Daily minimum of $\Delta\theta_e$ (500–850)hPa	K
TCWV	Daily mean of total column water vapour	kg/m^2
$BS_{500_925_dmax}$	Daily maximum of wind bulk shear 500–925 hPa	m/s

2.2 | Convective adjustment time-scale computation (τ)

The convective adjustment time-scale is used to discriminate between atmospheric states that differ by the rate of removal

of conditional instability: equilibrium and non-equilibrium regimes (Done *et al.*, 2006). In the equilibrium regime the generation of CAPE is balanced by widespread convective heating associated with synoptic forcing, while in the non-equilibrium regime CAPE can rise to larger values since

convection is limited by high convection inhibition (CIN) and its initiation is associated with local circulations in the boundary layer (weak large-scale forcing). Values between 3 and 12 h can be used as a threshold to discriminate between these regimes with a value of 6 h mostly used (Molini *et al.*, 2011; Keil *et al.*, 2014; Kober *et al.*, 2014). Following Zimmer *et al.* (2011), Tau is computed as

$$Tau = 1/2 * \left(\frac{Cp\rho_0T_0}{Lvg} \right) * \left(\frac{CAPE}{P} \right)$$

at 3 h intervals and averaged over the target domain. CAPE and precipitation P are extracted from short-term forecasts of ERA-Interim at 3 h intervals since these are not analysed fields. P is divided accordingly to obtain hourly precipitation rates needed for the computation. We omit grid-points with hourly rain rates lower than 0.2 mm/h. This empirically determined threshold allows a good balance between avoiding very low intensities that would produce spurious high values of Tau, and providing enough data points for a robust estimate. The domain-averaged Tau is set to zero if there are less than 10% precipitating grid points.

2.3 | Machine-learning algorithm description and Silhouette score

The machine-learning classification is performed using modules of the Scikit-Learn library written in Python (Pedregosa *et al.*, 2011). In particular, for clustering we use the *Kmeans* method of the *sklearn.cluster* module, and for removing the unnecessary predictors (or reducing impurity in the machine-learning language) we used the *RandomForestClassifier* method, and its attribute *feature_importances*, which are part of the *sklearn.ensemble* module. As an objective metric to judge the cluster separation into three categories we used the Silhouette score (Rousseeuw, 1987), implemented in the *silhouette score* method part of the *sklearn.metrics* module. This score measures, along each dimension (i.e. each predictor in a normalized space), how tightly the events are grouped inside each cluster (cohesion) compared to the remaining clusters (separation). It ranges from -1 (wrong clustering) to 1 (fully separated clusters) with values equal to 0 indicating that a given element has the same distance from the other cluster centroids (overlapping). The Silhouette score is computed for all classification methods and averaged over all elements falling in each category.

3 | EPE SEASONAL DISTRIBUTION

The seasonal distribution of all 887 EPE days is displayed in weekly bins in Figure 2. One bin contains 7 days, each counting from the first day of the year. Grouping in weeks instead of months, as done in previous studies, provides a more

detailed temporal evolution and facilitates deeper insights into the large-scale triggering of the events. All EPE days are attributable to 633 independent events (separated at least by one day) with a mean duration of $1.4 (\pm 0.7)$ days. A marked seasonal cycle is visible in Figure 2 with a main peak in the autumn season. From the beginning of September to the beginning of December the relative frequency of EPEs is very high, reaching a maximum in weeks 45 and 46, where values are larger than one. Relative frequencies greater than one implies more than one EPE day per week. This is caused by the higher frequency of events persisting over consecutive days in this period of the year (the mean duration in weeks 45 and 46 increases to 1.8 days). This autumn peak of heavy precipitation events over the Mediterranean is well documented (Khodayar *et al.*, 2018; Pavan *et al.*, 2019) and is explained by the large thermal gradient between the warm sea and the atmosphere, favouring strong moisture and heat exchange. Winter and mid-summer are periods with a low EPE frequency, while from April to mid-June a secondary peak emerges that is less discussed in the literature. The observed frequency in spring is almost half of that observed in autumn and the interannual variability is much higher, as indicated by the wider confidence interval. The entire seasonal cycle of EPEs shows remarkable correlation with mean IVTn fluxes (Figure 2). This has important implications since it indicates that EPEs are statistically associated with large-scale precursors which are ultimately responsible for triggering strong meridional water flux transport towards the target area. On EPE days, the mean IVTn anomaly over the target domain is in fact $+1.3$ standard deviations over its climatological (weekly) value.

4 | EPE CLUSTERING AND CLASSIFICATION

In the previous section we have shown that periods with high EPE frequency are associated with anomalously high IVTn. However, the resulting precipitation pattern can vary substantially depending on details of the mesoscale and thermodynamic state. Given a similar large-scale setting, an EPE can be generated by different processes, including or excluding convection for example. In winter for example, when colder air masses hold less water vapour, EPEs can be achieved only by a strong moisture transport from remote areas (e.g. in the form of atmospheric rivers) in association with additional uplift forced by steep topography. Lavers and Villarini (2013) have shown in fact that this association is stronger in winter months. On the other end, in summer, characterized by high moisture availability and high thermodynamic instability, a weaker thermal circulation can be sufficient to trigger convection, even on modest relief (Khodayar *et al.*, 2018). The details of the different precipitation mechanisms of moist flow impinging on orography

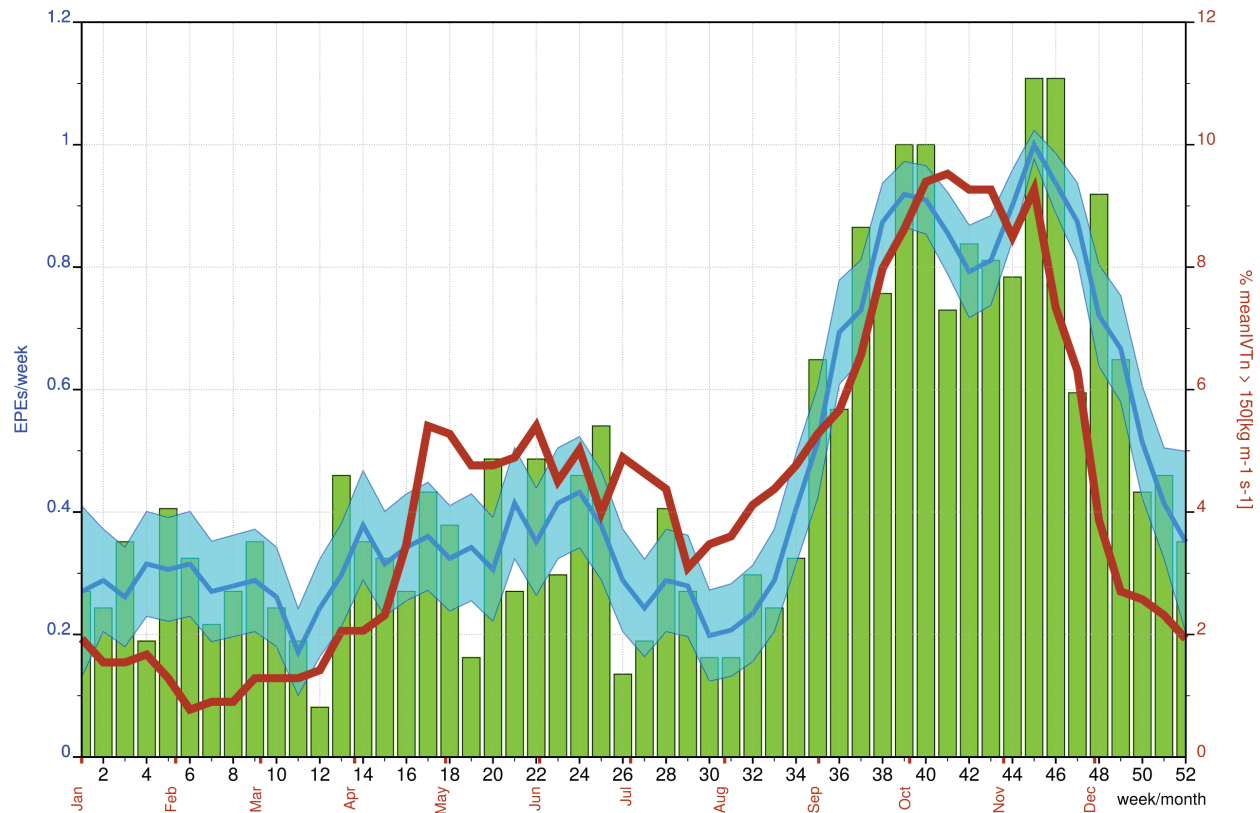


FIGURE 2 Seasonal distribution of EPEs in the period 1979–2015. Bars show the mean frequency of EPEs in bins of 7 days. The thin solid blue curve and corresponding shaded area depict moving averages over 21 days and 95% confidence intervals, respectively, estimated with the adjusted Wald method assuming a binomial distribution inside each bin. The thick red curve shows the climatological frequency of days with IVTn averaged over the target domain greater than 150 ($\text{kg m}^{-1} \text{s}^{-1}$), a threshold corresponding to the 95th percentile of the area-averaged IVTn distribution for all days in the period 1979–2015. The IVTn curve is also based on a 21-day moving average

have been extensively investigated in the Hydrological cycle in Mediterranean eXperiment (HyMeX) project, and in particular during the special observing period SOP1 dedicated to studying heavy precipitation across the Mediterranean (Ducrocq *et al.*, 2014). Davolio *et al.* (2016) have shown, for example, two case-studies with similar large-scale flows that result in two very different precipitation patterns. The difference was attributable to the type of interaction of the impinging flow with orography; in one case producing convection upstream due to persistent blocked-flow conditions, while in the other case heavy rain was limited to the main Alpine crest as the flow went over the orography. This characterization is based on a detailed analysis of how the flow interacts in space and time with the orographic barrier, and would be difficult to repeat for our large EPE dataset. For this reason, we propose a more practical approach based on a categorization of EPEs according to mean values of typical predictors averaged over the target domain. Based on these arguments, we subdivide EPEs into three categories differentiated by the main processes involved:

- Category 1 (main process: *frontal/orographic uplift*)
EPEs in this category originate from intense and persistent frontal structures, including slantwise ascent in warm

sectors, often classifiable as Warm Conveyor Belt (WCB), initiated by an upper-level Rossby wave in the western Mediterranean. Mechanical orographic uplift of low-level marine, moist air is the key factor to attain extreme precipitation over steep topography. Remotely transported moisture via atmospheric rivers may also play a role. Rare presence of convection, mostly associated with cold-front passages, accounts only for a small fraction of total precipitation of the event.

- Category 2 (main process: *frontal uplift with equilibrium deep convection embedded*)

This category shares with the first a prominent large-scale signature, with an amplified upper-level precursor (Rossby wave) in the western Mediterranean but a stronger southerly flow component. However, reduced moist static stability might lead to the occurrence of deep convection, often in the form of back-building MCS (Lee *et al.*, 2016) embedded in WCB ascent or more generally in the warm sector of the frontal system associated with Rossby waves. Persistent convergence lines over sea or close to orography, as in the case of presence of barrier-flow close to the orography, are the main factors triggering convection.

- Category 3 (main process: *non-equilibrium convection*)

Even in this category a synoptic-scale wave can often be recognized, but of smaller amplitude. EPEs are generated mostly by convective events in a high conditionally unstable thermodynamic environment (very high CAPE). Triggering is controlled by local factors in a complicated interplay with orography: thermal boundaries induced by direct circulations (including sea and mountain breezes), soil wetness gradients, or outflow of previous mature systems. Triggering is typically limited by persistent capping inversions. Precipitating structures tend to assume the form of single cells or MCS of different kinds depending on the steering wind, local thermodynamic characteristics and environmental wind shear.

4.1 | Subjective threshold-based classification

We investigate several ways to populate these three predefined categories. As a first approach we make a selection, based on experience and previous literature, using the list of predictors to obtain a reduced set for which we establish characteristic thresholds. We call this method the subjective threshold approach (STA). The convective time-scale τ represents our first choice due to its ability to discriminate between equilibrium and non-equilibrium convective cases, as described in section 2.2. For Mediterranean cases spanning a 3-year period, Molini *et al.* (2011) apply a threshold of 6 h for τ to classify heavy precipitation events over Italy and propose two categories: $\tau < 6$ h type I events (equilibrium convection events, larger than 2,500 km²), and $\tau > 6$ h type II events (non-equilibrium, smaller than 2,500 km²). However, this predictor alone is not able to discriminate between frontal precipitation with no convection embedded and cases of frontal precipitation with embedded convection. Both cases are characterized by very small values of τ . Kober *et al.* (2014) introduced CAPE as an additional predictor to account for stratiform cases over Germany. Similarly, we introduce CAPE to discriminate between events falling in category 1 (from now on indicated as Cat1), while for events above a certain CAPE threshold τ is used to distinguish between category 2 (Cat2) and category 3 (Cat3).

Figure 3 shows a scatter plot of τ_{dmax} against day of the year with colour coding according to the value of $\text{CAPE}_{\text{dmax}}$. In addition, a smaller panel displays the mean orographic fraction for 6 bins of τ_{dmax} . The orographic fraction is the ratio between the number of mountainous WAs (underlined WAs in Figure 1) and flat WAs affected by the EPE. Winter events (up to beginning of March) are characterized by low values of τ_{dmax} and high orographic fraction, meaning that winter events mostly occur in regions with high orography. Values of $\text{CAPE}_{\text{dmax}}$ are small, although not exactly zero since there is always some residual CAPE over sea, even in winter.

A selection of 15 benchmark cases (5 for each category) is used to determine a characteristic threshold value of $\text{CAPE}_{\text{dmax}}$. Since the event type is *a priori* known for these events (see Table S2 in File S1) we can assign $\text{CAPE}_{\text{dmax}}$ to specific weather regimes. The EPE benchmark cases that represent orographic precipitation events (Cat1) suggest a threshold value of 150 J/kg for $\text{CAPE}_{\text{dmax}}$. Together with the discrimination between Cat2 and Cat3 based on τ_{dmax} we obtain the following STA classification:

$$\text{Cat1 } \text{CAPE}_{\text{dmax}} < 150 \text{ J/kg,}$$

$$\text{Cat2 } \text{CAPE}_{\text{dmax}} \geq 150 \text{ J/kg and } \tau_{\text{dmax}} < 6 \text{ h,}$$

$$\text{Cat3 } \text{CAPE}_{\text{dmax}} \geq 150 \text{ J/kg and } \tau_{\text{dmax}} \geq 6 \text{ h.}$$

4.2 | Objective K-means classification

Although the classification proposed above provides a sufficient separation between the three categories, it is inherently subjective and requires *a priori* knowledge for a proper definition of the thresholds. In addition, only a small part of the information available in the complete list of predictors is used. We therefore apply an objective clustering method to exploit the full potential of the entire set of eight available predictors (see Table 1). We use a *K-means* method, one of the simplest and most-used unsupervised learning tools for unlabelled data. The algorithm assigns every data point to one of the K predefined groups (3 in our case) following a minimization of the inertia function or, in other words, the sum of squared distances within any cluster, between cluster centroid and points. Through a series of iterations, the algorithm creates groups of data points that have similar variance and that minimize the distances within the groups, in a multidimensional space defined by the number of predictors. Before applying any machine-learning algorithm (see section 2.3 for a description of the software modules used), all features (predictors) are normalized to the same scale (subtracting the mean and dividing by the standard deviation) to avoid distortion of the norm. Initially, we start clustering with all eight variables, being aware that some information is redundant due to cross-correlations between variables. The *K-means* method is applied in the default configuration. To check whether it is possible to reduce the number of predictors, we use a random forest method (*RandomForestClassifier*) to simulate the classification obtained by *K-means*. This ensemble learning method fits a number of decision trees (in our case 100 estimators or trees) to various subsamples of the dataset and uses averaging to improve the accuracy of the classification and control over-fitting (Breiman, 2001). In this way, we estimate the sensitivity of K-mean classification with respect to each predictor through the *feature_importances* attribute of the *RandomForestClassifier* method. In Figure 4, the ranking

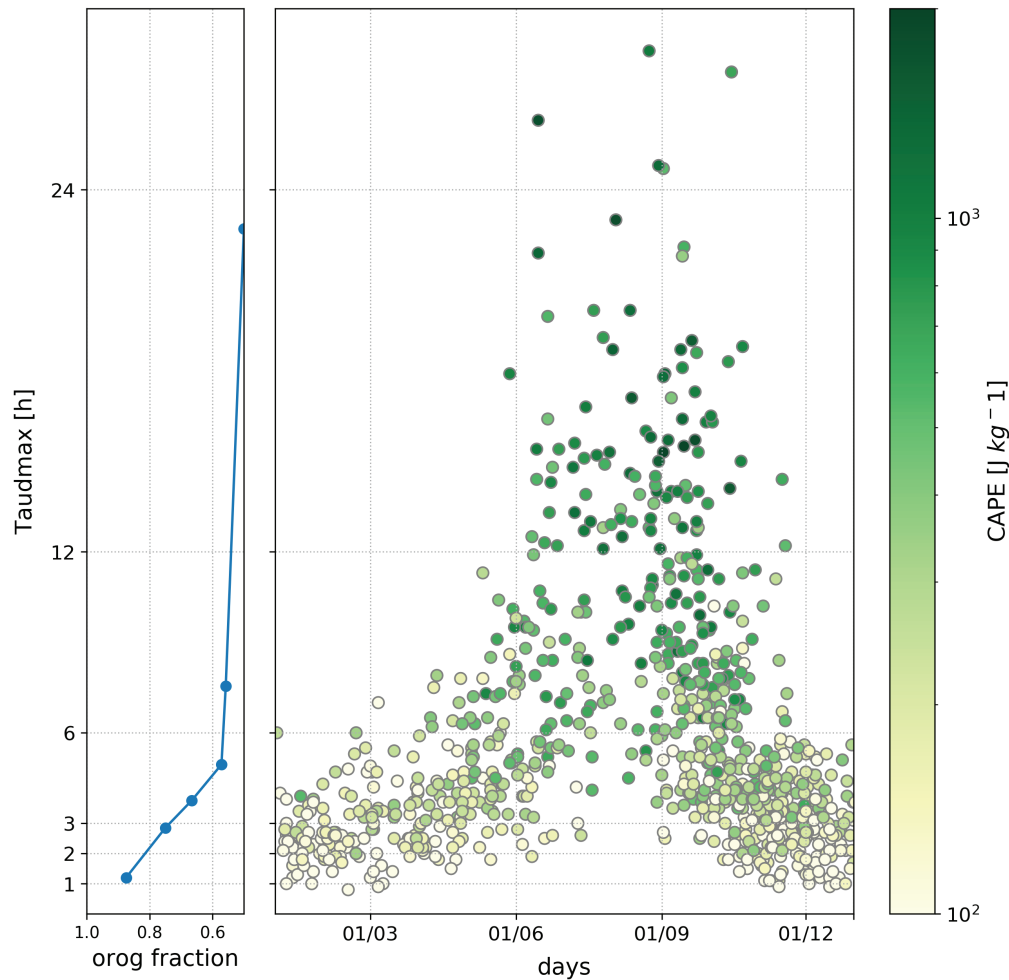


FIGURE 3 Distribution of EPEs in terms of Tau_{dmax} (on the y-axes), day of the year (x-axis on the larger plot), $\text{CAPE}_{\text{dmax}}$ (coloured) and orographic fraction (small plot on the left). The median orographic fraction has been computed using six equally populated bins. Dots on the left graph mark the centroid of the bins

of the eight predictors is displayed according to their importance in assigning a given EPE to one of the three categories. θ_{e850} and TCWV show the greatest importance, probably acting as air mass tracers, followed by Tau_{dmax} , $\text{CAPE}_{\text{dmax}}$ and $\Delta\theta_e$, all important for describing the potential and type of the convective environment. The surprisingly low ranking of IVTn can be explained by the fact that the IVTn component plays an important role in all three categories so its ability to discriminate is low, however not negligible. Finally, IVTe and $\text{BS}_{500,925_{\text{dmax}}}$ are well below 0.05. Therefore, we considered the latter two descriptors not important and consequently dropped. The final configuration of K-means clustering is based on the six remaining predictors.

4.3 | Comparison between K-means and subjective method

Different approaches are employed to comparatively evaluate both methods. First, we focus on key properties such as a visual separation of the clusters in pairs of two selected dimensions. In Figure 5 a scatter plot comparing Tau_{dmax} and

TCWV is presented. While the STA approach guarantees a sharp separation in terms of the selected variables (Tau_{dmax} and $\text{CAPE}_{\text{dmax}}$), it does not guarantee a sufficient separation in the remaining variables, as can be seen along the TCWV axis with Cat1 and Cat2 almost completely overlapping and with less separated centroids compared with K-means classification. An interesting property emerging from K-means clustering is that the value of Tau_{dmax} that separates Cat2 from Cat3 decreases as the value of TCWV increases, indicating that a transition towards non-equilibrium convection is becoming more likely even with low Tau values as total water vapour increases in the column. This can be seen in the right panel of Figure 5 where the separation between orange dots (Cat2) and green dots (Cat3) follows a diagonal line. To the authors' knowledge, this dependence has not been highlighted in previous literature. Another important metric is the seasonal distribution of the three different categories. According to its definition, we expect that Cat1 events are more frequent during the cold season, while Cat3 should peak in summer months. Cat2, being an intermediate category, is expected to be most frequent during transition seasons.

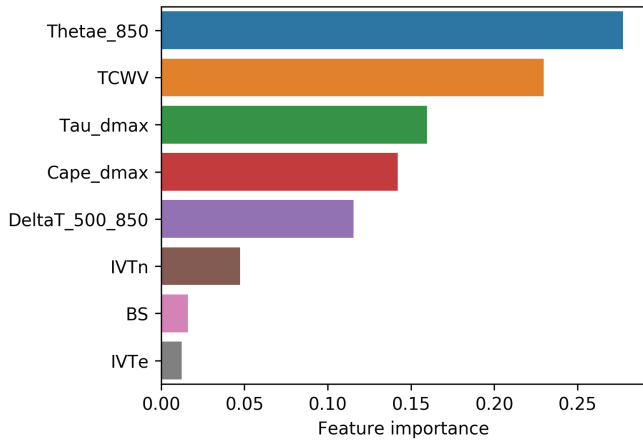


FIGURE 4 Feature importance ranking computed with the homonymous attribute of the *RandomForestClassifier* algorithm. The algorithm was run using the output of the K-means prediction with all eight predictors as target data (see text for further explanation). The last two predictors, IVTe and BS_500_925_dmax (abbreviated in the label figure to BS) are dropped since they rank well below 0.05

Indeed, comparison of the two methods shows a clear advantage of the K-means clustering method in producing more separated categories over the seasons (Figure 6). K-means produces, as expected, a prominence of Cat1 events in winter. On the contrary, the STA approach gives a more mixed situation in winter, with a frequent overlapping between Cat1 and

Cat2, indicated by the brown colour. Moreover, Cat2 is more prominent in transition seasons using the K-means clustering.

A third classification method simply based on the week of the year (seasonal classification) is used as an additional independent dataset to be compared against the other two. As can be seen in Table 2, the Silhouette score (an objective measure of cluster separation) is highest for K-means clustering indicating a better separation than the other methods (STA and seasonal). Thus, the classification based on the K-means method is used in the remainder of the study.

5 | CLASSIFICATION RESULTS

A discussion of the characteristics of the three categories resulting from the K-means classification is now presented. The characteristics of each category are highlighted, starting with Cat1 events, followed by Cat3 and finally Cat2 events. The order reflects the fact that Cat1 and Cat3 events represent opposing extrema of the categorization, while Cat2 shows intermediate characteristics. Cat2 includes many of the most important EPE cases. The discussion is mainly based on three figures: Figure 7 displays the size distributions of the EPEs and the mean area of EPEs in each category (in the inset). Figure 8 shows a summary panel of nine key variables that can be thematically grouped: (a,b,c) present EPEs area

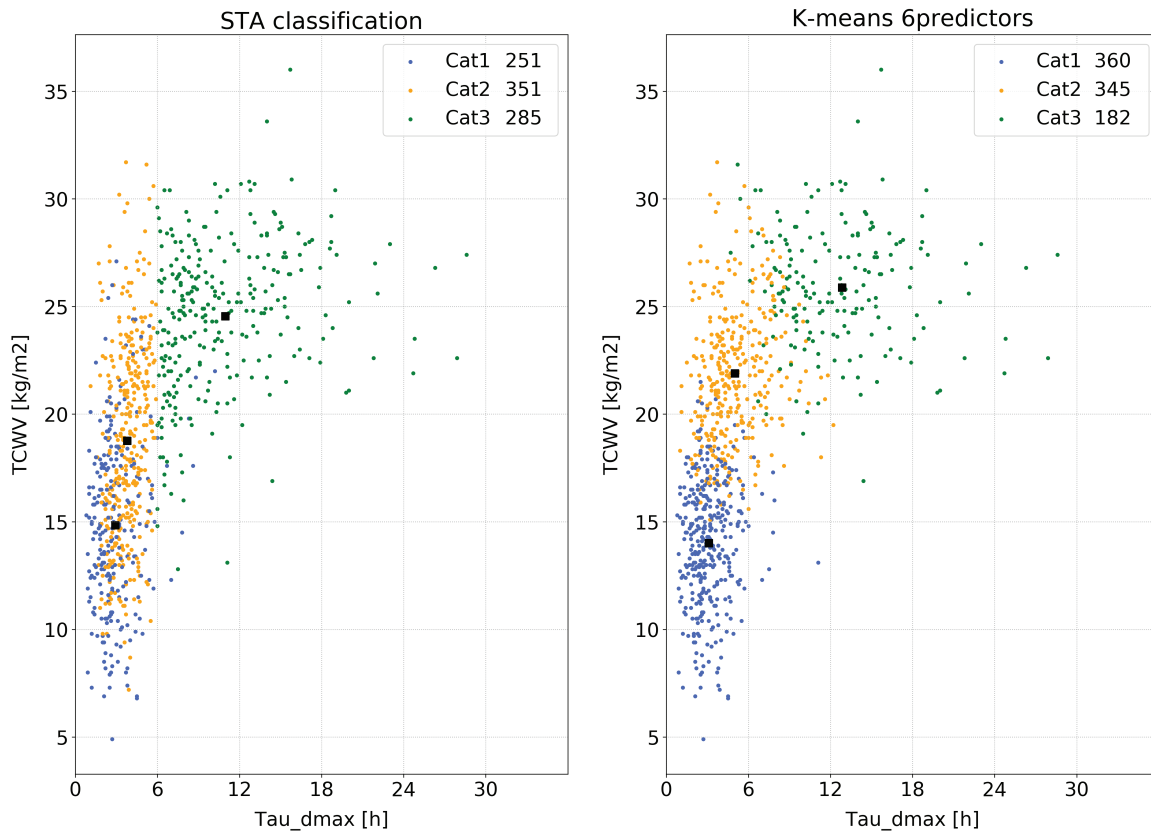


FIGURE 5 TCWV and Tau_{dmax} scatter plots for the two different types of classification. Subjective classification (left) and K-means based clustering (right) with six predictors. Black squares represent the centroids of the three different clusters. The respective population of each category is reported in the legend

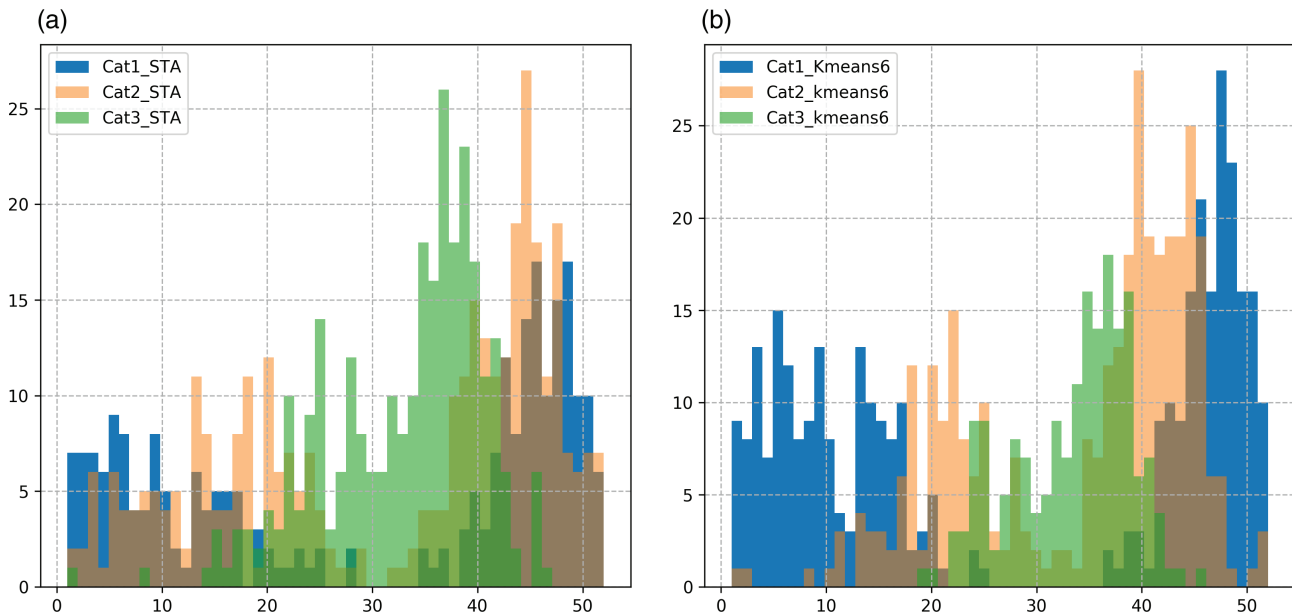


FIGURE 6 Distribution of EPE counts (y-axis) in the three different categories according to the week of the year (x-axis), obtained with K-means clustering with six predictors (Kmeans6, panel b), and subjective method (STA, panel a). In addition to the colours in the legend, overlapping colours are: brown (Cat1 + Cat2), olive green (Cat2 + Cat3)

TABLE 2 Silhouette score computed on the 6-dimensional predictor space used for K-means clustering. For comparison, the subjective classification (STA) and an alternative classification based on the week of the year are also scored. The score provides a measure of the efficiency of the algorithm in producing well-separated clusters. It ranges from -1 (wrong clusters) to 1 (fully separated clusters) with 0 meaning overlapping clusters. K-means with six predictors proved to be superior to other tested configurations

Score	K-means (6 predictors)	STA classification	Classification by week
Silhouette	0.31	0.13	0.12

characteristics, (d,e,f) thermodynamic instability indices, and (g,h,i) total column water vapour TCWV and vertical integrated transport IVT. Figures 9 and 10 depict respectively composite maps of geopotential height at 500 hPa (Z_{500}), mean sea level pressure (MSLP), θ_{e850} , and daily precipitation averaged over 100 events with the highest Silhouette score for each category.

5.1 | Category 1

On average, EPEs in Cat1 have the smallest area extension with a mean value close to $5,000 \text{ km}^2$ corresponding to 3.5 WAs involved (Figure 7 and Figure 8a). They are more frequent close to orography (orographic fraction 0.6, Figure 8c) and they have the smallest spatial variability inside the WA (Figure 8b). They are predominant in winter up to mid-May, when their frequency decays, and they start to appear again from December (Figure 6). They are characterized by strong moist static stability (Figure 8d,e,f) and show a comparable transport of water vapour from the zonal and the meridional

component (Figure 8h,i). The mean flow pattern (Figure 9, upper panel) shows a broad upper-level wave in Z_{500} centred over central Europe. A surface cyclone is present over the Tyrrhenian Sea, embedded in a weak θ_{e850} gradient, aligned with the main trough axis. Peak values of precipitation are lower and more confined than Cat2 and Cat3. The highest values are found along the Apennine crest, and to a lesser extent also over the Adriatic area in response to low-level easterly (bora) winds (Figure 10, left panel). This is highlighting the fact that Cat1 EPEs are associated with stable low-level flow, blocked by the upstream orography, and circulating around the surface cyclone. This flow configuration is a distinctive feature of cyclogenesis in the lee of the Alps (or Genoa Low), mainly occurring in winter/spring (Trigo *et al.*, 2002). This is confirming the expectation that Cat1 are mainly attributable to winter-type events, where in addition to the direct uplift on the windward side of the orographic barriers, baroclinic instability is locally increased by differential flow deformation at different levels (Buzzi and Tibaldi, 1978).

5.2 | Category 3

Events in Cat3 are comparable in size with Cat1 events, especially in terms of area extension. The size distributions in both peak strongly at $1,700 \text{ km}^2$ (Figure 7). Cat3 events occur from mid-May to the end of October with the highest frequency from mid-August to mid-September (Figure 6). This seasonal distribution is similar to the climatology of MCS over Europe (Morel and Senesi, 2002). Cat3 events show the lowest orographic fraction, where a value of 0.5 in orographic fraction indicates that EPEs in Cat3 occur with same frequency whether orography is present or absent in the WA,

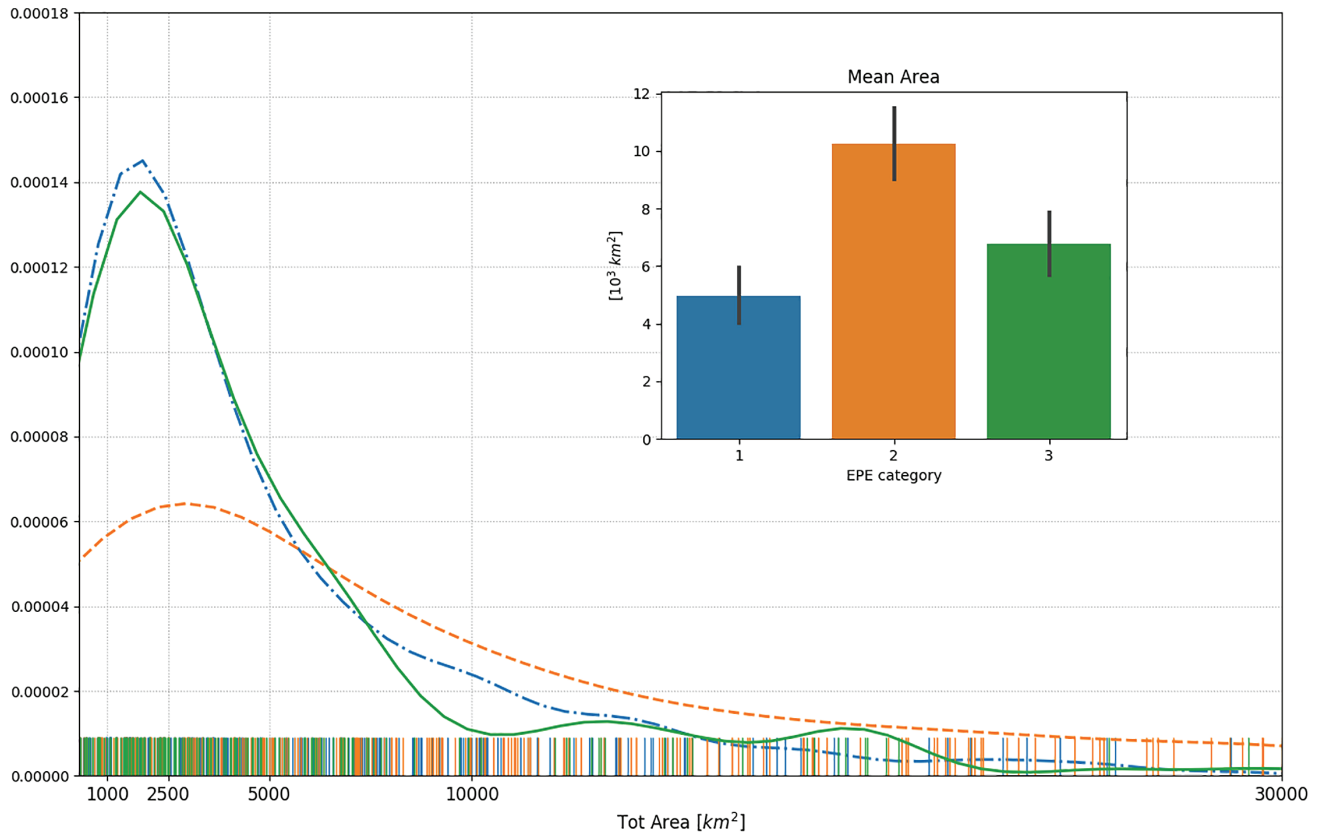


FIGURE 7 Density distribution of EPE area extension for the three different categories: Cat1 (blue dash-dotted line), Cat2 (orange dashed line) and Cat3 (green solid line). The inset shows the corresponding mean area and the 95% confidence interval

especially over central Italy (Figures 8c and 10 right panel). They also show the largest spatial standard deviation variability inside the WA (Figure 8b) indicating greater variability in the precipitation field typical for spotty convective events. Thermodynamic indices are significantly higher than for other categories as indicated by the highest values of $CAPE_{dmax}$, Tau_{dmax} , and conditional instability (negative value of $\Delta\theta_e$), respectively in Figure 8d,e,f. Finally, Cat3 shows the highest TCWV, reflecting warmer and moister air masses present in summer. Interestingly the highest moisture transport towards the target domain is attributable to the IVT zonal component (Figure 8g,h,i). The flow composite still shows an upper-level wave, but of smaller amplitude with a shallow and broad surface cyclone over the central Mediterranean, implying a weaker surface circulation. θ_{e850} values are also the highest (Figure 9). The precipitation composite shows a reduced locking of the precipitation along the orography of central Italy while a maximum emerges over the western–central Alps linked with summer convection which tend to be localized more on the Alpine range (Figure 10, right panel).

Based on the characteristics discussed above, we attribute Cat3 events to a predominance of non-equilibrium convection, clearly highlighted by mean values of Tau_{dmax} larger than 12 h. Non-equilibrium convective environment is characterized by weak large-scale forcing with the most relevant phenomena being thermally forced convection, that is notoriously

difficult to predict, as it responds to details in the spatial distribution of CAPE and convective inhibition (CIN) (Done *et al.*, 2006). Strong CIN constitutes a limiting factor that prevents the development of diffuse widespread convective activity but allows outbreaks of violent convection leading to extreme precipitation over limited areas. We hypothesize that the main features responsible for EPEs in this category are MCS affecting one or more WAs during their lifetime.

5.3 | Category 2

Cat2 events exhibit by far the largest spatial scale, both in terms of number of WA and affected area. The mean area for Cat2 is about 10^4 km², peaking (Substitute median with mode) at 3,000 km² (Figure 7). The different peaks in EPE area size of Cat1, Cat3 and Cat2 are consistent with Molini *et al.* (2011) who found a separation in scale between equilibrium (here Cat2) and non-equilibrium convection (here Cat3) at 2,500 km². Events in Cat2 are even more likely to affect WAs with orography. Interestingly, the seasonal distribution of the events in this category shows two peaks: one in spring around week 20 (mid-May), and a larger one in autumn, between weeks 40 and 45 (October–mid-November) (Figure 6). EPEs in this category are less thermodynamically stable than in Cat1, exhibiting a nearly neutral stratification with $\Delta\theta_{e500-850}$ close to zero (Figure 8f). The Cat2 upper-level

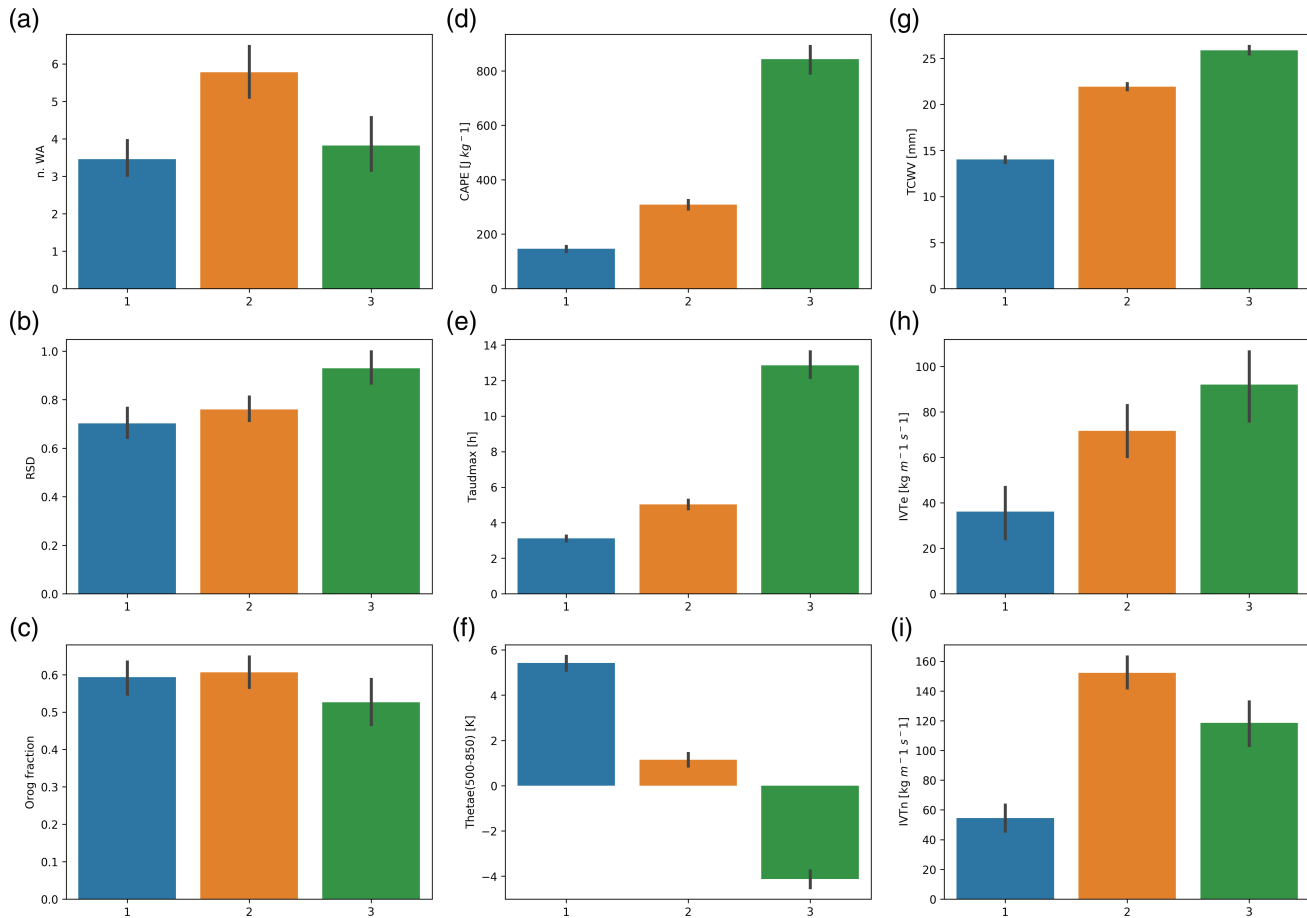


FIGURE 8 Nine key mean characteristics of the EPEs for the three categories. The first column shows statistics derived from observations aggregated over warning areas, respectively: (a) the mean number (n) of WA per event, (b) the relative spatial standard deviation (RSD, areal standard deviation of precipitation divided by the precipitation mean for each WA), (c) the orographic fraction (1 if all areas with EPE have orography; 0 EPE only on flat warning areas). Second column: (d) CAPE_{dmax} , (e) Taud_{dmax} , (f) $\Delta\theta_{e500-850-dmin}$. Third column: (g) TCWV, (h) IVTe/zonal component of IVT, (i) IVTn/meridional component. Confidence intervals are computed with a bootstrapping method as part of the Seaborn Python library

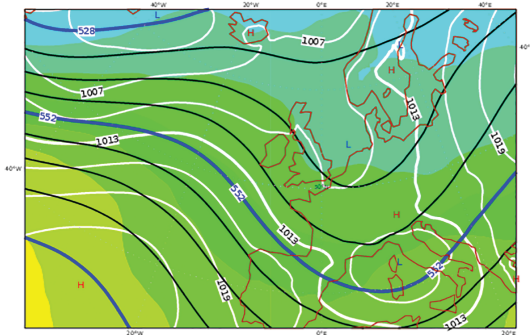
flow is characterized by the presence of a sharper trough compared with Cat1 (Figure 9). In addition, the trough axis is centred 5° in longitude more to the west, close to the Greenwich meridian, and has the main axis meridionally aligned, while in Cat1 it is more cyclonically tilted. The surface circulation and thermal gradients are stronger, with a deeper surface cyclone positioned over the western Mediterranean, in a forward position with respect to the upper-level main trough axis. All these characteristics indicate a more active baroclinic structure compared to both other categories, producing stronger meridional flow. Such a favourable positioning produces the highest moisture fluxes in the meridional direction (IVTn, Figure 8i).

Many favourable ingredients for generating strong EPEs are present for Cat2. In particular, there is a clear synergy between strong large-scale forcing, denoted by high values of IVTn, which in turn imply large-scale upward vertical motion induced by horizontal advection of moist/warm air masses, and boundary-layer conditions still supporting deep convection. Synoptically driven low-level jets over the warm waters of the Mediterranean Sea further destabilize (in potential

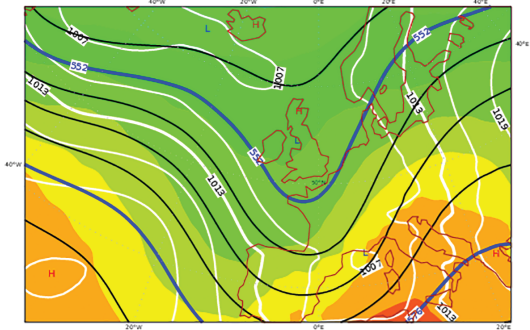
terms) the onshore flow, increasing low-level θ_e . This creates the ideal ingredient for the development of deep convection bursts embedded in the synoptic flow, typically localized at the interface between sea and coast or on the windward side of the orography close to the sea (Buzzi *et al.*, 1998; Kirshbaum *et al.*, 2018). The particular combination of stratiform precipitation and embedded deep convection explains why this category of EPE exhibits the highest precipitation intensity and the largest spatial extent as clearly evident in Figure 10, central panel.

To this category belongs the largest EPE in the period 1979–2015 which occurred on 1 November 2010, with an area extension of $70,000 \text{ km}^2$. If we extend the statistics of EPEs back to 1961 (the first available year of the ArCIS dataset), the November 2010 EPE is surpassed only by what is known as the “century” flood in Italy. This event, which occurred between 3 and 5 November 1966, badly impacted Florence, where 101 people died and millions of rare books and art masterpieces were inundated. Beyond Florence, 54 WAs (out of 94) were affected with a total area extension that reached $98,760 \text{ km}^2$ on 4 November, by far the largest size

(a) Cat1 - Sil: 0.52



(b) Cat2- Sil: 0.44



(c) Cat3- Sil: 0.37

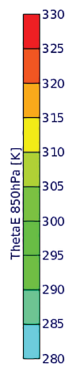
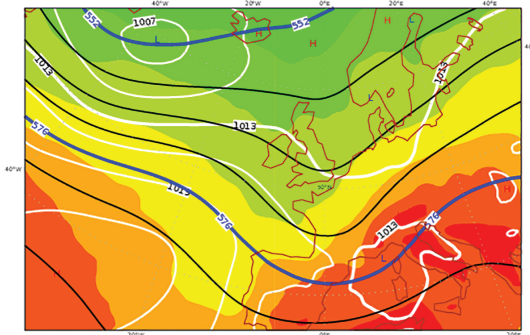


FIGURE 9 (a–c) Composite maps of the 100 events attaining the highest Silhouette score for each category. The average value of the Silhouette score for the three subsamples is reported at the top of each map. The fields shown are geopotential height at 500 hPa (contours every 6 dam in thick dark blue), MSLP (contours every 3 hPa in white) and θ_{e850} shaded according to the legend

in our dataset. Although not included in our list, since the ERA-Interim data are not available for this date, the K-means algorithm correctly classifies this EPE as Cat2 date (based on ECMWF ERA40 reanalysis data). A detailed meteorological description of that episode including a modelling study indicate that indeed the record precipitation was achieved by slowly moving stratiform rain preceding the cold front combined with an extensive line of deep convection, particularly active over the Apennines (Malguzzi *et al.*, 2006). Finally, it is also worth mentioning a recent event occurring on 27–30 October 2018, called storm “*Vaia*,” which affected north and central Italy with an amplitude similar to both cases above. Using ECMWF operational analysis as input, the objective classification classifies this EPE also in Cat2. A preliminary

analysis shows that this EPE is likely to become one of the strongest on record in terms of rain accumulation and integrated water vapour transport over the target domain. Further analyses are planned to study this event in detail.

The seasonal distribution of Cat2 shows a consistent correlation with the climatological monthly precipitation distribution, in particular concerning the monthly distribution of extreme daily rainfall on the southern side of the Alps (Isotta *et al.*, 2014). Consequently, the Cat2 distribution also fits well with the seasonality of the discharge of major rivers, like the Po river, showing two peaks, one in mid-May (due to melting snow plus peaks of rain) and the second in mid-November (due to wide and extreme rainfall only: Montanari, 2012).

We hypothesize that Cat2 events are closely linked with pulses of particularly long-lived Rossby Wave Packets (RWP), coherently maintained by a strong wave guiding effect. This long chain of downstream cyclone development is likely to open ideal pathways for long-range moisture transport towards the target domain (as documented by Piaget *et al.* (2014)). In the next section we show an example of this. This hypothesis has some important implication for predictability. Grazzini and Vitart (2015) have shown that if long and coherent RWPs (lasting more than 8 days) are present in the initial conditions, the resulting forecast shows higher skill than average conditions over Europe. An analysis of such an event is documented in the next section.

5.4 | Genesis of Cat2 events: An example

In this section, we show an example of a typical large-scale evolution leading to Cat2 EPEs. We focus on a period embracing two Cat2 events, both included in the list of benchmark cases reported in Table S2 in File S1. Both occurred within a 10-day period in autumn 2011: on 25 October 2011 (Cinque Terre flood, Figure 11b) and 4 November 2011 (Genova (Genoa) flood, Figure 11c). In both cases, localized convection stayed quasi-stationary within slow moving large-scale patterns, and precipitation accumulated in an area already affected by widespread heavy rain causing devastating floods at different spatial scales.

The main panel of Figure 11 illustrates the RWP propagation (and IVT transport) that ultimately led to the positioning of the upper-level waves associated with those EPEs. In the Hovmüller diagram we can see that the flow was characterized by an almost stationary wave pattern until 15 October, with main waves located over eastern USA and the Atlantic. A small-scale EPE event (less than 1,000 km²) occurred on the 19th associated with weak wave activity. On the 15th a large-amplitude RWP started off the west Pacific coast, reaching Europe on the 23rd. A second RWP pulse, apparently less coherent and split into two branches, started in the west Pacific on 26th and reached Europe on 3 November. In both cases RWP propagation ended when reaching Europe, leading

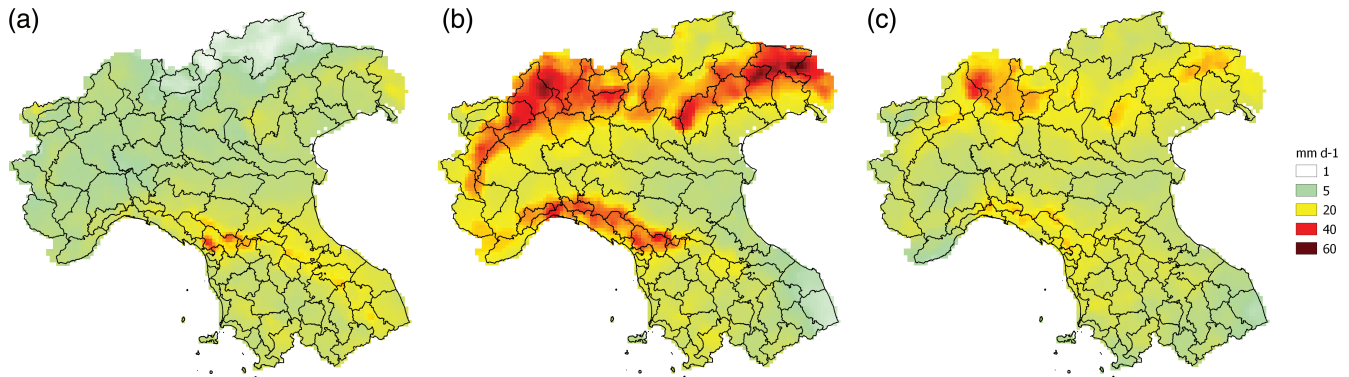


FIGURE 10 As in Figure 9 but displaying the EPEs precipitation composites for each category, overlaid on WA. (a) Cat1, (b) Cat2, (c) Cat3. Units are mm/day. EPEs in Cat2 are clearly the strongest

to a deep trough positioned slightly west of 0° longitude. These upper-level waves channelled very warm moist air from the Atlantic towards the central Mediterranean and the target domain. IVT values higher than $250 \text{ kg m}^{-1} \text{ s}^{-1}$, the threshold defining an atmospheric river (AMS meteorology glossary) are evident in both cases. The second RWP produced an even greater and more persistent water vapour transport from the central Atlantic, setting up favourable conditions not only for the EPE on 4 November, but also for three subsequent days (sequence of triangles in Figure 11). This extremely high IVT appears to be related to the convergence of anomalously high water-vapour amounts associated with the remnants of Atlantic tropical storm *Rina* (23–28 October), as discussed by Rebora *et al.* (2013).

6 | CONCLUSIONS

In this article, we describe a methodology for identification and systematic classification of extreme precipitation events (EPEs) over northern–central Italy. EPEs are defined as days when at least in one of the Italian Civil Protection warning-area units the spatially average daily precipitation is greater than the 99th percentile of the daily climatological distribution (1979–2015). The computation is based on the ArCIS gridded database, which is built from more than 1,700 quality-controlled stations. This database, in combination with ERA-Interim reanalysis data for upper-level atmospheric fields, allows a 10-fold increase in the number of EPEs compared to previous studies.

A set of 887 EPEs is found and a subdivision in three predefined categories is proposed. First a subjective classification based on $\text{CAPE}_{\text{dmax}}$ and Tau_{dmax} is developed, then a combination of machine-learning methods (K-means and Random Forest) is applied to group EPEs into the three categories. Random Forest Classifier and feature importances methods turn out to be decisive in finding an optimal classification and for neglecting non-useful predictors. The resulting upper-level composites agree with the subjectively chosen categories in which we wanted to map our events.

From the analysis of the upper-level composites, different processes generating EPEs are recognized: frontal or mechanical orographic uplift of moist statically stable flow for Cat1, stronger frontal and mechanical uplift of a neutrally moister/warmer stable flow for Cat2, and finally thermally forced deep convective ascent for Cat3.

A common characteristic for all three categories is that IVT is anomalously high. EPEs are largely controlled by the intensity of the meridional component of integrated vapour transport IVT_n that in turn depends not only on moisture availability but also on a favourable phasing of the upper-level wave with respect to the target area. This confirms IVT as an important large-scale predictor, especially for Cat2 events, shown to be the most relevant category in terms of effects and EPE area extension. The importance of IVT as a predictor has been shown by Lavers *et al.* (2014; 2016), who demonstrated that it is possible to extend the range of predictability of extreme hydro-geological events if the integrated water vapour transport is directly employed instead of considering the precipitation from direct model output.

The proposed classification, based on widely used machine-learning methods, has the advantage that it can be easily applied elsewhere, since no subjective choice of fixed thresholds is necessary. The categorization of precipitation may introduce some simplifications compared to nature, but it is very useful for gaining a clearer picture of the basic processes. This approach can raise forecaster awareness of the origins of high impact weather phenomena and of different kind of EPEs, fostering a more critical interpretation of numerical model output. In addition, moving to research aspects, the study sets the stage to investigate the relation between EPEs and Rossby wave packets. This analysis will be conducted in Part II of this work with the intention of gaining insight into flow-dependent predictability for these three different categories. The value of the forecast is measured by its ability to predict critical situations and the skill of modern numerical weather prediction is highly flow-dependent, especially when convection is involved (Keil *et al.*, 2014; Nuissier *et al.*, 2016; Rodwell *et al.*, 2018). It is therefore important

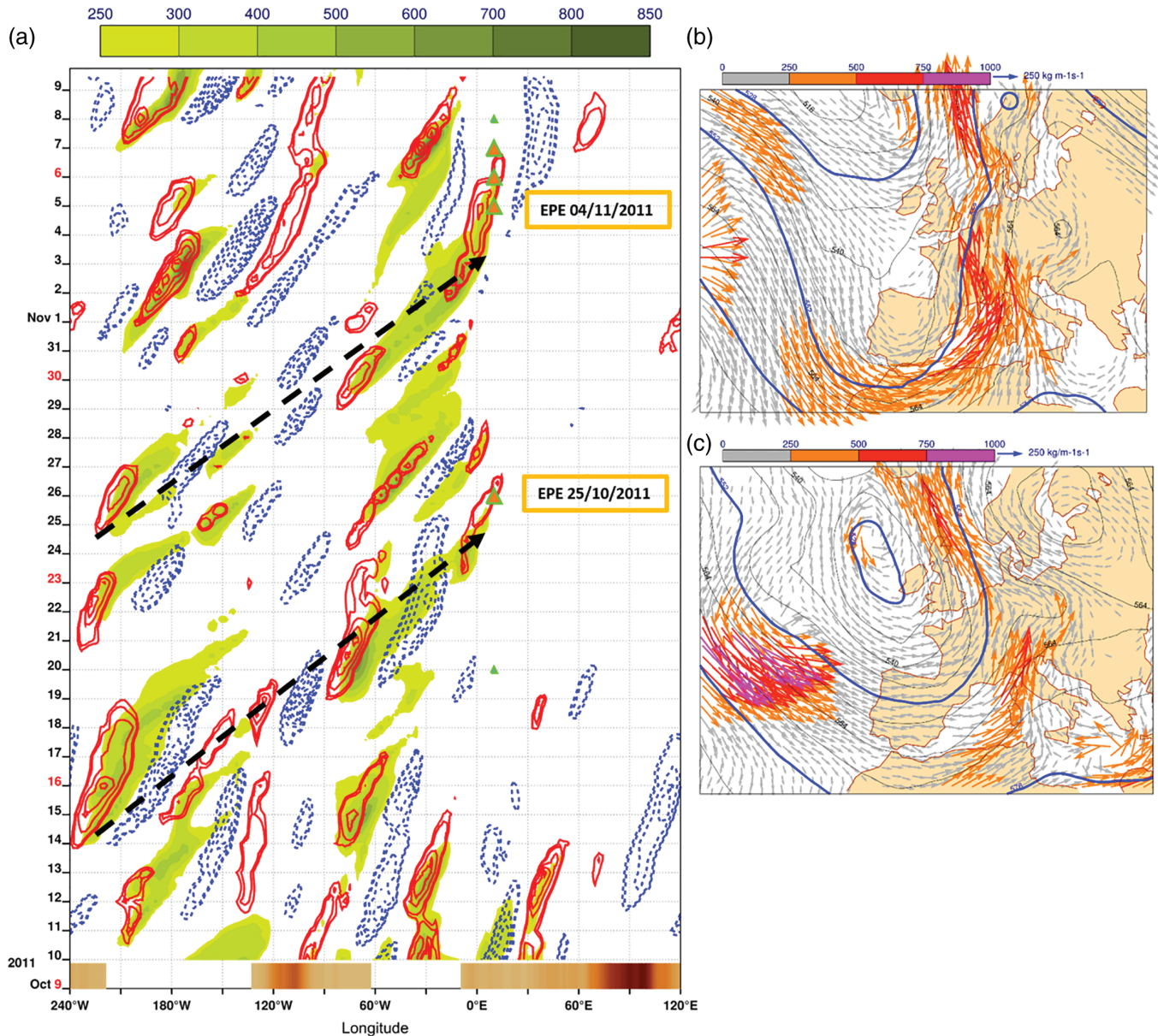


FIGURE 11 (a) Hovmüller diagram of RWP propagation during the period 9 October–10 November 2011, characterized by a significant EPE sequence. Red (continuous)/blue (dashed) lines show the meridional wind speed at 250 hPa (every 6 m/s, starting from 16 m/s). The green shaded areas represent the magnitude of IVT, starting from a threshold value of $250 \text{ kg m}^{-1} \text{ s}^{-1}$ which marks the atmospheric river lower limit. Fields are averaged over a band of latitude between 30°N and 60°N . EPE events in the target domain are marked by green triangles. The larger ones filled with orange colour are indicating Cat2 events. The two smaller triangles, respectively on the 20 October and 8 November are representing two smaller events of Cat3 and Cat1. Black dashed arrows mark RWPs associated with EPE. The brown shading, just above the longitude axis, provides a graphical impression of the distribution of the orography (white/sea, cream to dark brown/altitude) along the longitude. (b,c) Instantaneous Z500 and IVT for the two benchmark EPEs, 25 October and 4 November 2011, at 1200 UTC, respectively

to provide the meteorological operational community with a more process-based assessment of predictability as a foundation for a new forecasting methodology specifically designed for extreme precipitation events.

ACKNOWLEDGEMENTS

The results shown have been obtained within the subproject T1 of the Transregional Collaborative Research Centre

SFB/TRR 165 “Waves to Weather” (www.wavestoweather.de) funded by the German Research Foundation (DFG). We would like to acknowledge our collaboration partner ARPAE-SIMC (Bologna, Italy) for contributing with data and human resources to this project. We thank the Italian Department of Civil Protection for providing the shape files of the warning area units. We would also like to acknowledge Stefan Rasp (LMU) for insights and useful suggestions on machine-learning applications in atmospheric science.

ORCID

Federico Grazzini  <https://orcid.org/0000-0002-3435-2376>

Christian Keil  <https://orcid.org/0000-0003-2736-4309>

REFERENCES

- Breiman, L. (2001) Random forests. *Machine Learning*, 45(1), 5–32.
- Buzzi, A., Tartaglione, N. and Malguzzi, P. (1998) Numerical simulation of the 1994 Piedmont flood: role of orography and moist processes. *Monthly Weather Review*, 126, 2369–2383.
- Buzzi, A. and Tibaldi, S. (1978) Cyclogenesis in the lee of the Alps: a case study. *Quarterly Journal of the Royal Meteorological Society*, 104, 271–287. <https://doi.org/10.1002/qj.49710444004>.
- Craig, G.C. and Selz, T. (2018) Mesoscale dynamical regimes in the midlatitudes. *Geophysical Research Letters*, 45, 410–417. <https://doi.org/10.1002/2017GL076174>.
- Davolio, S., Volonté, A., Manzato, A., Pucillo, A., Cicogna, A. and Ferrario, M.E. (2016) Mechanisms producing different precipitation patterns over north-eastern Italy: insights from HyMeX-SOP1 and previous events. *Quarterly Journal of the Royal Meteorological Society*, 142, 188–205. <https://doi.org/10.1002/qj.2731>.
- Dee, D.P., Uppala, S.M., Simmons, A.J., Berrisford, P., Poli, P., Kobayashi, S., Andrae, U., Balmaseda, M.A., Balsamo, G., Bauer, P., Bechtold, P., Beljaars, A.C.M., van de Berg, L., Bidlot, J., Bormann, N., Delsol, C., Dragani, R., Fuentes, M., Geer, A.J., Haimberger, L., Healy, S.B., Hersbach, H., Hólm, E.V., Isaksen, I., Kållberg, P., Köhler, M., Matricardi, M., McNally, A.P., Monge-Sanz, B.M., Morcrette, J.-J., Park, B.-K., Peubey, C., de Rosnay, P., Tavolato, C., Thépaut, J.-N. and Vitart, F. (2011) The ERA-Interim reanalysis: configuration and performance of the data assimilation system. *Quarterly Journal of the Royal Meteorological Society*, 137, 553–597. <https://doi.org/10.1002/qj.828>.
- Done, J.M., Craig, G.C., Gray, S.L., Clark, P.A. and Gray, M.E.B. (2006) Mesoscale simulations of organized convection: importance of convective equilibrium. *Quarterly Journal of the Royal Meteorological Society*, 132, 737–756.
- Ducrocq, V., Braud, I., Davolio, S., Ferretti, R., Flamant, C., Jansa, A., Kalthoff, N., Richard, E., Taupier-Letage, I., Ayrat, P.-A., Belamari, S., Berne, A., Borga, M., Boudevillain, B., Bock, O., Boichard, J.-L., Bouin, M.-N., Bousquet, O., Bouvier, C., Chiggiato, J., Cimini, D., Corsmeier, U., Coppola, L., Cocquerez, P., Defer, E., Delanoë, J., Di Girolamo, P., Doerenbecher, A., Drobinski, P., Dufournet, Y., Fourrié, N., Gourley, J.J., Labatut, L., Lambert, D., Le Coz, J., Marzano, F.S., Molinié, G., Montani, A., Nord, G., Nuret, M., Ramage, K., Roussot, B.R.O., Said, F., Schwarzenboeck, A., Testor, P., van Baelen, J., Vincendon, B., Aran, M. and Tamayo, J. (2014) HyMeX-SOP1, the field campaign dedicated to heavy precipitation and flash-flooding in northwestern Mediterranean. *Bulletin of the American Meteorological Society*, 95, 1083–1100. <https://doi.org/10.1175/BAMS-D-12-00244.1>.
- Grazzini, F. (2007) Predictability of a large-scale flow conducive to extreme precipitation over the western Alps. *Meteorology and Atmospheric Physics*, 95, 123–138.
- Grazzini, F. and Vitart, F. (2015) Atmospheric predictability and Rossby wave packets. *Quarterly Journal of the Royal Meteorological Society*, 141, 2793–2802. <https://doi.org/10.1002/qj.2564>.
- Hohenegger, C., Lüthi, D. and Schär, C. (2006) Predictability mysteries in cloud-resolving models. *Monthly Weather Review*, 134, 2095–2107. <https://doi.org/10.1175/MWR3176.1>.
- Houssos, E.E., Lolis, C.J. and Bartzokas, A. (2008) Atmospheric circulation patterns associated with extreme precipitation amounts in Greece. *Advances in Geosciences*, 17, 5–11. <https://doi.org/10.5194/adeo-17-5-2008>.
- Isotta, F.A., Frei, C., Weilguni, V., Tadić, M.P., Lassègues, P., Rudolf, B., Pavan, V., Cacciamani, C., Antolini, G., Ratto, S.M., Munari, M., Micheletti, S., Bonati, V., Lussana, C., Ronchi, C., Panettieri, E., Marigo, G. and Vertačnik, G. (2014) The climate of daily precipitation in the Alps: development and analysis of a high-resolution grid dataset from pan-Alpine rain-gauge data. *International Journal of Climatology*, 34, 1657–1675. <https://doi.org/10.1002/joc.3794>.
- Keil, C., Heinlein, F. and Craig, G.C. (2014) The convective adjustment time-scale as indicator of predictability of convective precipitation. *Quarterly Journal of the Royal Meteorological Society*, 140, 480–490. <https://doi.org/10.1002/qj.2143>.
- Khodayar, S., Kalthoff, N. and Kottmeier, C. (2018) Atmospheric conditions associated with heavy precipitation events in comparison to seasonal means in the western Mediterranean region. *Climate Dynamics*, 51(3), 951–967.
- Kirshbaum, D.J., Adler, B., Kalthoff, N., Barthlott, C. and Serafin, S. (2018) Moist orographic convection: physical mechanisms and links to surface-exchange processes. *Atmosphere*, 9(3), 80.
- Kober, K., Craig, G.C. and Keil, C. (2014) Aspects of short-term probabilistic blending in different weather regimes. *Quarterly Journal of the Royal Meteorological Society*, 140, 1179–1188. <https://doi.org/10.1002/qj.2220>.
- Lavers, D.A., Pappenberger, F. and Zsoter, E. (2014) Extending medium-range predictability of extreme hydrological events in Europe. *Nature Communications*, 5, 5382. <https://doi.org/10.1038/ncomms6382>.
- Lavers, D.A. and Villarini, G. (2013) The nexus between atmospheric rivers and extreme precipitation across Europe. *Geophysical Research Letters*, 40, 3259–3264. <https://doi.org/10.1002/grl.50636>.
- Lavers, D.A. and Villarini, G. (2015) The relationship between daily European precipitation and measures of atmospheric water vapour transport. *International Journal of Climatology*, 35, 2187–2192. <https://doi.org/10.1002/joc.4119>.
- Lavers, D.A., Waliser, D.E., Ralph, F.M. and Dettinger, M.D. (2016) Predictability of horizontal water vapor transport relative to precipitation: enhancing situational awareness for forecasting western U.S. extreme precipitation and flooding. *Geophysical Research Letters*, 43, 2275–2282. <https://doi.org/10.1002/2016GL067765>.
- Lee, K., Flamant, C., Ducrocq, V., Duffourg, F., Fourrié, N. and Davolio, S. (2016) Convective initiation and maintenance processes of two back-building mesoscale convective systems leading to heavy precipitation events in southern Italy during HyMeX IOP 13. *Quarterly Journal of the Royal Meteorological Society*, 142, 2623–2635. <https://doi.org/10.1002/qj.2851>.
- Llasat, M.C. (2001) An objective classification of rainfall events on the basis of their convective features: application to rainfall intensity in the northeast of Spain. *International Journal of Climatology*, 21, 1385–1400.
- Malguzzi, P., Grossi, G., Buzzi, A., Ranzi, R. and Buizza, R. (2006) The 1966 “century” flood in Italy: a meteorological and hydrological revisit. *Journal of Geophysical Research*, 111, D24106. <https://doi.org/10.1029/2006JD007111>.

- Martius, O., Schwierz, C. and Davies, H.C. (2008) Far-upstream precursors of heavy precipitation events on the Alpine south-side. *Quarterly Journal of the Royal Meteorological Society*, 134, 417–428. <https://doi.org/10.1002/qj.229>.
- Massacand, A.C., Wernli, H. and Davies, H.C. (1998) Heavy precipitation on the Alpine southside: an upper-level precursor. *Geophysical Research Letters*, 25, 1435–1438.
- McGovern, A., Elmore, K.L., Gagne, D.J., Haupt, S.E., Karstens, C.D., Lagerquist, R., Smith, T. and Williams, J.K. (2017) Using artificial intelligence to improve real-time decision-making for high-impact weather. *Bulletin of the American Meteorological Society*, 98, 2073–2090. <https://doi.org/10.1175/BAMS-D-16-0123.1>.
- Molini, L., Parodi, A., Rebora, N. and Craig, G.C. (2011) Classifying severe rainfall events over Italy by hydrometeorological and dynamical criteria. *Quarterly Journal of the Royal Meteorological Society*, 137, 148–154.
- Montanari, A. (2012) Hydrology of the Po River: looking for changing patterns in river discharge. *Hydrology and Earth System Sciences*, 16, 3739–3747. <https://doi.org/10.5194/hess-16-3739-2012>.
- Morel, C. and Senesi, S. (2002) A climatology of mesoscale convective systems over Europe using satellite infrared imagery. II: Characteristics of European mesoscale convective systems. *Quarterly Journal of the Royal Meteorological Society*, 128, 1973–1995. <https://doi.org/10.1256/003590002320603494>.
- Nuissier, O., Joly, B., Joly, A., Ducrocq, V. and Arbogast, P. (2011) A statistical downscaling to identify the large-scale circulation patterns associated with heavy precipitation events over southern France. *Quarterly Journal of the Royal Meteorological Society*, 137, 1812–1827. <https://doi.org/10.1002/qj.866>.
- Nuissier, O., Marsigli, C., Vincendon, B., Hally, A., Bouttier, F., Montani, A. and Paccagnella, T. (2016) Evaluation of two convection-permitting ensemble systems in the HyMeX Special Observation Period (SOP1) framework. *Quarterly Journal of the Royal Meteorological Society*, 142, 404–418. <https://doi.org/10.1002/qj.2859>.
- Pavan, V., Antolini, G., Barbiero, R., Berni, N., Brunier, F., Cacciamani, C., Cagnati, A., Cazzuli, O., Cicogna, A., De Luigi, C., Di Carlo, E., Francioni, M., Maraldo, L., Marigo, G., Micheletti, S., Onorato, L., Panettieri, E., Pellegrini, U., Pelosini, R., Piccinini, D., Ratto, S., Ronchi, C., Rusca, L., Sofia, S., Stelluti, M., Tomozeiu, R. and Malaspina, T.T. (2019) High resolution climate precipitation analysis for north-central Italy, 1961–2015. *Climate Dynamics*, 52, 3435–3453. <https://doi.org/10.1007/s00382-018-4337-6>.
- Pedregosa, F., Varoquaux, G., Gramfort, A., Michel, V., Thirion, B., Grisel, O., Blondel, M., Prettenhofer, P., Weiss, R., Dubourg, V., Vanderplas, J., Passos, A., Cournapeau, D., Brucher, M., Perrot, M. and Duchesnay, É. (2011) Scikit-learn: machine learning in Python. *Journal of Machine Learning Research*, 12, 2825–2830.
- Pfahl, S., Madonna, E., Boettcher, M., Joos, H. and Wernli, H. (2014) Warm conveyor belts in the ERA-Interim dataset (1979–2010). Part II: Moisture origin and relevance for precipitation. *Journal of Climate*, 27, 27–40.
- Piaget, N., Froidevaux, P., Giannakaki, P., Gierth, F., Martius, O., Riemer, M., Wolf, G. and Grams, C.M. (2014) Dynamics of a local Alpine flooding event in October 2011: moisture source and large-scale circulation. *Quarterly Journal of the Royal Meteorological Society*, 141, 1922–1937. <https://doi.org/10.1002/qj.2496>.
- Pinto, J.G., Ulbrich, S., Parodi, A., Rudari, R., Boni, G. and Ulbrich, U. (2013) Identification and ranking of extraordinary rainfall events over northwest Italy: the role of Atlantic moisture. *Journal of Geophysical Research: Atmospheres*, 118, 2085–2097. <https://doi.org/10.1002/jgrd.50179>.
- Raveh-Rubin, S. and Wernli, H. (2015) Large-scale wind and precipitation extremes in the Mediterranean – a climatological analysis for 1979–2012. *Quarterly Journal of the Royal Meteorological Society*, 141, 2404–2417. <https://doi.org/10.1002/qj.2531>.
- Rebora, N., Molini, L., Casella, E., Comellas, A., Fiori, E., Pignone, F., Siccardi, F., Silvestro, F., Tanelli, S. and Parodi, A. (2013) Extreme rainfall in the Mediterranean: what can we learn from observations? *Journal of Hydrometeorology*, 14, 906–922.
- Rodwell, M.J., Richardson, D.S., Parsons, D.B. and Wernli, H. (2018) Flow-dependent reliability: a path to more skillful ensemble forecasts. *Bulletin of the American Meteorological Society*, 99, 1015–1026. <https://doi.org/10.1175/BAMS-D-17-0027.1>.
- Rousseeuw, P., J. (1987) Silhouettes: a graphical aid to the interpretation and validation of cluster analysis. *Computational and Applied Mathematics*, 20, 53–65.
- Trigo, I.F., Bigg, G.R. and Davies, T.D. (2002) Climatology of cyclogenesis mechanisms in the Mediterranean. *Monthly Weather Review*, 130, 549–569. <https://doi.org/10.1175/1520-0493>.
- Walther, A. and Bennartz, R. (2006) Radar-based precipitation type analysis in the Baltic area. *Tellus A*, 58(3), 331–343. <https://doi.org/10.1111/j.1600-0870.2006.00183.x>.
- Winschall, A. (2013) *Evaporative moisture sources for heavy precipitation events*. PhD Thesis, ETH Zurich. <https://doi.org/10.3929/ethz-a-009755505>.
- Winschall, A., Sodemann, H., Pfahl, S. and Wernli, H. (2014) How important is intensified evaporation for Mediterranean precipitation extremes? *Journal of Geophysical Research: Atmospheres*, 119, 5240–5256. <https://doi.org/10.1002/2013JD021175>.
- Zimmer, M., Craig, G.C., Keil, C. and Wernli, H. (2011) Classification of precipitation events with a convective response timescale and their forecasting characteristics. *Geophysical Research Letters*, 38, L05802. <https://doi.org/10.1029/2010GL046199>.

SUPPORTING INFORMATION

Additional supporting information may be found online in the Supporting Information section at the end of this article.

How to cite this article: Grazzini F, Craig GC, Keil C, Antolini G, Pavan V. Extreme precipitation events over northern Italy. Part I: A systematic classification with machine-learning techniques. *Q J R Meteorol Soc.* 2020;146:69–85. <https://doi.org/10.1002/qj.3635>

3.2 An archetypal EPE: The Piedmont 1994 case study



The 1994 Piedmont flood: an archetype of extreme precipitation events in Northern Italy

F. Grazzini^{1,3}  · G. Fragkoulidis² · V. Pavan³ · G. Antolini³

Received: 18 April 2020 / Accepted: 26 August 2020 / Published online: 01 September 2020
© The Author(s) 2020

Abstract

Extreme precipitation events (EPEs) are meteorological phenomena of major concern for the densely populated regions of northern and central Italy. Although statistically rare, they tend to be recurrent in autumn and share common characteristics in the large-scale dynamical evolution responsible for their generation. Past studies on EPEs have reported, as the main triggering factor, a meridionally elongated upper-level trough embedded in an incoming Rossby wave packet. In this respect, we show how the meteorological conditions leading to the devastating 1994 Piedmont flood represent a typical flow evolution for this type of extreme events. Exploiting the systematic classification of EPEs recently published by the authors and taking advantage of a new observational dataset, this article revisits the role of the large-scale flow on this and similar cases of past EPEs.

Keywords Extreme precipitation · Floods · Po river · Atmospheric rivers · Rossby wave packets · Downstream development

1 Introduction

The extreme precipitation that affected the Piedmont region, in Northern Italy, in November 1994 led to a destructive flood with significant socioeconomic impacts. Seventy people died, and more than two thousand had to be evacuated. Damage to public and private property was extensive, 150 bridges collapsed or were severely damaged, and more than 5000 head of livestock were lost (Buzzi et al. 1998).

The heaviest precipitation occurred between 4 and 6 of November when several rain gauges in mountainous regions recorded accumulated values above 300 mm/36 h (Buzzi and

✉ F. Grazzini
Federico.Grazzini@lmu.de

¹ Meteorologisches Institut, Ludwig-Maximilians-Universität, Munich, Germany

² Institute for Atmospheric Physics, Johannes Gutenberg University Mainz, Mainz, Germany

³ ARPAE-SIMC, Bologna, Regione Emilia-Romagna, Italy

Tartaglione, 1995). Forty percent of the Piedmont territory received more than 200 mm of rain during the event (Arpa Piemonte 1998). The large-scale circulation was characterized by a Rossby wave with meridional extension from the British Isles to the Iberian Peninsula featuring an elongated trough over Western Europe and a blocking anticyclone over Central Europe. Extreme precipitation events (EPEs), like this one, are typically associated with a strongly confluent flow ahead of a polar cold front concentrating water vapour into a narrow plume, which then interacts with the orography (Krichak et al. 2015). Such a flow can be triggered by a breaking Rossby wave over Western Europe that takes the form of a PV streamer, an elongated filament of high potential vorticity (PV) air (Grazzini, 2007, Martius et al. 2008). Since most of the intense orographic precipitation falls in the prefrontal sector, it is essential to study the characteristics of the flow and the associated water vapour transport.

Based on the EPE categorization presented in Grazzini et al., 2020a; (hereafter, G2020), in which the authors classify EPEs into three categories, in the present paper, we discuss the large-scale circulation characteristics leading to the 1994 Piedmont flood and evaluate its similarities with other cases. Following a statistical approach, Grazzini et al. (2020b) investigated the upstream large-scale precursors which influence the frequency and intensity of EPEs. Revisiting the dynamics of the 1994 event might be useful to reveal the processes leading to such an extreme. Highlighting them is essential in the quest for better predictability and impact assessment of future events.

In this article, we will retrace the evolution of the event starting from the description of the regional precipitation pattern and the corresponding synoptic situation and then investigating the spatiotemporal evolution of the associated wave packet at larger scales. The paper is organized as follows. In Section 2, we describe the dataset and the key variables used to analyse the event. In Section 3, we comment on the observed daily precipitation and classification of the event. In Section 4, we discuss the genesis and characteristics of the synoptic pattern associated with the event, while in Section 5, we highlight the key role of the moisture transport and we contrast this case with more recent analogues. Conclusions follow in Section 6.

2 Data and methods

The atmospheric fields used in this study are retrieved from the ERA5 reanalysis (Hersbach et al. 2020), while precipitation data, upon which the EPE definition is based, are retrieved from the new observational dataset ARCIS (Archivio Climatologico per l'Italia Centro Settentrionale). ARCIS is a recently assembled gridded precipitation dataset (with a resolution of 5 km) derived from 1762 rain gauges from 11 regional networks in Northern-Central Italy and several stations of adjacent Alpine regions (Pavan et al. 2019). The dataset has a daily temporal resolution and covers the period 1961–2015. The input data are checked for quality, time consistency, synchronicity, and statistical homogeneity and then spatially interpolated using a modified Shepard's scheme. The 24-h accumulation period corresponds to the best practice of the Italian Hydrological Service, i.e. from 08 to 08 UTC of the following day.

Based on this dataset, EPEs are defined and classified as follows. Precipitation is aggregated over the official warning areas (WAs) provided by the Italian Department of Civil Protection. This choice, preferable to regular boxes, allows averaging precipitation on subregional hydrological basins which are considered climatologically homogenous. Northern-Central Italy is subdivided into 94 WAs, shown in Fig. 1. EPEs are defined as days with

daily precipitation greater than or equal to the 99th percentile across one or more WAs. Subsequently, the meteorological variables listed in Table 1 are used as predictors for the EPE classification as described in G2020. Among these variables, central in the following considerations is the magnitude of the integrated water vapour transport (IVT), as well as its zonal (IVTe) and meridional (IVTn) components. Their instantaneous fields in ERA5 are computed as the integral (over model levels, from the surface to the top of the atmosphere) of the wind component multiplied by the specific humidity at each level. Positive values of IVTe indicate an eastward flux, and positive IVTn values indicate a northward flux.

3 Observed precipitation and event classification

Figure 1 shows the daily accumulated precipitation patterns that led to the Piedmont flood as analysed with the ARCIS dataset which, compared with the raw data of the dense regional networks, has the advantages of being gridded, spatially homogeneous, and not limited to single administrative regions. The precipitation event is prolonged, with very high intensity, especially during the 24-h period from 5 November 08 UTC to 6 November 08 UTC. In this period, daily values above 300 mm were recorded on the northern and western borders of the Piedmont region associated with persistent orographic uplift, while on the southern side of the region, on the border with Liguria, hourly rates in excess of 30 mm/h were reported in a few stations, due to strong convective activity (Arpa Piemonte, 1998).

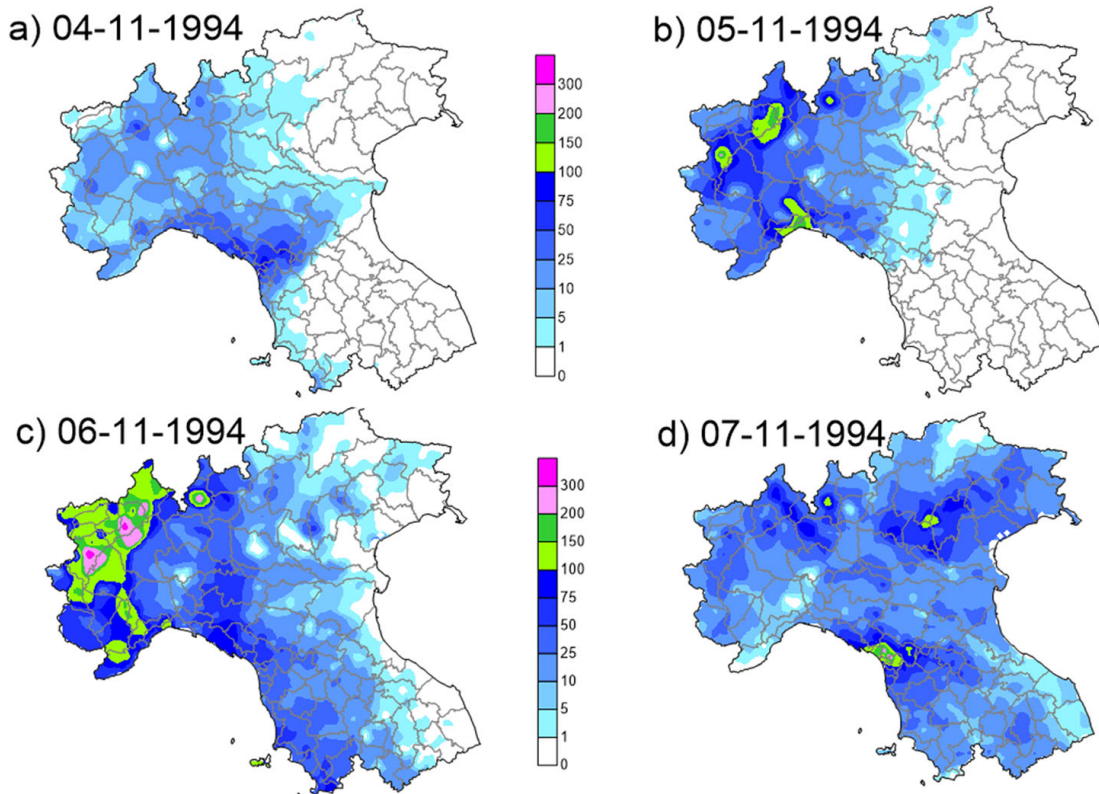


Fig. 1 Gridded daily total precipitation from the ARCIS dataset of high-resolution regional observational networks (mm/24 h). Note that the dates on the panels refer to the end of the 24 h accumulation period 08-08 UTC. The areas in the foregrounds are the Italian Civil Protection Warning Areas used for operational warnings

Table 1 Predictors used in the EPE classification algorithm of G2020

Variable	Description	Units
τ_{dmax}	Daily maximum convective adjustment time scale	h
$CAPE_{dmax}$	Daily maximum convective available potential energy	J kg ⁻¹
IVTe	Daily mean zonal component of integrated water vapour transport (from the surface up to the top of atmosphere)	kg m ⁻¹ s ⁻¹
IVTn	Daily mean meridional component of integrated water vapour transport (from the surface up to the top of the atmosphere)	kg m ⁻¹ s ⁻¹
θ_{e850}	Daily mean equivalent potential temperature at 850 hPa	K
$\Delta\theta_{e500-850_dmin}$	Daily minimum θ_e difference between 500 and 850 hPa	K
TCWV	Daily mean total column water vapour	kg m ⁻²
$BS_{500_925_dmax}$	Daily maximum wind bulk shear between 500 and 925 hPa	m s ⁻¹

For each EPE day, the instantaneous values of the variables are spatially averaged over Northern-Central Italy and aggregated daily, as reported in the table. See G2020 for further details on variable definitions and averaging methods

Compared with the 887 EPEs found in G2020, we notice that the 1994 Piedmont event, although not characterized by an extreme spatial extension (ranked only 32nd in this respect), presents one of the highest area average precipitation intensities. In Table 2 we show precipitation data and the values of atmospheric variables used for the classification of this event. A very similar event, which caused the historical Po river flood in October 2000, is also included in Table 2. The intensity on 5 November 1994 (see the column mmkm² in Table 2) is just slightly lower and comparable with the one on 14/10/2000, which is the maximum precipitation average intensity recorded among all EPEs.

The next question to address is in which category this event is classified. Here we briefly recall the definition of the three categories in which subdivide EPEs following G2020. Category 1 (Cat1) events originate from intense frontal structures, including slantwise ascent in the warm sector of the associated cyclones (warm conveyor belt). Mechanical (orographic) uplift of low-level marine, statically stable air is the key factor to attain extreme precipitation that is mostly confined over upwind steep topography. Category 2 (Cat2) events originate from

Table 2 Relevant data for two recent historical Po river floods, 4–6 November 1994 and 11–16 October 2000

Day	#WA	Area	mmkm ²	IVTe	IVTn	τ_{dmax}	$CAPE_{dmax}$	TCWV	θ_{e850}	Dtmin	Cat
04/11/1994	7	15.8	68.0	-23.4	148.1	2.2	66.2	23.2	315.5	2.3	2
05/11/1994	20	33.3	97.7	-66.7	234.5	4.7	97.2	21.6	314.2	3.7	2
06/11/1994	9	12.7	66.6	-24.6	150.5	1.3	77.6	19.8	309.8	5.1	2
11/10/2000	8	11.3	77.1	198.4	208.7	1.3	63.2	19.5	311.3	8.8	2
12/10/2000	3	3.0	61.0	148.9	281.1	4.5	220.0	21.5	317.4	1.0	2
13/10/2000	7	9.3	94.8	-20.0	306.3	6.7	319.5	23.0	320.3	-1.9	2
14/10/2000	17	32.4	103.4	-120.8	296.1	5.1	184.9	25.7	321.2	0.5	2
15/10/2000	12	23.9	69.9	-153.8	254.2	2.5	114.6	23.3	316.8	3.2	2

#WA number of warning areas with spatial daily average precipitation exceeding the 99th percentile of the respective climatological distribution, *Area* total area exceeding the 99th percentile of daily precipitation [10³ km²], *mmkm²* mean area daily precipitation intensity [mm/24 h km²], *IVTe* mean zonal component of IVT [kg s⁻¹ m⁻¹], *IVTn* mean meridional component of IVT [kg s⁻¹ m⁻¹], τ_{dmax} maximum daily value of Tau [hours], $CAPE_{dmax}$ daily maximum value of CAPE [J/kg], *TCWV* daily mean of total column water vapour [kg/m²], θ_{e850} daily mean of equivalent potential temperature at 850 hPa [K], *Dtmin* daily minimum of $\Delta\theta_e$ [K] ($\Delta\theta_e = \theta_{e500} - \theta_{e850}$), *Cat* the EPE category. Atmospheric variables are spatially averaged over Northern-Central Italy (roughly corresponding to the area covered by ARCIS dataset) and aggregated daily. The maximum intensity days of the two events are in italics

a synergic combination of frontal uplift and embedded deep convection. They are characterized by a stronger southerly flow component and a reduced moist static stability (almost neutral conditions). Category 3 (Cat3) events are associated with weakly forced convection (non-equilibrium convective events) in a potentially unstable environment (i.e. with very high CAPE). According to the classification method, which is based on the dynamic and thermodynamic predictors listed in Table 1, all the days of the 1994 Piedmont flood episode, as well as the days of the October 2000 event, qualify as Cat2 EPE days, as indicated in Table 2.

In order to provide further evidence for the classification of the event and describe in more detail the relevant processes, Fig. 2 displays the patterns of the ERA5 reanalysis low-level wind at 18 UTC on 5 November 1994 (panel b) and the 06–24 UTC accumulated precipitation from the ERA5 forecast initiated at 06 UTC of the same day (panel a). The precipitation pattern shows two main precipitation areas, on the northern side of the Piedmont region, indicated by the grey arrow, and on the southern side, on the border with Liguria, indicated by the yellow arrow (also evident in Fig. 1b). The partition of precipitation to convective and large scale (or “stratiform”) is based on the corresponding definitions and numerical schemes used in ECMWF forecasts and ERA5 (Owens and Hewson, 2018). The red-dashed contours, which indicate the convective fraction, suggest that these two peaks are attributable to two distinct processes. The precipitation peak indicated by the grey arrow is mainly due to orographically enhanced stratiform precipitation which may have had some isolated convective element in it, while the other peak indicated by the yellow arrow lies just on the border of a region where deep convection is predominant (up to 80% of the precipitation amount resulted from the convection scheme of the model).

Figure 2 b provides further information on the observed differences in precipitation type. The red isoline, representing the values of 2 potential vorticity units (PVU) at 330 K, marks the position of the forward side of the upper-level trough (see also Fig. 3). Ahead of it, the cold

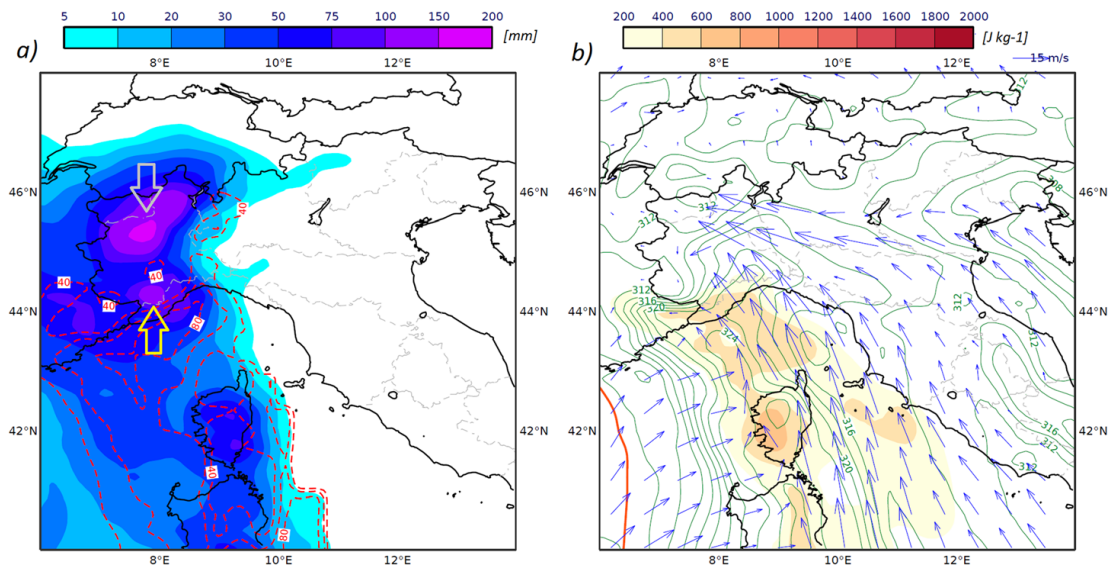


Fig. 2 **a** 18-h accumulated precipitation from 06 UTC to 24 UTC 5 November 1994 in the ERA5 short-term forecast initialized at 06 UTC. The shaded field depicts the total precipitation (mm), while the red dashed contours indicate the convective fraction estimated as the ratio of the convective over the total precipitation in ERA5. Isolines are drawn every 20%, starting from 40%. **b** Synoptic situation derived from the ERA5 hourly reanalysis and valid at 18 UTC of the same day, at about the time of maximum convergence of the southerly and easterly branch of the low level jets. The shaded field is CAPE [J kg^{-1}], the arrows indicate the wind vectors at 925 hPa, the green contours are θ_e at 850 hPa (every 2 K), and the red contours mark the 2PVU contour at 330 K

front is evident and represented by the tight zonal gradient in θ_e at 850 hPa, indicated by the green contours. A key feature is the very intense low-level flow (blue arrows) at 925 hPa, which blows northward in the warm sector. This intensifies and splits in two low-level jet (LLJ) branches during the day. The first one, flowing from the Tyrrhenian sea towards the Ligurian coast, is channelling warm moist (high θ_e values around or above 320 K) maritime air masses in a narrow band ahead of the cold front. This air mass is also relatively unstable with values of CAPE in the order of 500 Jkg^{-1} and has relatively low-convective inhibition. In this airstream, convection is triggered over the sea, by forced uplift over the Ligurian Apennines and later by the approach of the cold front. A second low-level jet blowing from south-east forms on the Po valley due to the blocking action of the orography on more stable air masses, a typical example of barrier wind (Buzzi et al. 2020). The mass convergence of these two branches in the western Po valley triggered high vertical velocities on the upwind side of the orography, generating intense and persistent orographic precipitation. A comparison with the radio sounding data from Ajaccio (Corsica) and San Pietro Capofiume (Emilia-Romagna region, Po valley), Milano Linate (Lombardy region, Po valley) confirms the different characteristics of the two airstreams with the Po valley LLJ being very shallow and stable although very intense, in the order of 20 m s^{-1} (not shown).

The 1994 Piedmont event was also characterized by a strong IVT band at the eastern flank of the upper-level trough (Fig. 3) with a magnitude constantly higher than the atmospheric river (AR) definition threshold of $250 \text{ kg s}^{-1} \text{ m}^{-1}$. In addition, the total column water content

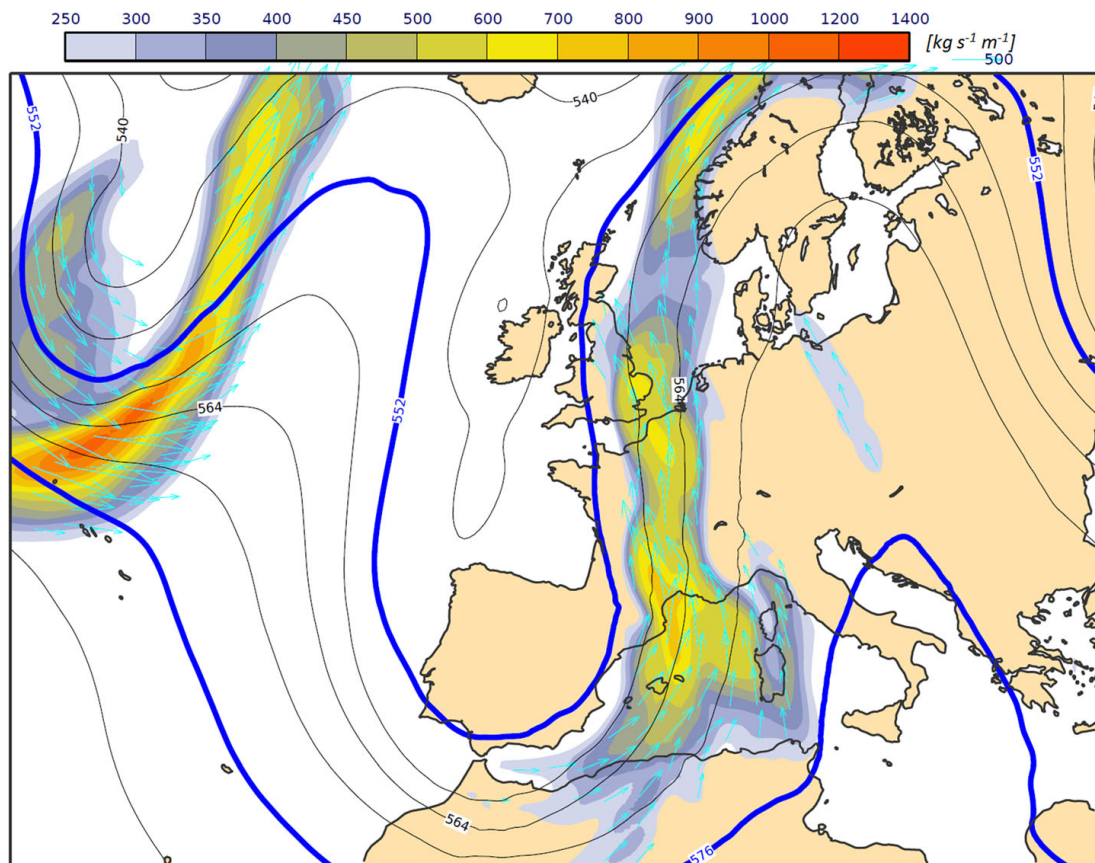


Fig. 3 Synoptic view of the 1994 Piedmont flood on 5 November 1994 00 UTC by the ERA5 reanalysis. Contours show geopotential height at 500 hPa (every 6 dam), the colour shading refers to the IVT magnitude [$\text{kg s}^{-1} \text{ m}^{-1}$], and the cyan arrows indicate IVT vectors, drawn where the IVT magnitude exceeds the AR threshold of $250 \text{ kg s}^{-1} \text{ m}^{-1}$

(TCWV) was greater than 20 kg m^{-2} . This allows us to affirm that the strong southerly moist flow ahead of the cold front can be classified as an AR, a circumstance also confirmed by Krichak et al. 2015.

As we have seen through the examination of the reanalysis fields, this event presents the key features that are typical of category 2 events, i.e., the abnormally strong flow from the south and the presence of both large-scale and deep convection precipitation peaks. The dynamic and thermodynamic characteristics of this event described herein agree with previous studies obtained with limited area model simulations (Ferretti et al. 2000, Cassardo et al. 2002). In particular, Cassardo et al. (2002) reported that the persistence of deep convection further contributed to the severity of the event over the Ligurian range.

4 Synoptic evolution and large-scale precursors

As stated above, the presence of a strong southerly airstream, classifiable as AR, is a crucial feature which characterizes this event as well as many other EPEs in the Alpine region. In this section, we discuss the origin and dynamical evolution responsible for its occurrence. For this purpose, we present two figures. Figure 4 shows the synoptic wave and the associated IVT on 4 November at 12 UTC, at the initial phase of the event. Figure 5 displays, in a compact way, the dynamical evolution of the upper-tropospheric flow and the associated Rossby wave packets (RWPs) which set the stage for the smaller-scale processes that eventually lead to the event. Figure 5 depicts the meridional wind component at 300 hPa, the corresponding envelope E, as well as the 2 PVU contour at 330 K on selected days leading to the event. The envelope field, diagnosed following Fragkoulidis et al. (2018), highlights the regions where the RWP amplitude is strong, i.e. the upper-tropospheric jet exhibits pronounced undulations.

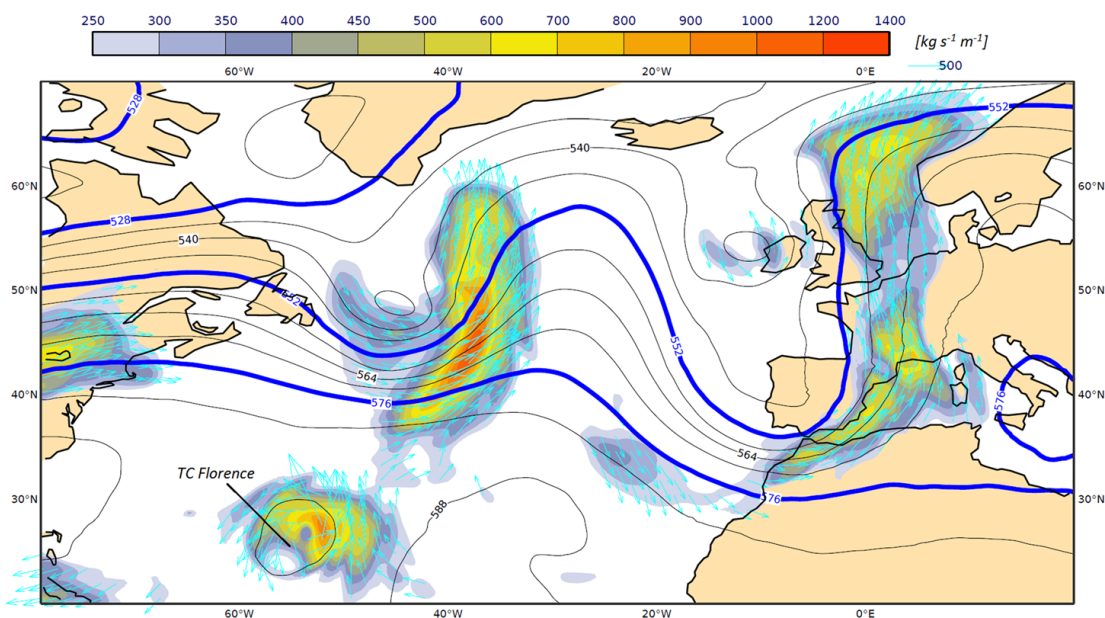


Fig. 4 Synoptic configuration on 4 November 1994 12UTC over the Atlantic basin. Contours show geopotential height at 500 hPa, every 6 dam, the colour shading refers to the IVT magnitude [$\text{kg s}^{-1} \text{m}^{-1}$] (see colour bar above), and the cyan arrows are IVT vectors, drawn only when the IVT magnitude exceeds the AR threshold of 250 [$\text{kg s}^{-1} \text{m}^{-1}$]

This is also reflected in the large meridional wind anomaly (v') values and the associated succession of troughs and ridges that result in a wavy 2 PVU contour.

The moist airstream that was crucial for the extreme precipitation event grew ahead and in response to a developing trough over the eastern Atlantic on 2 November (Fig. 5b). The narrow band of strong IVT associated with the trough can be identified in Fig. 3, where values exceeding the AR thresholds become evident already from 4 November (Fig. 4). Overall, the

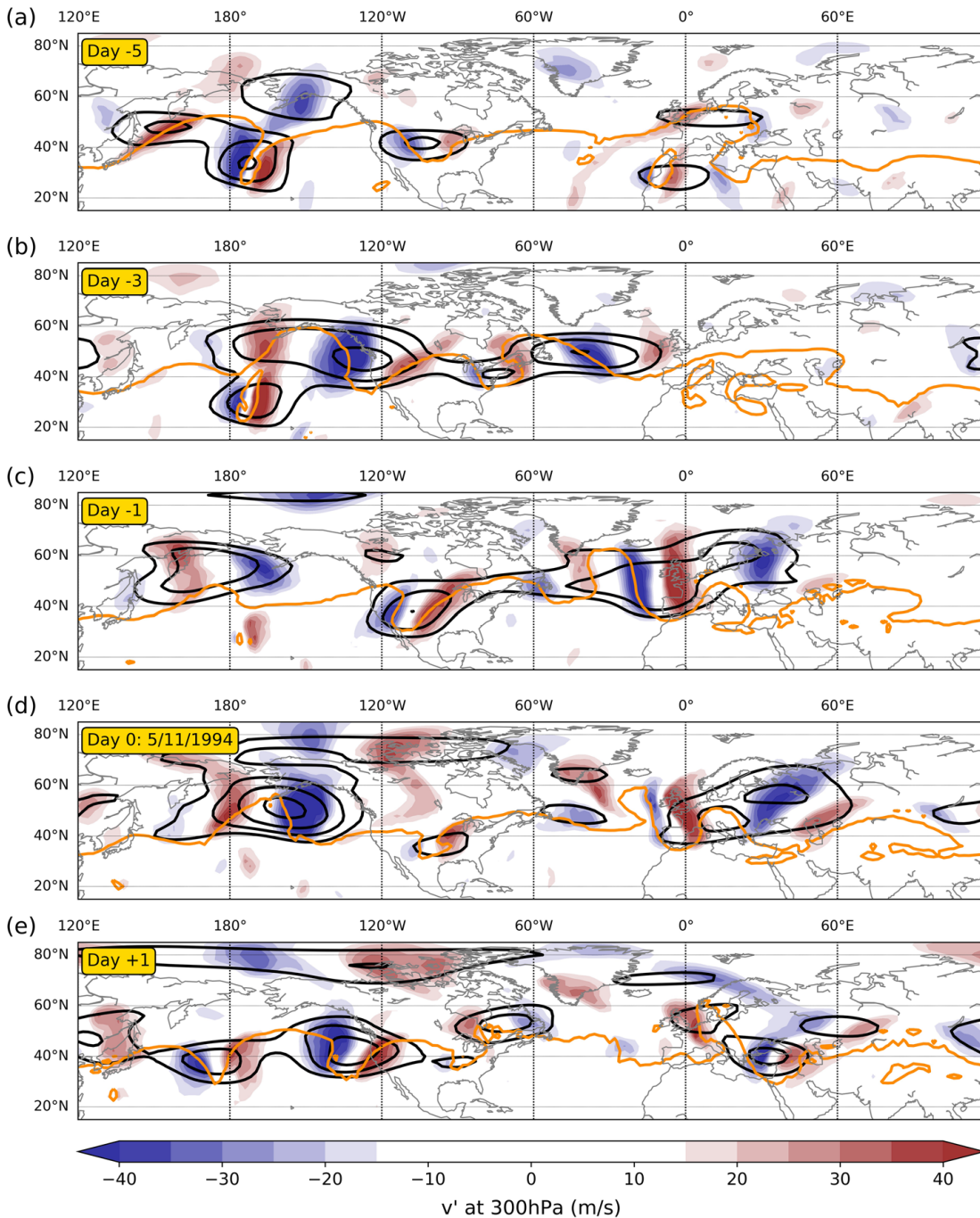


Fig. 5 Evolution of the upper-tropospheric flow leading to the November 1994 Piedmont flood. The panels depict mean daily values of meridional wind at 300 hPa (colour fill), the corresponding E at 300 hPa (black contours every 10 m/s starting from 25 m/s) and the 2 PVU isoline at 330 K (orange contour) at **a** 31 October 1994 (D-5), **b** 02 November 1994 (D-3), **c** 04 November 1994 (D-1), **d** 05 November 1994 (D0), and **e** 06 November 1994 (D+1). All maps show instantaneous values at 12 UTC

AR stretches from the Azores to the North Sea. In Fig. 4, the presence of hurricane Florence in the central Atlantic is also evident. A closer inspection of a sequence of snapshots around 4 November reveals that the circulation and moisture fluxes induced by Florence have interacted with the trough to the north and the associated upper-level jet. This may have indirectly influenced the evolution of the N. Atlantic wave packet propagating towards the Mediterranean. As can be seen from Fig. 4, there seems to be a connection in the IVT fluxes from the tropical cyclone to the trough in the central Atlantic, later visible in the wind field at 250 hPa (not shown). In this respect, as documented in several other occasions (Grams and Archambault 2016, Pohorsky et al. 2019), the low-PV air injection into the mid-latitude jet can cause a jet acceleration and a ridge building, thus strengthening the development of the trough downstream (in our case over the Mediterranean). A strong downstream development, possibly connected with anomalous water vapour fluxes in the upstream trough, is frequently observed in Cat2 events and this evolution is extensively investigated in Grazzini et al. (2020b).

In the following hours, the slow eastward movement and amplification of the synoptic wave pattern over Western Europe modulated a strong moisture transport and convergence towards the western Alpine region. This situation further intensified on 5 November, when the trough axis advanced slightly eastward, while the downstream ridge centred over the Adriatic Sea almost kept its position and amplified (Figs. 3, 5). Also note that at that time, a channelling of the AR between the largest Mediterranean islands (Sardinia and Corsica) and the continent is evident. This channelling may be responsible for the prefrontal precipitation during the night between 4 and 5 November. In Fig. 5 we note the northward expansion of the ridge in the orange PV contour on the Mediterranean, from 4 (panel c) to 5 November (panel d), presumably also affected by the low-PV outflow associated with the deep convection over northern Italy.

The synergic interaction between convection and the large-scale environment described above is typical of Cat2 events as discussed in G2020. It may arise from temporary positive feedback from the synoptic flow that, through mass convergence, favours local convection to grow into mesoscale systems, which in turn enhance low-PV air export into the upper levels, contributing to ridge amplification and further strengthening of mass convergence. However, the interaction of the large-scale flow and local mesoscale deep convective systems is not yet fully understood and deserves further investigation.

Finally, we briefly discuss the dynamical evolution of the RWP associated with the trough over the Mediterranean. The time reference (day 0, D0) is set on the day of maximum intensity, i.e. on 5 November at 12 UTC. On D-5, a RWP of large amplitude is located over the central Pacific, highlighted by the black contours (E) in Fig. 5a centred on a narrow PV streamer east of the dateline. On D-3 (2 November, panel b), the disturbance is growing and propagating rapidly over North America, inducing a new couplet (ridge-trough) development over the western North Atlantic, with the latter subsequently approaching western Europe. On D-1, the amplified trough remains over Western Europe and constitutes the stronger part of the RWP and the dominant flow feature associated with the EPE synoptic pattern. An apparent overturning and wave breaking between D0 and D+1 over eastern North Atlantic are well depicted by the 2 PVU contour. At the same time, v' and E get fragmented and imply an incoherent RWP at its decay stage.

This short analysis points to the remote origin of the RWP associated with the trough, which could be traced back to western-central Pacific 6 to 5 days before. The long lifetime and coherence of the wave packet may have played a role in determining the good predictability of

the large-scale flow in the medium-range forecasts, experienced even in the not so advanced operational systems of that time (Ferrero and Balsamo 2020). The statistical relation between long spatial and temporal coherence of RWPs and increased forecast skill was already reported by Grazzini and Vitart (2015).

5 Comparison with other similar EPEs

In this section, we compare this event to others that have recently affected the southern part of the Alpine area to identify analogies and threshold values for key features of the large-scale flow. As mentioned in several works (Ralph and Dettinger, 2011, Lavers and Villarini 2013, Krichak et al. 2015, Froidevaux and Martius, 2016), IVT represents an optimal integral variable to account for the large-scale contribution to the severity of a precipitation event. EPEs require extreme water vapour convergence to sustain high intensities for an extended period of time, which is why the association between precipitation and water vapour transport is particularly strong (Lavers et al. 2014). A first comparison of IVTe and IVTn in Table 2 shows that although moisture transport was significant in the 1994 event, it was inferior to the one registered during the Po flood of 11–15 October 2000. Precipitation in the 2000 event was, in fact, more intense, also due to the presence of higher convective instability (higher CAPE, lower DTmin, and higher column-integrated water vapour) associated with a warm air mass (see θ_e at 850 hPa in Table 2).

Aiming at comparing the contribution of the large-scale circulation, we display the distribution of IVTn as a tracer of the intensity of the upper-level wave and the availability of moisture. The distribution of IVTn, averaged over the target domain of northern-central Italy defined in G2020, is shown in Fig. 6 for the different EPE categories. Non-EPE days are shown in black, while Cat1, Cat2, and Cat3 events are coloured according to the legend. In addition, recent significant events are marked by the red bars on the x -axis. We notice that the

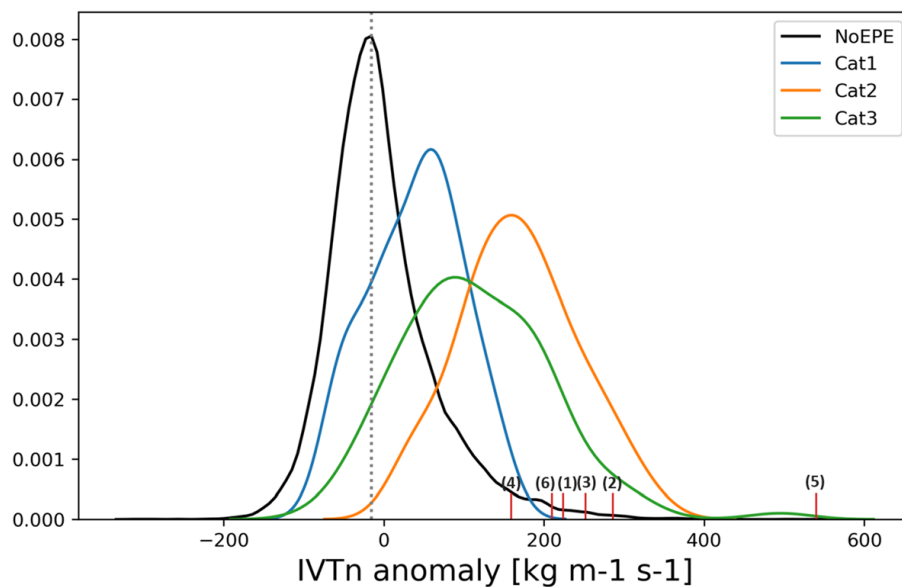


Fig. 6 Distribution of daily IVTn [$\text{kg m}^{-1} \text{s}^{-1}$] averaged over the target domain of Northern-Central Italy for non EPEs days (black curve), Cat1 days (blue curve), Cat2 days (orange curve), and Cat3 days (green curve). Numbers refer to analogue cases of the 1994 Piedmont event in chronological order. Recent cases are also considered not included in the former classification. (1) 5 November 1994, (2) 13 October 2000, (3) 14 October 2014, (4) 21 November 2016, (5) 20 October 2018 storm “Vaia”, and (6) 21 October 2019

IVTn values associated with all the marked events lie around and mostly to the right of the Cat2 distribution mode, which is just slightly below $200 \text{ kg m}^{-1} \text{ s}^{-1}$. All these events produced extensive and damaging floods over the western Po valley and the Piedmont region (see Arpa Piemonte 2019, for an intercomparison and description of these cases). Standing out from the Cat2 IVTn distribution is storm Vaia, one of the strongest ever recorded over Central and Northern Italy (Cavaleri et al. 2019). The Cat2 distribution is clearly separated from the non-EPE days distribution (black curve), so we can empirically assume that IVTn daily mean values beyond $200 \text{ kg m}^{-1} \text{ s}^{-1}$ are very likely for Cat2 events.

6 Discussion and conclusions

In this study, we have revisited the dynamical evolution of the 1994 Piedmont flood event with new reanalysis and high-resolution precipitation datasets and in the light of a recent EPE classification approach. We have shown that this event may be considered an archetype for southern Alpine Cat2 EPEs which are able to produce very high river discharges and widespread flooding on small and large river basins due to the combined presence of stratiform precipitation and deep convection. The main triggering factor was a meridionally elongated upper-level trough, embedded in an incoming Rossby wave packet that originated in the Pacific. The wave packet propagation modulated the transport of a large moisture quantity from the central Atlantic towards the Mediterranean, with a formation of an AR over the central Mediterranean Sea. We also documented the presence of hurricane Florence in the central Atlantic in the days before the events, which interacted with the upstream trough and arguably contributed to strengthen the downstream development of the synoptic wave responsible for the precipitation. Finally, we have highlighted the value of the integrated water vapour transport as a key variable for detecting large-scale conditions favourable to the realization of these events, proposing a threshold based on the meridional component IVTn.

There is a growing interest by forecasters to complement direct model precipitation output (including probability) with other variables/methods which could give a physical insight into the type of precipitation event to be expected. Lavers et al. (2016) pointed out that IVT is very useful to detect extreme events in the medium range or even later, while for the shorter forecast ranges, considering only water vapour fluxes may lead to higher false alarm rate than using precipitation. Therefore, we conclude that the increased predictability of water vapour transport could be used as the basis for a classification method, including other variables, e.g. related to RWP properties, to be applied to real-time forecast fields. This could provide a more robust approach to increase preparedness regarding EPEs, especially at longer forecast ranges. This is becoming even more substantial in view of the increasing likelihood of extreme precipitation events in a warming climate.

Acknowledgements We are grateful to three anonymous reviewers for their suggestions towards improving this study. We would also like to thank George Craig for useful discussions and suggestions on the manuscript.

Funding Open Access funding provided by Projekt DEAL.

Compliance with ethical standards

Competing interests The authors declare that they have no conflict of interest.

Open Access This article is licensed under a Creative Commons Attribution 4.0 International License, which permits use, sharing, adaptation, distribution and reproduction in any medium or format, as long as you give appropriate credit to the original author(s) and the source, provide a link to the Creative Commons licence, and indicate if changes were made. The images or other third party material in this article are included in the article's Creative Commons licence, unless indicated otherwise in a credit line to the material. If material is not included in the article's Creative Commons licence and your intended use is not permitted by statutory regulation or exceeds the permitted use, you will need to obtain permission directly from the copyright holder. To view a copy of this licence, visit <http://creativecommons.org/licenses/by/4.0/>.

References

- Arpa Piemonte 1998, L'evento alluvionale del 2–6 Novembre 1994. In Italian. Last accessed on 10/04/2020. <http://www.arpa.piemonte.it/approfondimenti/temi-ambientali/geologia-e-dissesto/pubblicazioni/immagini-e-files/ev9496/EventialluvionaliinPiemonte1994cap1.pdf>
- Arpa Piemonte 2019, Eventi alluvionali in Piemonte - Evento del 19–24 ottobre 2019, prima parte. In Italian. Last accessed on 10/04/2020. http://www.arpa.piemonte.it/pubblicazioni-2/relazioni-tecniche/analisi-eventi/eventi2019/rapporto-evento-19-24-ottobre_parte1
- Buzzi A, Tartaglione N (1995) Meteorological modelling aspects of the Piedmont 1994 flood. MAP Newsletter 3:27–28
- Buzzi A, Tartaglione N, Malguzzi P (1998) Numerical simulation of the 1994 Piedmont flood: role of orography and moist processes. Mon Weather Rev 126:2369–2383
- Buzzi A, Di Muzio E, Malguzzi P (2020) Barrier winds in the Italian region and effects of moist processes. Bull of Atmos Sci & Technol 1:59–90. <https://doi.org/10.1007/s42865-020-00005-6>
- Cassardo C, Loglisci N, Gandini D, Qian M, Niu G, Ramieri P, Pelosini R, Longhetto A (2002) The flood of November 1994 in Piedmont, Italy: a quantitative analysis and simulation. Hydrol Process 16(6):1275–1299. <https://doi.org/10.1002/hyp.1062>
- Cavaleri L, Bajo M, Barbariol F, Bastianini M, Benetazzo A, Bertotti L, Chiggiato J, Davolio S, Ferrarin C, Magnusson L, Papa A, Pezzutto P, Pomaro A, Umgiesser G (2019) The October 29, 2018 storm in Northern Italy – an exceptional event and its modeling, Progress in oceanography. 178:102178. <https://doi.org/10.1016/j.pcean.2019.102178>
- Ferrero E., G. Balsamo (2020), The 1994 Piedmont flood revisited. ECMWF Newsletter 162, Winter 2020, pag. 8–9
- Ferretti R, Low-Nam S, Rotunno R (2000) Numerical simulations of the 1994 Piedmont flood of 4–6 November. Tellus 52A:162–180
- Fragkoulidis G, Wirth V, Bossmann P, Fink AH (2018) Linking northern hemisphere temperature extremes to Rossby wave packets. Q J R Meteorol Soc 144(711):553–566. <https://doi.org/10.1002/qj.3228>
- Froidevaux P, Martius O (2016) Exceptional integrated vapour transport toward orography: an important precursor to severe floods in Switzerland. Q.J.R. Meteorol. Soc. 142:1997–2012. <https://doi.org/10.1002/qj.2793>
- Grams C, Archambault H (2016) The key role of diabatic outflow in amplifying the midlatitude flow: a representative case study of weather systems surrounding western North Pacific extratropical transition. Mon Weather Rev 144(10):3847–3869. <https://doi.org/10.1175/MWR-D-15-0419.1>
- Grazzini F (2007) Predictability of a large-scale flow conducive to extreme precipitation over the western Alps. Meteorog Atmos Phys 95(3–4):123–138. <https://doi.org/10.1007/s00703-006-0205-8>
- Grazzini F, Vitart F (2015) Atmospheric predictability and Rossby wave packets. Q.J.R. Meteorol Soc 141: 2793–2802. <https://doi.org/10.1002/qj.2564>
- Grazzini F, Craig G, Keil C, Antolini G, Pavan V (2020a) Extreme precipitation events over Northern Italy. Part I: A systematic classification with machine-learning techniques Quarterly Journal of the Royal Meteorological Society 146:69–85. <https://doi.org/10.1002/qj.3635>
- Grazzini, F., Fragkoulidis, G., Teubler, F., Wirth, V., Craig G. C. (2020b): Extreme precipitation events over Northern-Central Italy. Part II: Dynamical precursors and decadal variability. *Submitted to QJRM*
- Hersbach, H., B. Bell, P. Berrisford, S. Hirahara, A. Horanyi, J. Muñoz-Sabater, J. Nicolas, C. Peubey, R. Radu, D. Schepers, A. Simmons, C. Soci, S. Abdalla, X. Abellan, G. Balsamo, P. Bechtold, G. Biavati, J. Bidlot, M. Bonavita, G. Chiara, P. Dahlgren, D. Dee, M. Diamantakis, R. Dragani, J. Flemming, R. Forbes, M. Fuentes, A. Geer, L. Haimberger, S. Healy, R. J. Hogan, E. Holm, M. Janiskova, S. Keeley, P. Laloyaux, P. Lopez, C. Lupu, G. Radnoti, P. Rosnay, I. Rozum, F. Vamborg, S. Villaume, and J. Thepaut, 2020: The ERA5 global reanalysis. Quarterly Journal of the Royal Meteorological Society, qj.3803, URL <https://doi.org/10.1002/qj.3803>

- Krichak SO, Barkan J, Breitgand JS, Gualdi S, Feldstein SB (2015) The role of the export of tropical moisture into midlatitudes for extreme precipitation events in the Mediterranean region. *Theor Appl Climatol* 121: 499–515. <https://doi.org/10.1007/s00704-014-1244-6>
- Lavers DA, Villarini G (2013) The nexus between atmospheric rivers and extreme precipitation across Europe. *Geophys Res Lett* 40:3259–3264. <https://doi.org/10.1002/grl.50636>
- Lavers DA, Pappenberger F, Zsoter E (2014) Extending medium-range predictability of extreme hydrological events in Europe. *Nat Commun* 5:5382
- Lavers DA, Waliser DE, Ralph FM, Dettinger MD (2016) Predictability of horizontal water vapor transport relative to precipitation: enhancing situational awareness for forecasting western U.S. extreme precipitation and flooding. *Geophys Res Lett* 43:2275–2282. <https://doi.org/10.1002/2016GL067765>
- Martius O, Schwierz C, Davies HC (2008) Far-upstream precursors of heavy precipitation events on the Alpine south-side. *Q J R Meteorol Soc* 134(631):417–428. <https://doi.org/10.1002/qj.229>
- Owens, R G, Hewson, T D (2018): ECMWF Forecast User Guide. Reading: ECMWF. <https://doi.org/10.21957/m1cs7h>
- Pavan V, Antolini G, Barbiero R, Berni N, Brunier F, Cacciamani C, Cagnati A, Cazzuli O, Cicogna A, de Luigi C, di Carlo E, Francioni M, Maraldo L, Marigo G, Micheletti S, Onorato L, Panettieri E, Pellegrini U, Pelosini R, Piccinini D, Ratto S, Ronchi C, Rusca L, Sofia S, Stelluti M, Tomozeiu R, Torrigiani Malaspina T (2019) High resolution climate precipitation analysis for North-Central Italy, 1961–2015. *Clim Dyn* 52(5–6):3435–3453. <https://doi.org/10.1007/s00382-018-4337-6>
- Pohorsky R, Röthlisberger M, Grams C, Riboldi J, Martius O (2019) The climatological impact of recurving north Atlantic tropical cyclones on downstream extreme precipitation events. *Mon Weather Rev* 147(5): 1513–1532. <https://doi.org/10.1175/MWR-D-18-0195.1>
- Ralph FM, Dettinger MD (2011) Storms, floods, and the science of atmospheric rivers, EOS, transactions. *Am Geophys Union* 92(32):265–272

3.3 EPE Large-scale drivers and dynamical precursors (Part II)

RESEARCH ARTICLE

Extreme precipitation events over northern Italy. Part II: Dynamical precursors

Federico Grazzini^{1,2}  | Georgios Fragkoulidis³ | Franziska Teubler³ | Volkmar Wirth³ | George C. Craig¹

¹Ludwig-Maximilians-Universität, Meteorologisches Institut, Munich, Germany

²ARPAE-SIMC, Regione Emilia-Romagna, Bologna, Italy

³Institute for Atmospheric Physics, Johannes Gutenberg University Mainz, Mainz, Germany

Correspondence

Federico Grazzini,
Ludwig-Maximilians-Universität,
Meteorologisches Institut,
Theresienstrasse 37, 80333 München,
Germany.
Email: federico.grazzini@lmu.de

Funding information

Ludwig-Maximilians-Universität München; German Research Foundation (DFG), Grant/Award Number: FR 4363/1-1; Transregional Collaborative Research Centre

Abstract

The connection between weather extremes and Rossby wave packets (RWP) has been increasingly documented in recent years. RWP propagation and characteristics can modulate the midlatitude weather, setting the scene for temperature and precipitation extremes and controlling the geographical area affected. Several studies on extreme precipitation events (EPEs) in the Alpine area reported, as the main triggering factor, a meridionally elongated upper-level trough as part of an incoming Rossby wave packet. In this work, we investigate a wide number of EPEs occurring between 1979 and 2015 in northern-central Italy. The EPEs are subdivided into three categories (Cat1, Cat2, Cat3) according to thermodynamic conditions over the affected region. It is found that the three categories differ not only in terms of the local meteorological conditions, but also in terms of the evolution and properties of precursor RWPs. These differences cannot be solely explained by the apparent seasonality of the flow; therefore, the relevant physical processes in the RWP propagation of each case are further investigated. In particular, we show that RWPs associated with the strongest EPEs, namely the ones falling in Cat2, undergo a substantial amplification over the western North Atlantic due to anomalous ridge-building 2 days before the event; arguably due to diabatic heating sources. This type of development induces a downstream trough which is highly effective in focusing water vapour transport toward the main orographic barriers of northern-central Italy and favouring the occurrence of EPEs.

KEYWORDS

atmospheric rivers, extreme precipitation, integrated water vapour transport, large-scale forcing, potential vorticity, Rossby wave packets

1 | INTRODUCTION

Extreme precipitation events (EPEs) in the south-Alpine area are often followed by destructive flooding with severe

socio-economic impacts. This constitutes a recurring threat for the exposed population, and research efforts need to focus on a better understanding of the physical processes leading to such events. Moreover, positive trends in

This is an open access article under the terms of the Creative Commons Attribution License, which permits use, distribution and reproduction in any medium, provided the original work is properly cited.

© 2020 The Authors. *Quarterly Journal of the Royal Meteorological Society* published by John Wiley & Sons Ltd on behalf of the Royal Meteorological Society.

extreme precipitation in this area emerge, particularly in autumn (Isotta *et al.*, 2014; Brönnimann *et al.*, 2018; Pavan *et al.*, 2019), and EPE-related fatalities increase, specifically in the subalpine regions of southern France and Italy (Petrucci *et al.*, 2019).

Many studies have investigated the dynamics of such individual events, while fewer tried to find an association between the evolution of large-scale dynamical features and EPEs on the Alpine area based on a large sample of dates (say >100 cases, see for example Martius *et al.*, 2006a; Grazzini, 2007; Pinto *et al.*, 2013; Pohorsky *et al.*, 2019). Nevertheless, the linkage between extreme precipitation in the Alpine area and the presence of a large-amplitude wave or potential vorticity (PV) streamer over western Europe is well established. For example, Martius *et al.* (2008) have indicated that 73% of days with extreme precipitation over the Swiss Alps are associated with a PV streamer.

The connection between extreme weather events and Rossby wave packets (RWPs) has been documented by many studies that examined the physical linkage between the upper-tropospheric circulation and anomalous weather at the surface. In particular, these events are often associated with pronounced undulations in the upper-tropospheric jet that typically take the form of an eastward-propagating RWP. A comprehensive list of studies investigating the role of RWPs for a variety of meteorological extremes can be found in section 7 of the recent review by Wirth *et al.* (2018). Previous studies have also suggested that EPEs are modulated by large-scale waviness associated with eastward-propagating wave packets. High RWP amplitudes over the North Atlantic and Europe imply that a succession of high-amplitude troughs and ridges may be associated with heat and moisture fluxes that create favourable conditions for the occurrence of EPEs (Piaget *et al.*, 2015; Liu *et al.*, 2020). In addition, Boers *et al.* (2019) have recently suggested that EPEs occurring at distant places (>2,500 km) are not entirely independent, since they are typically associated with the same Rossby wave packet.

Based on the above, a better understanding of the dynamical linkage between RWPs and EPEs is extremely important in evaluating, among other things, the variability of these events at climate time-scales and their predictability at weather time-scales. However, the evolution of individual RWPs may differ in several aspects, including the processes that dominate their evolution and the kind of wave breaking at their leading edge, which can eventually determine the precipitation amount and impact. Moore *et al.* (2019) point out that different types of wave breaking produce different responses in the intensity and area extension of EPEs over the USA. More relevant for the present study, they also note that cyclonic wave breaking over the eastern USA produces stronger ridge

amplification downstream, over the Atlantic, due to strong PV gradient tilting and strong ascent.

Apart from the presence of a large-scale dynamical forcing factor, Sodemann and Zubler (2010) showed that moisture sources for EPEs in the Alpine area can be distant and pointed to the fact that moisture uptake in the Mediterranean is not the only source. They also highlighted the case-to-case variability in this respect. Very often large amounts of moisture come from different sectors of the Atlantic basin, with a different partition for each precipitation type, that is, stratiform or deeply convective (Winschall *et al.*, 2014). Therefore, it is important to appropriately consider the variability in dynamical forcing and moisture transport between the events in order to identify the driving factors.

According to Pohorsky *et al.* (2019), strong ridge amplification over the Atlantic appears to be a necessary prerequisite for EPEs over Europe. They show that ridge building could be further enhanced by strong diabatic heating disturbances, like those induced by recurving tropical cyclones (TCs) or associated with strong warm conveyor belts (WCBs). They recognized two main evolution patterns: in the first one, which they call “atmospheric river-like”, the building of the Atlantic ridge occurs more in the zonal direction and there is a direct transport of water vapour from west to east Atlantic along the northern side of the ridge. In the second one, called the “downstream development” pathway, the water vapour flux is more meridional, associated with a greater meridional amplification of the Atlantic ridge and downstream trough. The water vapour fluxes over Europe are coming more from the southerly direction and from the northerly flow on the back of the trough. Large-scale dynamics evolution thus influences atmospheric river landfall location and subsequent precipitation extremes in Europe (Pasquier *et al.*, 2019).

The above considerations suggest that large-scale dynamical features influence the frequency and intensity of EPEs and a deeper investigation of their dynamical pathways will be essential in improving our understanding of such events. Based on the EPE categorization presented in Part I of this study (Grazzini *et al.*, 2020a), we will address the question of whether EPEs of different categories are associated with distinct large-scale dynamical evolutions.

The article is organized as follows. In Section 2, we describe the data used and the methods employed in this study. In Section 3, we present the main characteristics and synoptic conditions of the three EPE categories and examine their linkage to upper-tropospheric waviness. In Section 4, we investigate the spatio-temporal evolution of the upper-tropospheric flow and associated moisture transport prior to the EPEs and examine the dynamical processes involved based on a PV tendency framework.

Finally, the conclusions of the study are presented in Section 5.

2 | DATA AND METHODS

The atmospheric fields used in this study are retrieved from the ERA5 reanalysis (Hersbach *et al.*, 2020) over the period 1979–2015, while precipitation data, upon which the EPE definition is based, are retrieved from the gridded dataset (5×5 km) of the Archivio Climatologico per l'Italia centro-Settentrionale (climatological archive for central-northern Italy, ArCIS) archive (Pavan *et al.*, 2019). With the exception of the analysis in Section 4.4 (see Section 2.4), deviations from climatology (i.e. anomalies) are computed following Fragkoulidis *et al.* (2018). In particular, the mean annual cycle at a given grid point is smoothed by a Fourier decomposition and restriction to the first four harmonics. A separate smooth annual cycle is produced for the four available times of the day (i.e. 0000, 0600, 1200, 1800 UTC) so that the diurnal cycle is taken into account. The anomalies are then computed by subtracting the respective smoothed annual cycle from the 6-hourly full field.

2.1 | EPE definition and classification

The selection of EPEs, which will form the basis for our investigations, follows the methodology that has been described in Part I (Grazzini *et al.*, 2020a). Precipitation measurements in a dense network of 1,762 rain-gauges are first aggregated over the 94 warning areas (WAs) of the Italian Department of Civil Protection (Figure 1). This choice is preferable to regular boxes, since precipitation averages are computed on subregional hydrological basins which are climatologically homogenous. EPEs are then defined as days with daily precipitation greater than or equal to the 99th percentile across one or more WAs, occurring in the period 1979–2015. As in Part I, EPEs are subdivided into three categories based on an unsupervised K-means clustering approach that considers area-averaged values of six thermodynamic and dynamical fields (convective adjustment time-scale τ_{conv} , convective available potential energy CAPE, meridional component of integrated water vapour transport IVT_n , θ_{e850} , $\Delta\theta_{e500-850}$, total column water vapour TCWV) described in table 1 of Part I. In contrast to Part I, which is based on ERA-Interim data (Dee *et al.*, 2011), the subdivision of EPEs here is actualized on the new ERA5 dataset. The catalogue of EPE days is very similar to the one of Part I, since the classification is based on area-averaged values and it is not sensitive to small local changes. Next, we compose the lists of independent

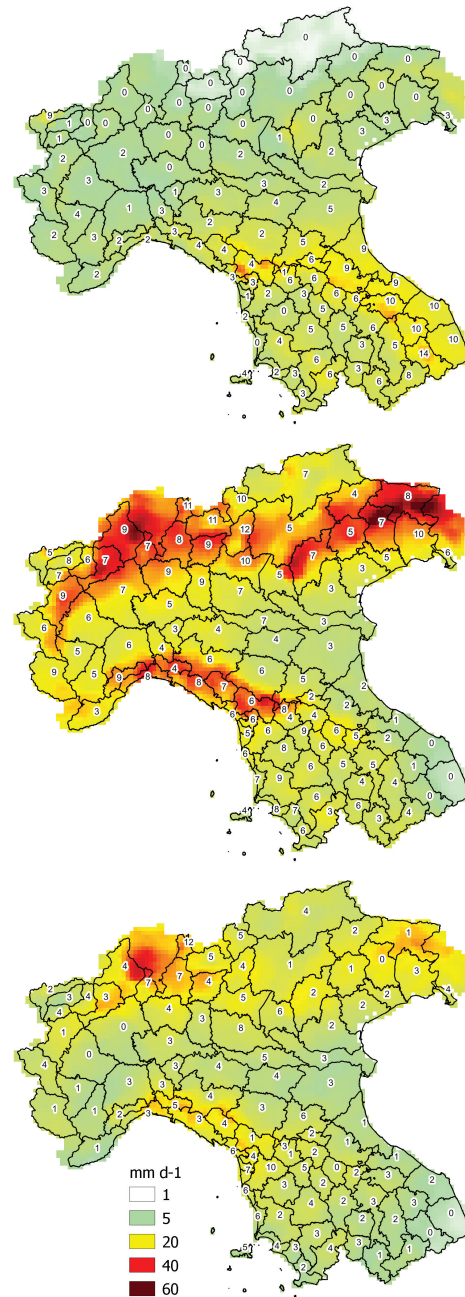


FIGURE 1 Precipitation composites [$\text{mm} \cdot (24 \text{ hr})^{-1}$] during the 100 representative Cat1 (top), Cat2 (middle), and Cat3 (bottom) EPEs. Warning area boundaries are shown along with the number of exceedances of the 99th of daily precipitation in each warning area

events in each category. For episodes that lasted for more than one consecutive day, we identify the first day of this sequence as the onset of the extreme precipitation event. The next event has to be at least 3 days later. This way, the EPEs we investigate can be considered as distinct events. Given that the resulting lists of independent events in the three EPE categories are not equal in size (287, 248

and 133 events in category 1, 2 and 3, respectively), for the purpose of comparison, a subsample of the 100 most representative cases of each category is selected based on ranking of the Silhouette score (SIL: Rousseeuw, 1987). SIL measures, along each dimension (i.e. each normalized predictor), how tightly the events are grouped inside each cluster (cohesion) compared to the remaining clusters (separation). It ranges from -1 (wrong clustering) to 1 (fully separated and compact clusters) with values equal to 0 indicating that a given element has the same distance from the other cluster centroids (overlapping). Consequently, the 100 cases of each category with the highest SIL score are the cases that are most separated from the other categories and best characterize their cluster.

2.2 | Diagnosis of Rossby wave packet amplitude

The diagnosis of RWP amplitude follows the approach of Zimin *et al.* (2003), with a few distinctions in the input variable and filtering steps. First, the 300 hPa meridional wind anomaly at every latitude is zonally filtered to wavelengths 2,000–10,000 km using a Tukey window in spectral space as in Fragkoulidis *et al.* (2018). Using the anomaly field excludes the effect of stationary waves from the analysis and the zonal filtering restricts to the more relevant scales of a transient RWP evolution, that is, the typically small contribution from transient planetary waves and small-scale features is effectively discarded. Subsequently, a meridional convolution with a Hann window (Harris, 1978) of 7° length at half maximum is applied in order to account for possible unphysical discontinuities from the latitude-wise application of the zonal filtering. Discarding the negative frequencies and applying an inverse Fourier transform to the meridional wind signal at every latitude results in a complex representation of this signal. The modulus of this so-called “analytic signal” corresponds to the envelope, E , of meridional wind, that is, the RWP amplitude. Finally, a weak smoothing is applied to the E field by discarding zonal wavelengths below 4,000 km (see also Fragkoulidis and Wirth, 2020).

2.3 | Statistical significance assessment

Statistical significance in the composite maps and Hovmöller diagrams is assessed using a Monte Carlo approach (e.g. Martius *et al.*, 2008). In particular, the value at a grid point is statistically significant at the $\alpha = 0.10$ level, if it belongs to the highest or lowest 5% tail of a distribution created by reconstructing the composite 300 times using

random selections of an equal number of dates. The assessment of statistical significance in a given field takes the seasonality of EPEs into account by properly restricting the pool the random dates are selected from. In particular, this pool includes the months when more than 10 EPEs of a given category have occurred (Figure 3). For Cat1 EPE composites we draw dates from November, December, January, February, March and April. For Cat2 EPE composites, we draw dates from May, June, September, October and November. Finally, for Cat3 EPE composites, we draw dates from June, July, August and September.

2.4 | PV tendency framework

We investigate the spatio-temporal evolution of the upper-tropospheric flow preceding EPEs by analysing the PV tendencies, as introduced by Teubler and Riemer (2016). This framework was previously applied, among other studies, to investigate the amplification of a North Atlantic ridge–trough couplet, associated with a severe precipitation event on the northern side of the Alps (Piaget *et al.*, 2015).

The framework is based on the hydrostatic form of Ertel’s potential vorticity PV on an isentropic surface. Anomalies in PV, PV' , are calculated (in contrast to Teubler and Riemer, 2016) as deviations from a background \overline{PV} , similar to the one described at the beginning of Section 2. Only for smoothing, a 30-day running mean is used instead of Fourier decomposition. Following the concept of baroclinically coupled Rossby waves (Eady, 1949; Hoskins *et al.*, 1985) the PV anomalies are separated into upper-level and low-level PV anomalies. The associated wind field perturbation is derived by piecewise PV inversion under nonlinear balance (Charney, 1955; Davis, 1992). From that we calculate PV tendencies due to the advection of the PV background by (a) the upper-level wind field perturbation, which physically represents downstream development and by (b) the low-level wind field perturbation, which represents baroclinic interaction. We add the (negligible) advection term by the background flow to (a) and refer to this, in the following, as quasi-barotropic propagation. Additionally we derive the divergent flow by Helmholtz-partitioning. Similar to the advective tendencies from piecewise PV inversion we calculate the advection of the PV background by the divergent flow and additionally the PV tendency accounting for an area change of the anomalies due to divergent flow (compare tendencies from equation 6 in Teubler and Riemer (2020)). In the following, a vertical average of the PV tendencies between 315 and 350 K (every 5 K) is considered to account for the seasonal cycle. A more detailed description of the PV tendency

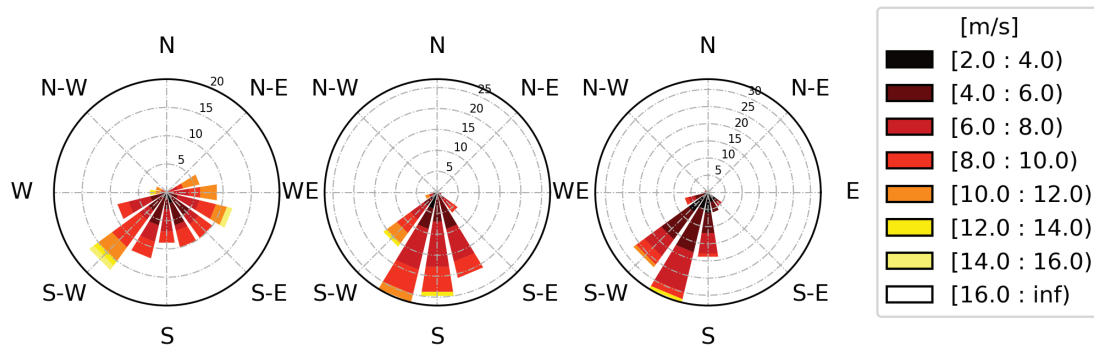


FIGURE 2 Direction and intensity of 850 hPa wind associated with the 100 representative Cat1 (left), Cat2 (middle) and Cat3 (right) EPEs. Spokes indicate the distribution of prevailing wind direction during the EPEs, with their length pointing to the greatest frequency (frequency is shown on the radial contours every 5%). Colour bands are showing mean wind speed in each direction ($[m \cdot s^{-1}]$, see legend). Wind direction and speed are computed as the daily average over the target area which includes the whole of north and central Italy

framework and a comparison to the more commonly used eddy kinetic energy framework can be found in Wirth *et al.* (2018).

3 | EPE CHARACTERISTICS AND UPPER-TROPOSPHERIC WAVINESS

In this section, we discuss the synoptic conditions and monthly distribution associated with the three EPE categories. Furthermore, we examine the linkage between extreme precipitation over northern-central Italy and upper-tropospheric waviness.

3.1 | Precipitation distribution and synoptic analysis

In Figure 1, we show the precipitation composites for the 100 representative cases of each EPE category. The precipitation patterns in the three categories appear consistent with the expected subdivisions and the associated meteorological conditions which are briefly recalled here. Category 1 (Cat1) events originate from frontal structures, with slantwise ascent in warm sectors and warm conveyor belts of Mediterranean cyclones. The associated mechanical orographic uplift of low-level marine, statically stable air typically produces extreme precipitation mostly confined to upwind steep topography. The distinctive feature of Category 2 (Cat2) events is a synergetic combination of frontal uplift and embedded deep convection which produces the most intense and spatially extended EPEs (as shown in Part I by the mean area extension which is double compared to Cat1 events). They are characterized by a stronger southerly flow component and a reduced moist static stability (almost neutral conditions).

Category 3 (Cat3) events are typically not associated with fronts, and precipitation is due to weakly-forced convection (non-equilibrium convective events) in a potentially unstable thermodynamic environment (i.e. with very high CAPE). To facilitate the interpretation of the composites, the number of the 99th percentile threshold exceedances in each warning area is also shown. Since an EPE is defined as a day in which one or more WAs exceed the 99th percentile threshold of daily rain accumulation, those numbers indicate which areas contributed most in the EPEs selection. As can be seen for example in the Cat1 case, most of the EPEs are associated with extreme rainfall amounts in central Italy and specifically in the Adriatic WAs, presumably due to the easterly low-level winds. Regarding Cat2 events, the situation is different with a higher frequency of extreme rainfall found in Tuscany and south-facing regions on the Apennines and the Alps. The precipitation composite (Figure 1, middle panel), shows higher intensities over the southern part of the Alpine region and the Apennines. Cat2 events are known to produce the stronger impact in terms of floods and damages (see Part I and Grazzini *et al.* (2020b)). For Cat3, the exceedance frequency is rather homogeneous with relative maxima over the central Alps and northern Apennines. The mean direction and intensity of the 850 hPa wind are shown in Figure 2 in the form of wind roses. The low-level wind associated with Cat1 (left panel) shows an almost even distribution of prevailing direction spanning the two southern quadrants, from easterly to westerly direction, with frequency and intensity maxima in the southwest direction. However, easterly winds seem to be as frequent as westerly winds, which can explain the high frequency exceedance of the precipitation threshold in the Adriatic regions. As shown in Figure 3d, Cat1 events typically occur during the colder months (November to April). Precipitation and wind distribution in this category are in fact

in agreement with typical winter surface cyclone development in the area with minima moving east, from the Tyrrhenian sea toward the Adriatic sea, preceded by south-westerly winds and followed by easterly winds.

In contrast, Cat2 events occur mostly in May, June and autumn, and a predominant southerly direction is clearly visible in the middle panel of Figure 2. Cat3 events are concentrated in the period from June to September with a prevailing southwesterly direction. Cat2 and Cat3 events are characterized by a neutrally stable or unstable environment (see Part I, figure 8), respectively, so the flow is less confined at low levels.

Composites of Z at 500 hPa (Figure 3(a–c)), show that a trough over western Europe is present in all three categories. However, the trough in Cat2 events is sharper and more to the west (centred at the prime meridian) than Cat1. The associated surface cyclone over the central Mediterranean in Cat2 is weaker than Cat1, but shifted more to the east relative to the trough axis, pointing therefore to a stronger baroclinicity. A pronounced anomaly of integrated water vapour transport toward the target domain (northern-central Italy) is evident in all three categories, but more pronounced in Cat2. The IVT magnitude is mostly associated with its meridional component, IVT_n , which is much higher than normal, especially in Cat2 where it exceeds the mean values for non-EPE days by more than two standard deviations (not shown). The presence of such IVT anomalies at the synoptic scale points to the pivotal role of upper-level wave amplitude in achieving the strong meridional moisture transport observed. High moisture convergence is a necessary requirement to achieve intense and widespread precipitation (as in Cat2) since the area extension is critically dependent on large-scale convergence of moisture (Loriaux *et al.*, 2017).

3.2 | Linkage between EPE occurrence and RWPs

In this section we aim to quantify the linkage between EPEs in northern-central Italy and RWPs by first assessing the association of heavy precipitation probability with waviness in the upper-tropospheric flow. In this regard, we use two upper-tropospheric waviness indicators: (a) the envelope, E , of meridional wind at 300 hPa, and (b) the absolute value of PV anomaly, $|PV'|$, at 330 K. The first one constitutes a phase-independent measure of the meridional wind amplitude, while the second is a measure of waviness in the upper-troposphere as reflected in the deviations of the PV field from climatology.

In order to introduce the concept of the aforementioned indicators and the statistical analysis that follows,

in Figure 4 we show the dynamical evolution leading to the Piedmont flood of November 1994, a typical example of Cat2 events, described in detail in Grazzini *et al.* (2020b). Depicted are the meridional wind at 300 hPa, the corresponding E , and the 2PVU (PV units) contour at 330 K on the days leading to the event. The evolution of E highlights the regions where the RWP amplitude is large, which is also reflected in the large meridional wind anomaly (v') values and the associated succession of troughs and ridges that result in a wavy 4PVU contour. Days D-4 and D-3 are characterized by isolated and incoherent disturbances over the North Pacific and a weaker disturbance over North America that slowly propagates eastward and appears to strengthen. On D-2, an apparent rapid intensification of the latter results in the formation of a large-amplitude wave packet over the North Atlantic, the leading edge of which is already approaching the British Isles. Meanwhile, the North Pacific disturbances appear to form a more coherent wave packet that reaches North America but does not directly affect the centre of action of the North Atlantic. On D-1, the North Atlantic wave packet has progressed further downstream and is characterized by a strong trough that dominates the flow over western Europe. From D-1 to D0 (onset of the EPE), this trough elongates further, appears to remain quasi-stationary, and obtains a north–south orientation while the leading edge of the wave packet approaches Siberia. As will be discussed later, such a PV streamer structure modulates effectively the regional flow and moisture transport and can thus play an important role in determining the onset and intensity of the EPE. Finally, an apparent wave breaking between D0 and D+1 over western Europe is clearly depicted in the 4PVU contour and marks the decay of the wave packet.

The statistical analysis that follows takes into account that the envelope, E , of meridional wind at 300 hPa is well-suited for RWPs in their almost-plane stage (Fragkoulidis and Wirth, 2020), whereas PV anomaly constitutes a better indicator of upper-level forcing in the later stages of wave overturning and breaking (see also Ghinassi *et al.*, 2018). Therefore, in order to assess the relation between upper-tropospheric waviness and EPE occurrence, we perform two separate regression analyses that involve E on D-2 and $|PV'|$ on D0 averaged over two different areas as shown in Figure 5. The absolute value of PV anomalies is used in order to avoid cancellations between positive and negative anomalies in the area-averaging. The two analyses will involve the daily aggregated precipitation in northern-central Italy as well as the EPE occurrence of a specific category.

For each day in the 1979–2015 period, the daily-mean E is averaged over the 38° – 62° N, 22° W– 2° E area (dashed rectangle in Figure 5) and the resulting sample is split into 10 equally-sized bins based on the nine deciles of

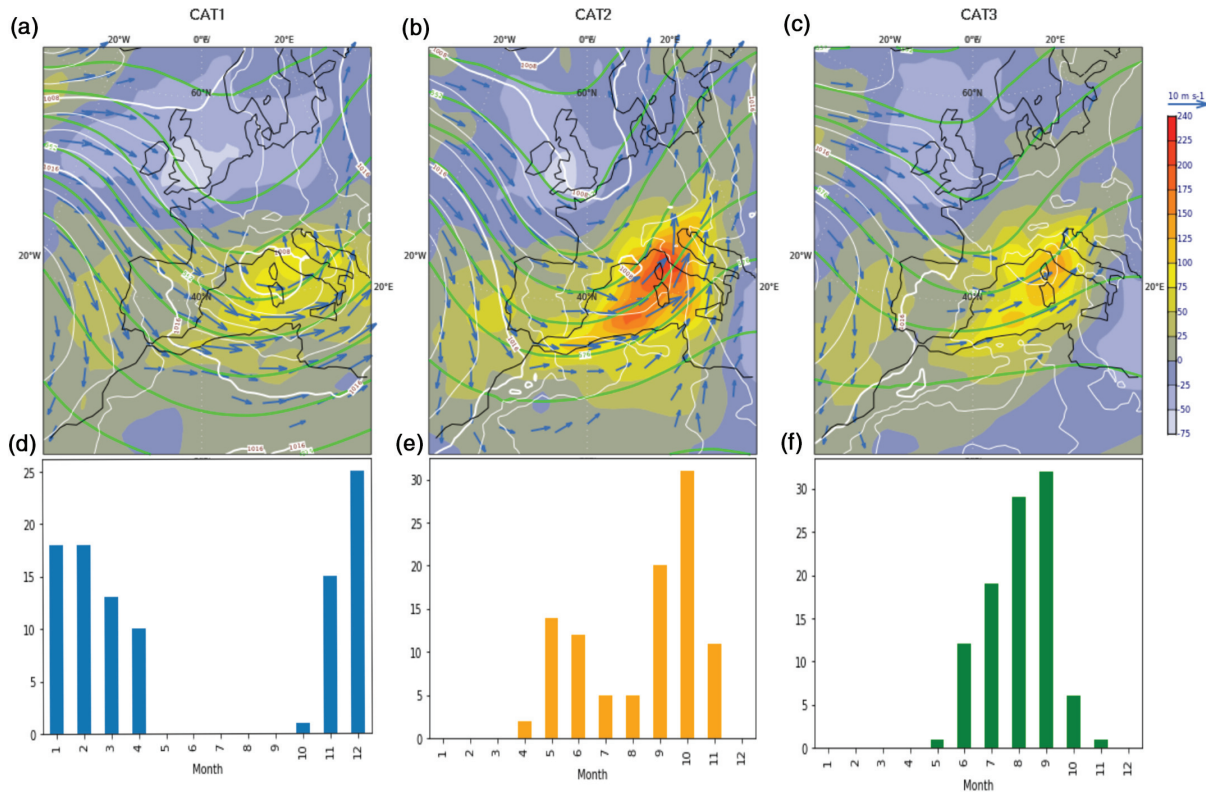


FIGURE 3 Composite maps during the 100 representative (a) Cat1, (b) Cat2 and (c) Cat3 EPEs of geopotential height at 500 hPa (green solid contours, every 6 gpdam), mean-sea-level pressure (white solid contours, every 2 hPa), integrated water vapour transport (IVT) anomaly (colour fill, kg m⁻¹ s⁻¹), and wind speed at 850 hPa (blue arrows, m s⁻¹). (d–f) Monthly distributions of the three EPE categories (number of occurrences)

area-averaged E. The first bin contains the days when E is between the minimum and the 10th percentile, the second bin contains the days with E between the 10th and the 20th percentile, etc. Subsequently, the total precipitation, with a lag of +2 days, is averaged over the 94 available warning areas in northern-central Italy. Figure 6a shows in black dots the percentage of days in each E-bin that surpass the 90th percentile of average precipitation over northern-central Italy, or else, the probability for heavy precipitation over the domain. Note that this is different from EPEs which are defined as days with local extremes on warning areas. The heavy precipitation frequency increases with increasing E and approximately 40% of heavy precipitation events occur at the upper two E-bins. In the same way, the probability for heavy precipitation is evaluated against the contemporary $|PV'|$ at 330 K averaged over the 38°–50°N, 4°–16°E area (solid rectangle in Figure 5) and displayed in Figure 6b. A clear connection is also found in this case with approximately 36% of heavy precipitation events occurring at the upper two $|PV'|$ -bins. Repeating the analysis in this area for E instead of $|PV'|$ results in a worse connection, with only

about 25% of heavy precipitation events at the upper two E-bins (not shown). The fact that the connection between E and northern-central Italy heavy precipitation is better for the dashed rectangle on Day –2 than the solid rectangle in Day 0, suggests that heavy precipitation events in northern-central Italy are typically associated with an upstream RWP that amplifies over the North Atlantic and subsequently breaks over western Europe, as illustrated in the Piedmont flood case.

Next, it is worth investigating whether this relation holds for all three types of EPEs. The blue, orange and green dots in Figure 6 correspond to the percentage of days in each E-bin that is associated with a Cat 1, 2 and 3 EPE, respectively. The probability for Cat 1 and 2 EPEs increases with a rate that is only slightly higher for Cat 1 in the case of E and similar in the case of $|PV'|$. Although there is some waviness in the flow during Cat 3 EPEs (Figure 3c), their occurrence is not increasing with E. The poor correlation in this category is consistent with the fact that Cat 3 events are mostly associated with high thermodynamic instability and non-equilibrium convection (or weakly forced convection), in which the interaction between the synoptic

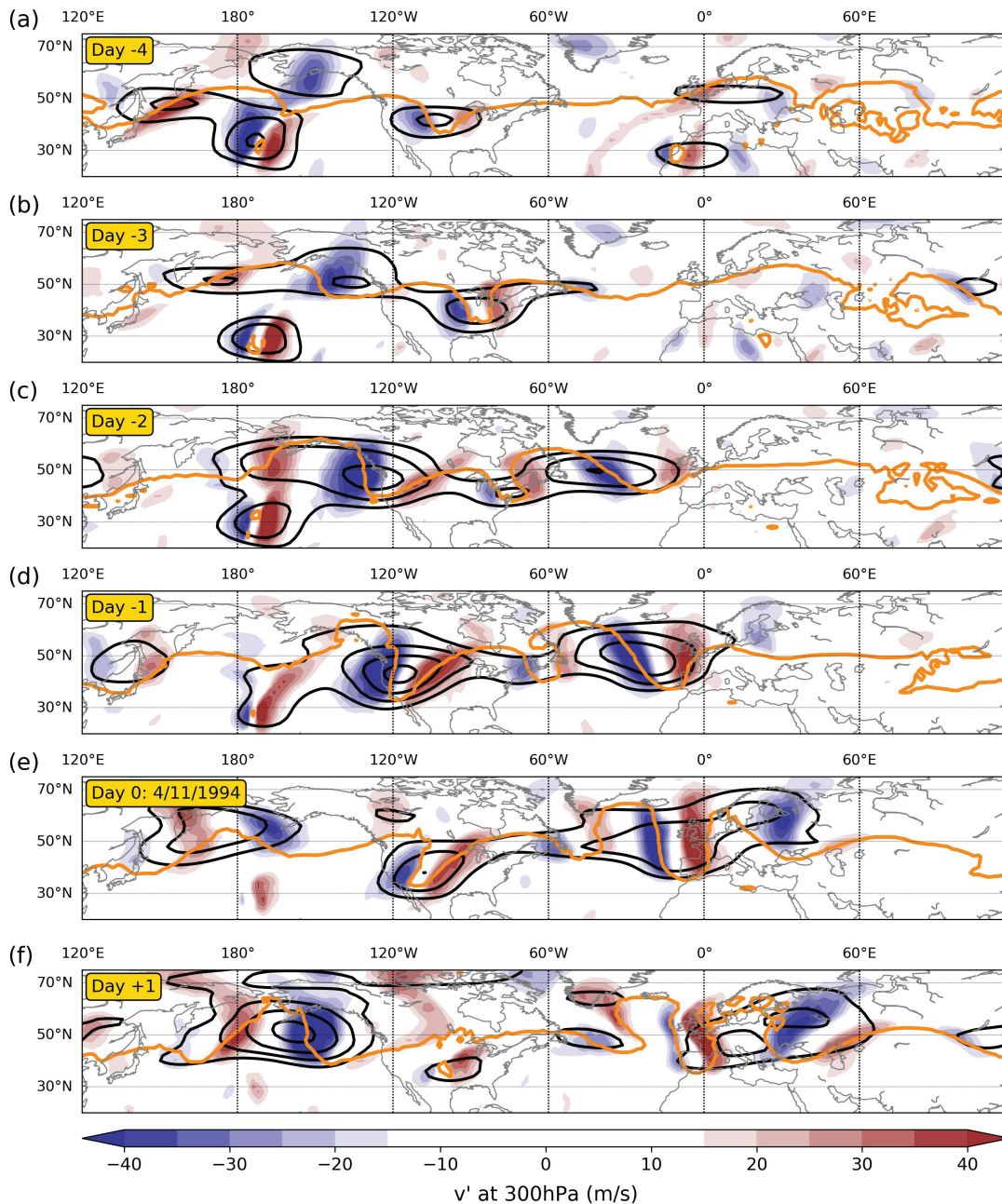


FIGURE 4 Evolution of the upper-tropospheric flow leading to the November 1994 Piedmont flood. The panels depict mean daily values of meridional wind at 300 hPa (colour fill, $\text{m}\cdot\text{s}^{-1}$), E at 300 hPa (black contours every $10 \text{ m}\cdot\text{s}^{-1}$ starting from $25 \text{ m}\cdot\text{s}^{-1}$), and the 4PVU isoline at 330 K (orange contour) at (a) 31 October 1994 (day -4), (b) 1 November 1994 (day -3), (c) 2 November 1994 (day -2), (d) 3 November 1994 (day -1), (e) 4 November 1994 (day 0), and (f) 5 November 1994 (day $+1$)

flow and convection is weaker (Done *et al.*, 2006; Zimmer *et al.*, 2011). The weak relation also suggests that these events are less predictable, since severe convection can be triggered, in a very unstable environment, even with small amplitude waves or due to local thermal circulations. It should be noted that, generally, the probabilities of Cat 1, 2 and 3 EPE occurrence in each E-bin do not sum up to

the heavy precipitation probability (black dots), since the former are defined with stricter criteria (days with at least one warning area with daily precipitation above the 99th percentile). Finally, we notice that the probability of EPEs grows slightly more rapidly with E for mountainous as opposed to low elevation warning areas (not shown). This

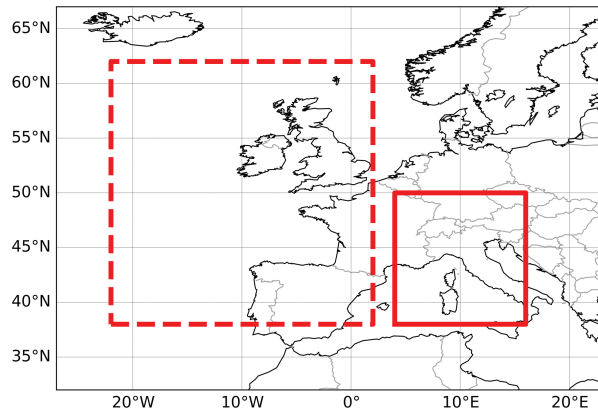


FIGURE 5 Areas used for averaging E at D-2 (dashed rectangle; 38° – 62° N, 22° W– 2° E) and $|PV'|$ at D0 (solid rectangle; 38° – 50° N, 4° – 16° E)

implies that, due to the stronger interaction with orography, the mountainous regions are more sensitive to RWP amplitude.

The above results do not change substantially for slight variations in the size and location of the two areas in Figure 5. Using a single vertical level, as is done here for simplicity, may constitute a limitation in cases when the wave packet evolution is characterized by pronounced variability in the vertical direction. However, the results of the regression analyses in Figure 6 remain quantitatively similar when using the maximum E between the 200, 300 and 400 hPa levels and the maximum $|PV'|$ between the 315 and 350 K levels (with 5 K increment) at every grid point. Finally, it has to be noted that although many times these waviness metrics attain large values over Europe, heavy precipitation or EPEs in northern-central Italy are not observed simply because the phasing of the trough–ridge sequence is not the right one (Figure 3). Therefore, higher probabilities are to be expected when we restrict to cases with a trough over western Europe.

4 | DYNAMICAL EVOLUTION

4.1 | RWP composites

In the previous section, we have shown that there is a statistical relation between large-scale upper-tropospheric waves and the probability of EPEs. In this section, we investigate in more detail the dynamics, and in particular the RWP characteristics leading to the three different categories of EPEs. We want to test the hypothesis that the three different categories exhibit specific propagation patterns of the precursor RWPs. In this respect, Hovmöller diagrams of the upper-tropospheric meridional

wind are well-suited to depict the main properties of the spatio-temporal RWP evolution (Martius *et al.*, 2006b; Persson, 2017). Unlike the amplitude measure used in the previous section, they provide an indication for the preferred phase during the RWP evolution, which is critical for the occurrence of EPEs. To this end, composite Hovmöller diagrams of v' at 300 hPa are constructed for the 100 representative cases of each EPE category (see Section 2.1) and the emerging patterns are shown in Figure 7. Evidently, a large-scale wave feature is recognizable in all categories at Day 0, but the characteristics of the spatio-temporal evolution of the RWPs are different. In the following, T_0 (Trough at Day 0) will refer to the trough over western Europe, directly associated with EPEs (Figure 3), and T_U (Trough Upstream) will refer to the upstream trough forming off the eastern coast of North America.

In Cat1 events, there is a statistically significant far-upstream RWP signal that is first detected over the eastern Pacific 5–6 days before the event and propagates toward Europe at a zonal group velocity of approximately $30^{\circ}\cdot\text{day}^{-1}$ (Figure 7; group velocity can be roughly estimated as the slope of a hypothetical line that connects the areas of positive and negative v' in the Hovmöller diagram). On days -1 to $+1$ of the events, the composite RWP spans approximately 150° in longitude with strong northerlies over the eastern North Atlantic and southerlies over Europe signifying the pronounced trough seen in Figure 3. A few days prior to the emergence of this RWP, a secondary RWP of weaker magnitude and lower group velocity but with the same phase as the primary RWP is also evident in the composite Hovmöller diagram. The two wave packets merge over the target region forming the trough T_0 . This suggests that the amplification and quasi-stationarity of T_0 may sometimes be associated with a sequence of RWPs of the same phasing, that induces a recurrent amplification of troughs and ridges at the same longitudes. The mechanism of RWPs recurrence, as a factor explaining the stationarity and amplification of a particular element of a wave pattern, has been shown by Barton *et al.* (2016) and Röthlisberger *et al.* (2019). Individual troughs and ridges are characterized by high phase speed ($7^{\circ}\cdot\text{day}^{-1}$), extending almost uniformly from the North Pacific to Europe. However, the situation over Europe is characterized by a substantially reduced phase speed (waves slow down, becoming almost stationary) in conjunction with wave amplification and possible wave breaking. Although this sequence of events arises from the analysis of the composite Hovmöller diagram, it appears consistent with the evolution of individual cases.

The composite RWP signal in Cat2 events is more confined in longitude (Figure 7b) compared to Cat1, and

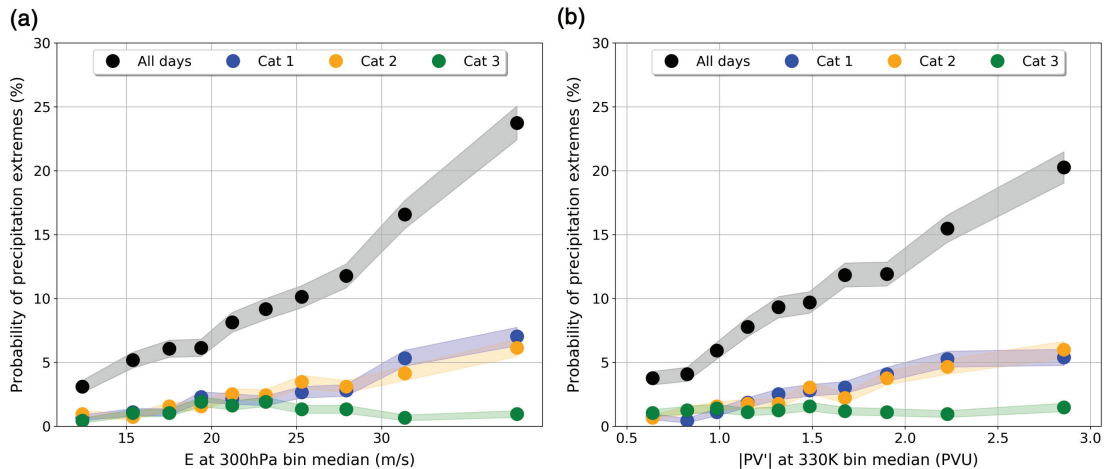


FIGURE 6 (a) Probability of heavy precipitation events in northern-central Italy as a function of the area-averaged E ($\text{m}\cdot\text{s}^{-1}$) (dashed rectangle in Figure 5) at a lag of 2 days. The black dots correspond to the percentage of days next within each E -bin of size N that exceeds the 90th percentile in the average precipitation over the 94 warning areas. The dots in the x -axis are placed at the median of E in each bin. Assuming that next corresponds to the sample mean of a Poisson distribution, and that many measurements have been done resulting in a Poisson distribution of sample means, the associated uncertainty (shaded range) is based on the standard error of this distribution: the blue, orange and green dots correspond to the percentage of days within each E -bin that are characterized as a category 1, 2 and 3 EPE respectively. (b) Same as (a) but now the probability of heavy precipitation events is evaluated against the contemporary area-averaged $|PV'|$ at 330 K (solid rectangle in Figure 5)

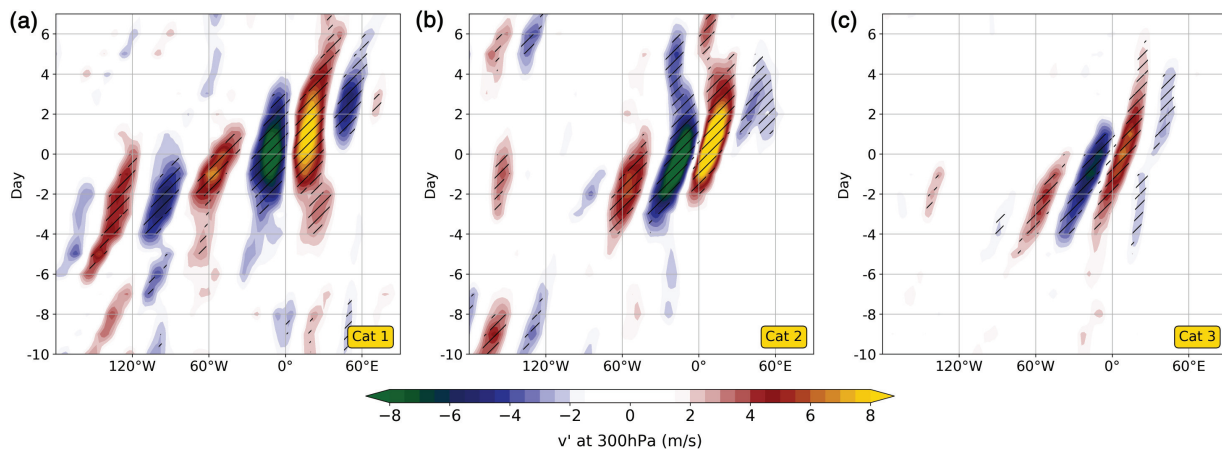


FIGURE 7 Composite Hovmöller plots of v' at 300 hPa (colour fill, $\text{m}\cdot\text{s}^{-1}$; positive meridional wind corresponds to northward direction) during the 100 representative cases of (a) Cat1, (b) Cat2 and (c) Cat3 EPEs. For every longitude, v' is meridionally averaged over the 30° – 60° latitude band. The hatches indicate statistical significance at the 0.10 level (see Section 2.3)

extends from the North American east coast to Europe. This implies that in Cat2 events there is either no in-phase wave propagation west of 90°W (so the signal in the composite is reduced through destructive interference), or there is rapid amplification over the North Atlantic without a significant far-upstream precursor. The amplification starts in T_u just west of 60°W , followed by the development of T_0 around the Greenwich meridian, in the correct phase

to produce strong water vapour convergence and precipitation to the south of the Alps. Therefore, the processes driving the amplification of the North Atlantic ridge may play a key role in determining the evolution and specific positioning of the downstream trough T_0 .

The magnitude of the meridional wind anomaly associated with T_0 and T_U is larger in Cat2 events than the other two categories. Notably, the meridional wind anomaly coupled over Europe is not stationary as in Cat1 events but

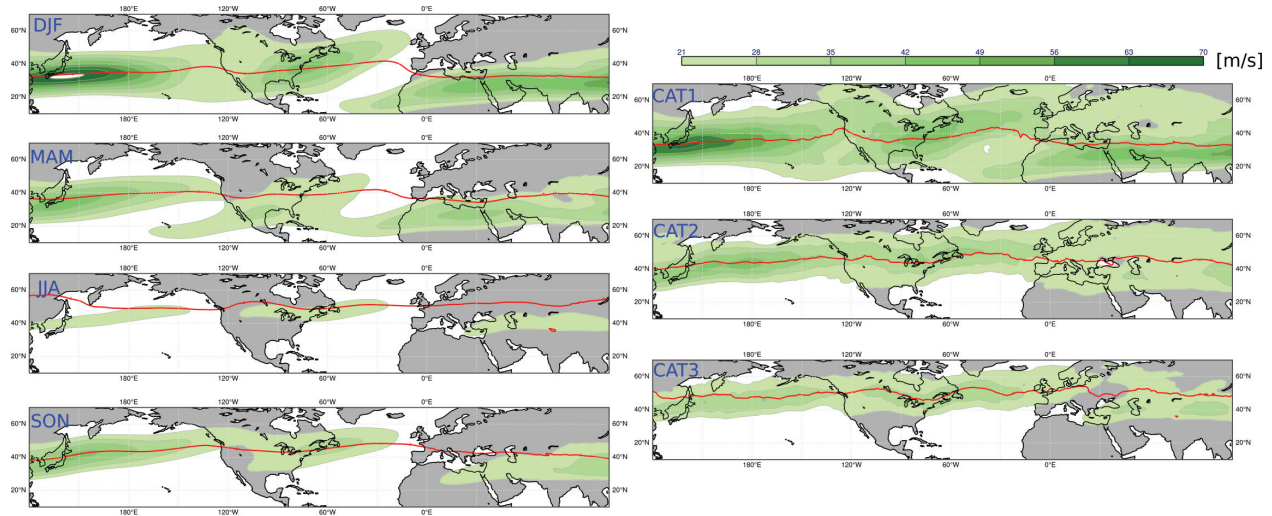


FIGURE 8 Composites of wind speed ($\text{m}\cdot\text{s}^{-1}$) at 250 hPa (colour fill) and 2PVU contour at 325 K isosurface (red contour). Panels on the left depict the seasonal composites (all days of the season labelled on the top left of each map), while the panels on the right show composites centred 4 days prior to (i.e. on D-4) the 100 representative EPEs of each category

has a phase speed of $5\text{--}7^\circ\cdot\text{day}^{-1}$. Furthermore, the proximity between the northerly and southerly bands in Cat2 events implies that the typical wavelength of T_0 is smaller than in Cat1 events. Group velocity is generally lower than in Cat1 while the phase speed is not uniform in time and longitude.

Despite the visual impression of the composite, individual Cat2 events do show a connection between the North Pacific and North Atlantic storm tracks, as visible in the example case of the Piedmont flood. We suggest therefore that prior to some Cat2 EPEs, waviness over the Pacific may be out of phase but still enhanced and capable of seeding the North Atlantic storm track. Once the composite RWP signal in Cat2 has reached the North Atlantic a strong coherent amplification is noticeable.

Although largely associated with *in situ* non-equilibrium convection (Grazzini *et al.*, 2020a), Cat3 events show a similar composite RWP signal over the North Atlantic and Europe as in Cat2 (Figure 7c), but with lower amplitude. Relative to the other two categories, the RWP for Cat3 is characterized by a higher phase speed and smaller zonal wavelength.

4.2 | Category composites versus seasonal composites

After a first account on the RWP properties associated with the three EPE categories, it is worth investigating the role of the background flow seasonality in this respect. The natural tendency of the upper troposphere to form

waveguides for the propagation of RWPs has been investigated before. The emergence and efficiency of these waveguides essentially depend on the strength and shape of the jet stream (e.g. Manola *et al.*, 2013; Wirth *et al.*, 2018; Wirth, 2020). Idealized studies of Rossby wave propagation (Hoskins and Ambrizzi, 1993; Branstator, 2002) show that weak jets (associated with weak PV gradients) are typically associated with RWP propagation along great circles, whereas strong zonal jets lead to zonal ducting and longer propagation of the RWPs. The seasonal variability of the jet is associated with a corresponding variability in the mean RWP properties (Fragkoulidis and Wirth, 2020).

Previous studies have shown that the properties of the RWP precursor signal of EPEs in the Alpine area have a seasonal variability (Grazzini, 2007; Martius *et al.*, 2008). In the Martius *et al.* (2008) study in particular, composites of autumn and winter reveal a long and coherent RWP signal that is detectable over the North Pacific up to 7 days prior to the precipitation event. During spring, however, these studies report a short-lived equatorward propagation initiated in the western North Atlantic about 4 days prior to the event. It is therefore interesting to investigate whether the characteristic RWP properties of each EPE category are purely dependent on the period of the year they occur in. To this end, we first compare the jet composites of the three EPE categories with the respective seasonal climatologies, which reflect the annual cycle of the climatological waveguides.

We compare seasonal jet speed composites (all days) to jet speed composites 4 days prior to the occurrence of EPEs (Figure 8). The lag of 4 days allows us to focus on the jet properties prior to the direct influence by the

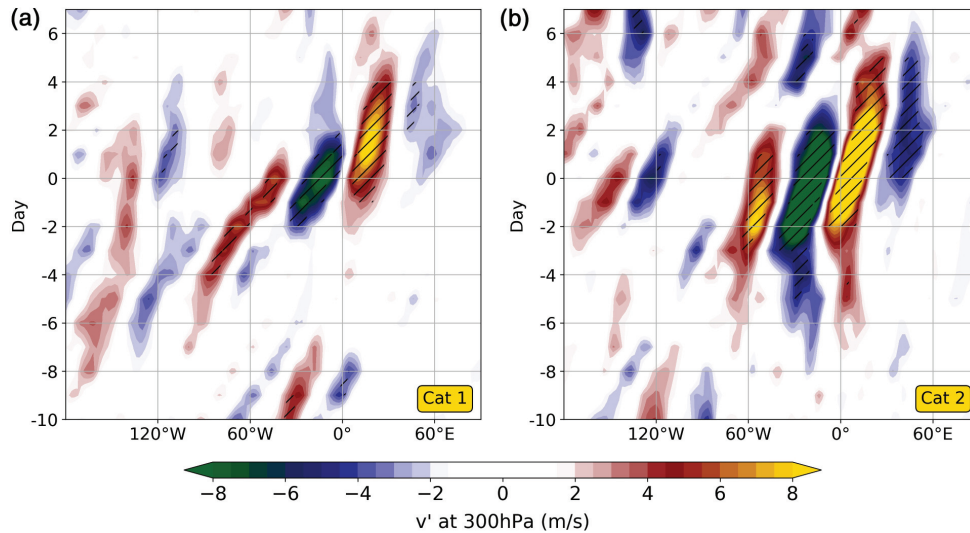


FIGURE 9 Composite Hovmöller plots of v' at 300 hPa, as in Figure 7, but for the (a) 59 Cat1 and (b) 35 Cat2 EPEs that occurred in November

wave associated with the EPE. Nevertheless, the following results do not change substantially for slightly different lags. The composite prior to Cat1 cases, which mostly occur in winter and late autumn (Figure 3d), is similar to the December–February (DJF) composite. An exception is that the Cat1 jet extends more towards Europe and is more intense and continuous over the continental USA, a characteristic which is common to the composites of all EPE categories. The fact that the Cat1 jet composite is similar to the DJF seasonal composite, and that the RWP Cat1 composite (Figure 7a) is similar to the Martius *et al.* (2008) winter composite, suggests that EPEs of this category are not too distinct from the typical winter circulation properties. In contrast, the Cat2 jet composite (Figure 8, middle right panel), instead, differs from the March–May (MAM) and September–November (SON) climatologies, while the Cat3 jet composite is similar to Cat2 but slightly weaker. Finally, we also note the prominent presence of the subtropical jet over the Mediterranean and North Africa in Cat1 events, while this is not the case in either the Cat2 or Cat3 composites.

The above might imply that in the transition seasons the large-scale flow associated with EPEs can vary substantially from the mean, sustaining different types of propagation according to the strength of the meridional PV gradient. To further investigate this point, we produce RWP composites based on all EPE cases (not just the 100 representative ones) that occurred in November, a month when both Cat1 and Cat2 EPEs are frequent. In particular, out of the 95 November EPEs, 59 are Cat1, 35 are Cat2, and 1 is Cat3. Therefore we can test whether in the same month there can be differences in the RWP propagation

associated with the two EPE categories. Indeed, Figure 9 shows distinct propagation patterns for November Cat1 and Cat2 EPEs, with a marked difference in the Pacific precursor part and the amplification over the North Atlantic. As in the full composite (Figure 7), Cat2 composite RWPs are still more confined in longitude. As a side note, June and September are also months when EPEs are not characterized by a distinctly preferable category (Figure 3).

4.3 | Water vapour transport and wave amplification over the Atlantic sector

In this section, we investigate the factors behind the strong amplification observed over the North Atlantic, that is evident in all categories and especially pronounced during Cat2 events, as seen in Figure 7. A strong amplification of the North Atlantic ridge is in fact a necessary condition for the evolution of the trough over western Europe into an elongated structure, able to drive significant water vapour transport toward Europe (Piaget *et al.*, 2015; Scoccimarro *et al.*, 2018). Although ridges are typically wider in longitude than troughs, as expected from the nonlinear dry primitive equations (Hoskins, 1975; Snyder *et al.*, 1991), Teubler and Riemer (2020) have shown that divergent outflow tends to increase ridge amplitude and to decrease trough amplitude systematically. Here we aim to address factors that further influence this asymmetry and that may vary between the EPE categories.

Many studies have shown the effect of diabatic heating in modifying the intensity of PV streamers and Rossby wave evolution downstream (Wernli and Davies, 1997;

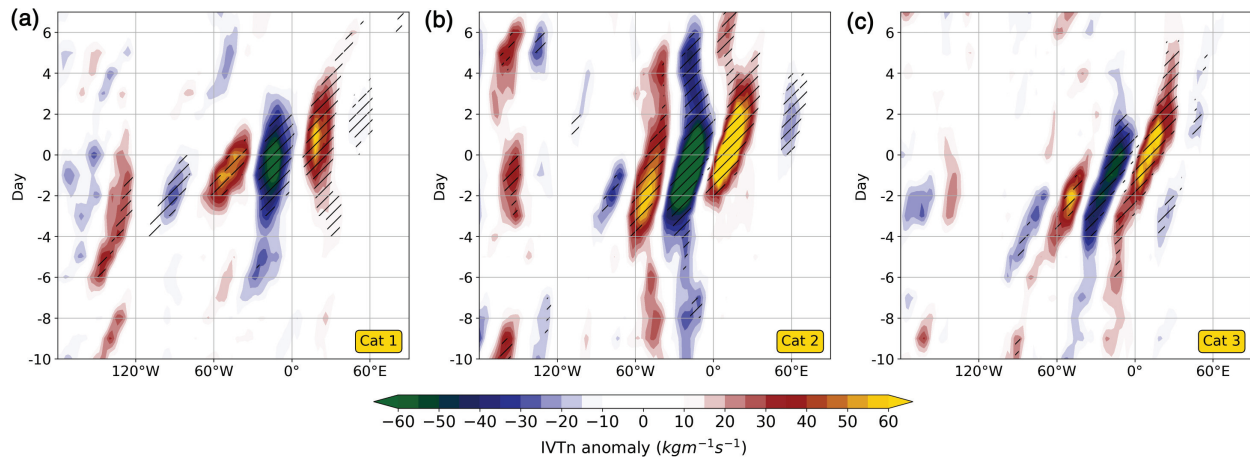


FIGURE 10 Composite Hovmöller plots of IVTn anomaly (colour fill, $\text{kg}\cdot\text{m}^{-1}\cdot\text{s}^{-1}$) during the 100 representative cases of (a) Cat1, (b) Cat2 and (c) Cat3 EPEs. For every longitude, IVTn anomaly is meridionally averaged over the 30° – 60° latitude band. The hatches indicate statistical significance at the 0.10 level

Grams and Archambault, 2016; Grams *et al.*, 2018). This occurs via the injection of low-PV air into the upper troposphere in a deep ascent of moist air streams which can originate from WCBs within extratropical cyclones and their embedded convection, or extratropical transition of tropical cyclones. The resulting upper-level negative PV anomaly can intensify the ridge downstream of the trough, strengthen the PV gradient and in general amplify the meridional elongation of the pre-existing streamer downstream of the ridge (Martius *et al.*, 2008). Numerical experiments with reduced meridional moisture transport and latent heat release lead to waves of substantially weaker amplitude (e.g. Grams and Archambault, 2016). Strong IVT convergence is, therefore, a typical precondition to achieve strong ridge amplification downstream on the target region; a feature that is characteristic of Cat2 events as will be shown later. Following this hypothesis, in this section we investigate the environment of the T_U system in the different categories, in search of mechanisms explaining the differences in the North Atlantic ridge amplification and the associated downstream development. In the next Section (4.4) we evaluate the contribution of different physical processes by adopting the PV tendency framework introduced in Section 2.4.

In Figure 10, we display composite Hovmöller diagrams of the meridional IVT (IVTn) anomaly. The first striking difference between the categories is the strong meridional water vapour fluxes occurring on the North Atlantic basin in Cat 2, beginning about 4 days before EPEs. Cat 1 EPEs are instead characterized by transient meridional IVT associated with a coherent and long-lasting wave packet that appears to form in the Pacific (180°W) at D-6. Cat 3 EPEs are similar to Cat 2, but with

weaker – although still statistically significant – water vapour transport.

In order to complement the information of Figure 10, in Figure 11 we display the North Atlantic 500 hPa geopotential height (full field and anomaly) and IVT anomaly composites at D-4, D-2 and D0. As a reference, the position of T_U is marked on Figure 11, whenever a close negative anomaly isoline (dashed) is evident. At D-4 in the Cat1 composite (Figure 11g) we note a stronger meridional height gradient compared to Cat2 and Cat3 (Figure 11h,i), which is consistent with the higher jet speed observed in Figure 8. An upstream trough (T_U) is located over Hudson Bay, and there is no apparent IVT anomaly or ridging over the North Atlantic associated with it. It is only at D-2 (Figure 11d), when it reaches the North Atlantic, that T_U starts to intensify, in association with a moderate positive IVT anomaly on its ascending branch and the strengthening of the wave downstream, as reflected in the geopotential height anomaly contours. The wave amplification continues until D0 when a particularly strong trough (T_0) dominates the flow over Europe (Figure 11a).

At D-4 for Cat2 EPEs, the T_U over North America is too weak to produce a closed contour in Figure 11h (weaker than -2gpdam), but positive IVT and geopotential height anomalies are apparent over the North Atlantic. A stronger amplification of the associated North Atlantic ridge is apparent on D-2 of Cat2 (Figure 11e) compared to Cat1, as indicated by the stronger positive geopotential anomaly. Furthermore, the Cat2 composite height anomalies over the North Atlantic imply waves of smaller wavelength than those of Cat1 events (as also suggested by the Hovmöller diagrams in Figure 7) and appear to be

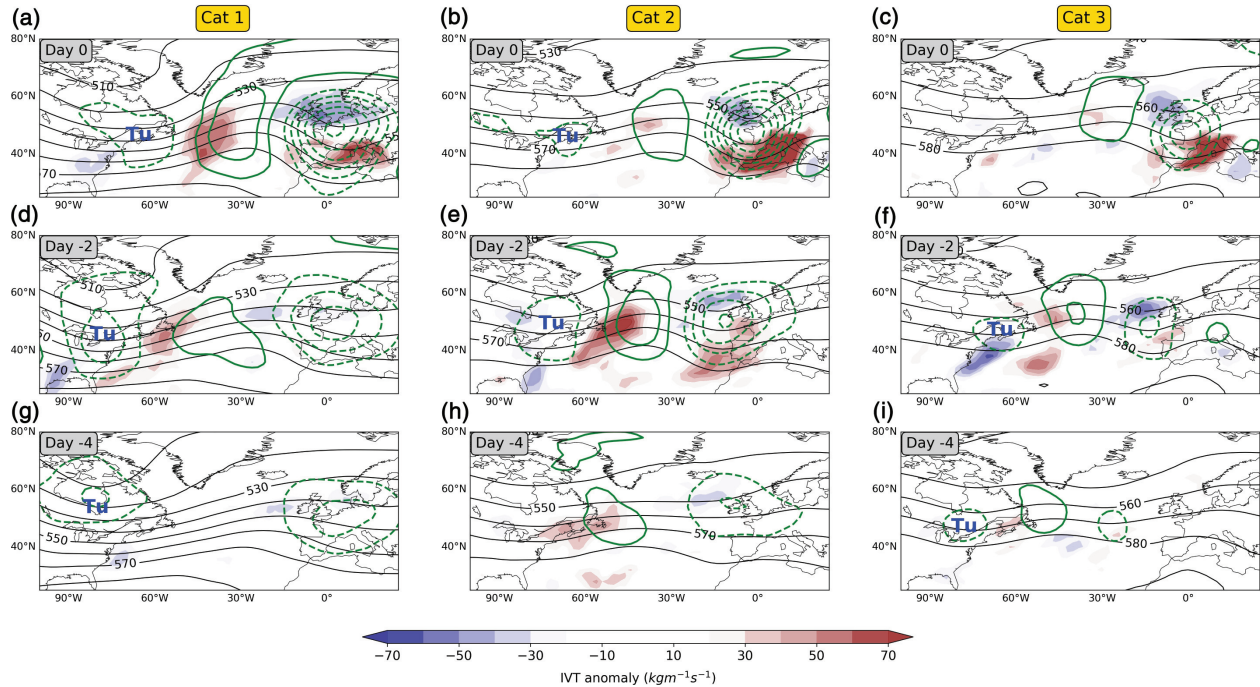


FIGURE 11 Composite maps of the IVT magnitude anomaly (colour fill, $\text{kg}\cdot\text{m}^{-1}\cdot\text{s}^{-1}$), geopotential height at 500 hPa (black contours every 10 gpdam), and geopotential height anomaly at 500 hPa (green contours at $\pm[2, 4, 6, \dots]$ gpdam; solid: positive anomalies, dashed: negative anomalies) at day 0 of the 100 representative (a) Cat1, (b) Cat2 and (c) Cat3 EPEs. Panels (d–f) correspond to day –2 and panels (g–i) correspond to day –4 of the three EPE categories respectively. The approximate position of the Tu trough is marked in blue

less influenced by upstream waves coming from North America. The latter hints at a more local forcing over the northern edge of the western boundary ocean current, as opposed to the Cat1 flow evolution described before. Finally, the large-scale flow prior to Cat3 EPEs is characterized by an overall weaker wave packet that amplifies slowly and has a shorter wavelength than the other two categories (see also Figure 7). In the next section, we investigate which processes are responsible for the more vigorous North Atlantic ridge amplification prior to Cat2 EPEs.

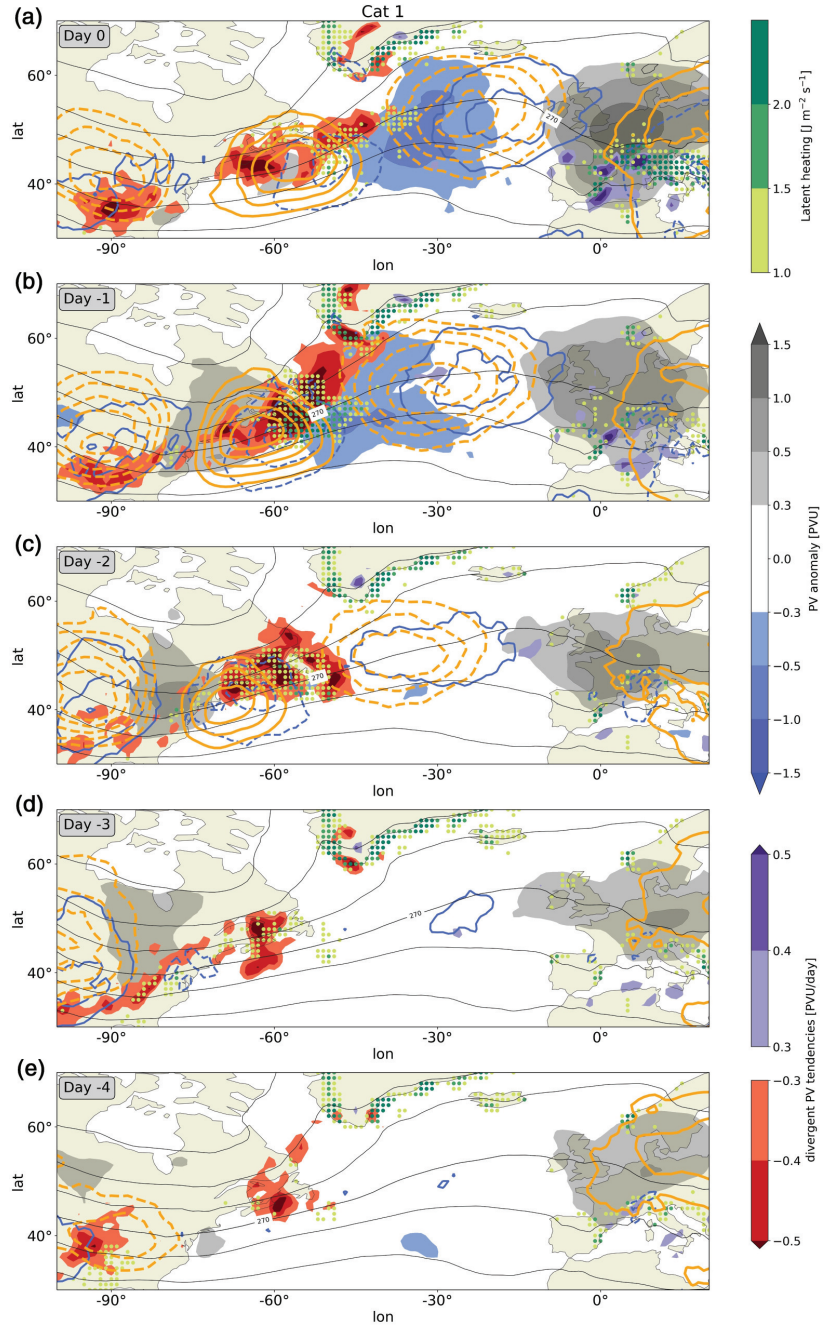
4.4 | PV tendency analysis of the precursor wave

In this section we investigate, in a composite sense, the contribution of individual processes, including latent heat release, to the spatio-temporal evolution of T_u and the respective downstream ridge. Since latent heating is not directly available in the ERA5 reanalysis, we employ a proxy based on the Lagrangian change in column water vapour: $\text{LHRproxy} = -L^*(\partial IWV/\partial t + \nabla \cdot IVT)$ (see equation [3] from Trenberth and Solomon (1994)). L denotes the latent heat of vaporization of water, IWV the

vertically integrated water vapour content, and IVT the vertically integrated water vapour transport as described before.

We will consider PV tendencies showing the contribution of quasi-barotropic propagation, baroclinic interaction, and divergent outflow to PV amplitude and neglect contributions to deformation and wave breaking. The role of these processes can be understood conceptually in terms of downstream baroclinic development in the PV framework (e.g. Wirth *et al.*, 2018). Downstream of an existing trough, a new ridge is created at the leading edge of an RWP due to quasi-barotropic (negative) PV advection. Subsequently, baroclinic interaction with the low-level temperature gradient is established, which reinforces the upper-level ridge by PV advection associated with low-level temperature anomalies. Baroclinic interaction is also associated with rising motions which will produce upper-tropospheric divergent outflow. Teubler and Riemer (2020) argued that such a ridge evolution is more precisely described as a downstream *moist*-baroclinic development, so as to include the contribution from moist processes. They showed that the impact of latent heat release on the PV amplitude is most effectively communicated by the enhancement of vertical motion and hence the divergent outflow.

FIGURE 12 (a–e) Composite maps of PV anomalies (blue-grey shading) and tendencies of the 100 representative Cat1 EPEs on days 0, –1, –2, –3 and –4. LHRproxy is shown by green coloured dots (only positive values shown). PV tendencies due to quasi-barotropic propagation (blue contours at $\pm[0.5, 1, 1.5, 2]$ PVU·day⁻¹), baroclinic interaction (orange contours at $\pm[0.04, 0.06, 0.08, 0.12]$ PVU·day⁻¹), and divergent outflow (red-purple shading). Solid contours refer to positive tendencies and dashed contours refer to negative tendencies. Grey lines refer to temperature at 850 hPa (every 10 K). The PV field and its tendencies correspond to the mean values between the 315–350 K isentropic levels



In Figures 12–14 we show composite maps of PV anomaly, LHRproxy, and PV tendencies at time lags from D0 to D-4 prior to Cat1, Cat2 and Cat3 EPEs. Starting with Cat1 events at D-4 (Figure 12e), the incoming baroclinic RWP (Figure 7a) can be identified over North America by the positive quasi-barotropic PV tendencies (solid blue contours) and negative baroclinic PV tendencies (dashed orange contour). However, the collocation of these tendencies is not favourable for mutual growth by baroclinic interaction. We also note the positive

PV anomaly (grey shading) and baroclinic PV tendencies over Europe, as a remnant of a previous wave over Europe (also evident in Figures 7a and 11g). The initially weak divergent outflow tendencies (red shading) and latent heating (LHRproxy indicated by coloured dots) at the North American east coast increase from D-4 to D-3 but do not have an apparent contribution to the North Atlantic ridge evolution. At D-2, however, the ridge development around 45°W is subject to moist-baroclinic development as indicated by the combination of enhanced

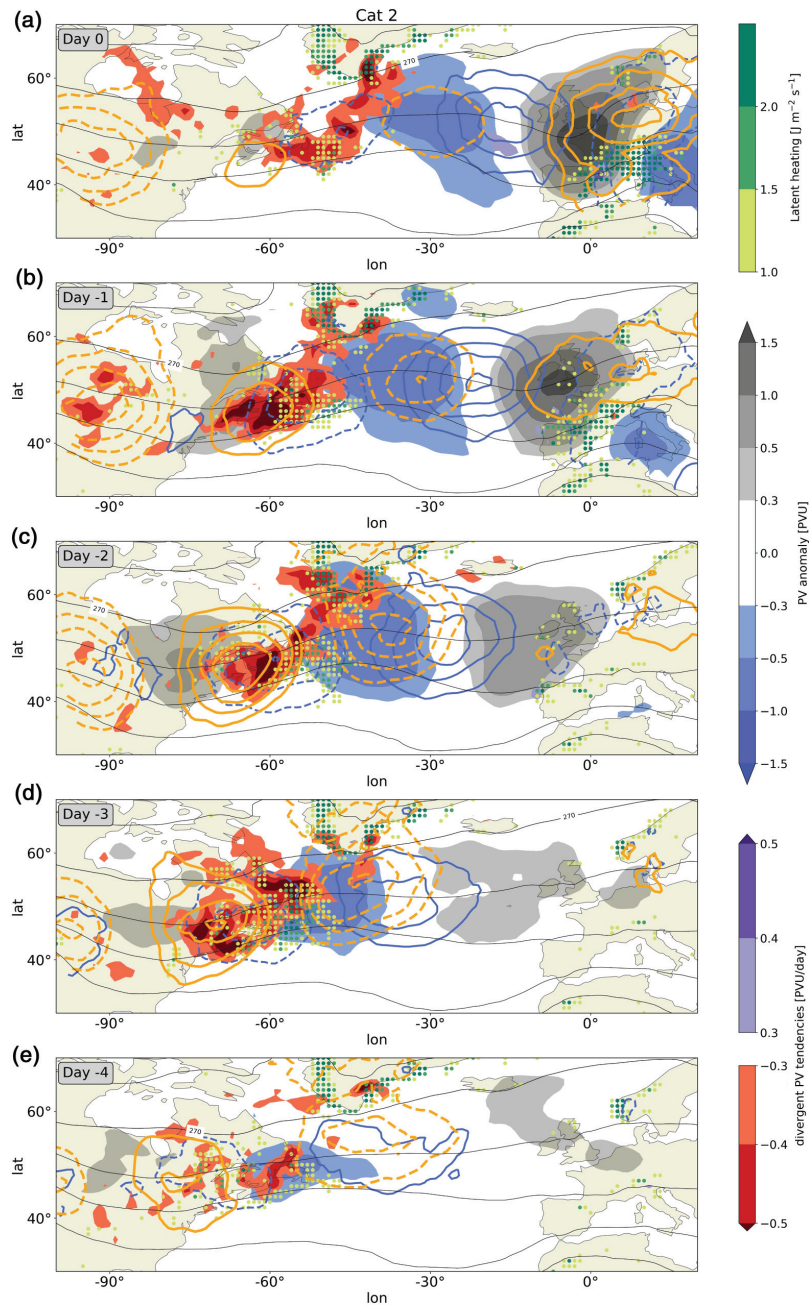


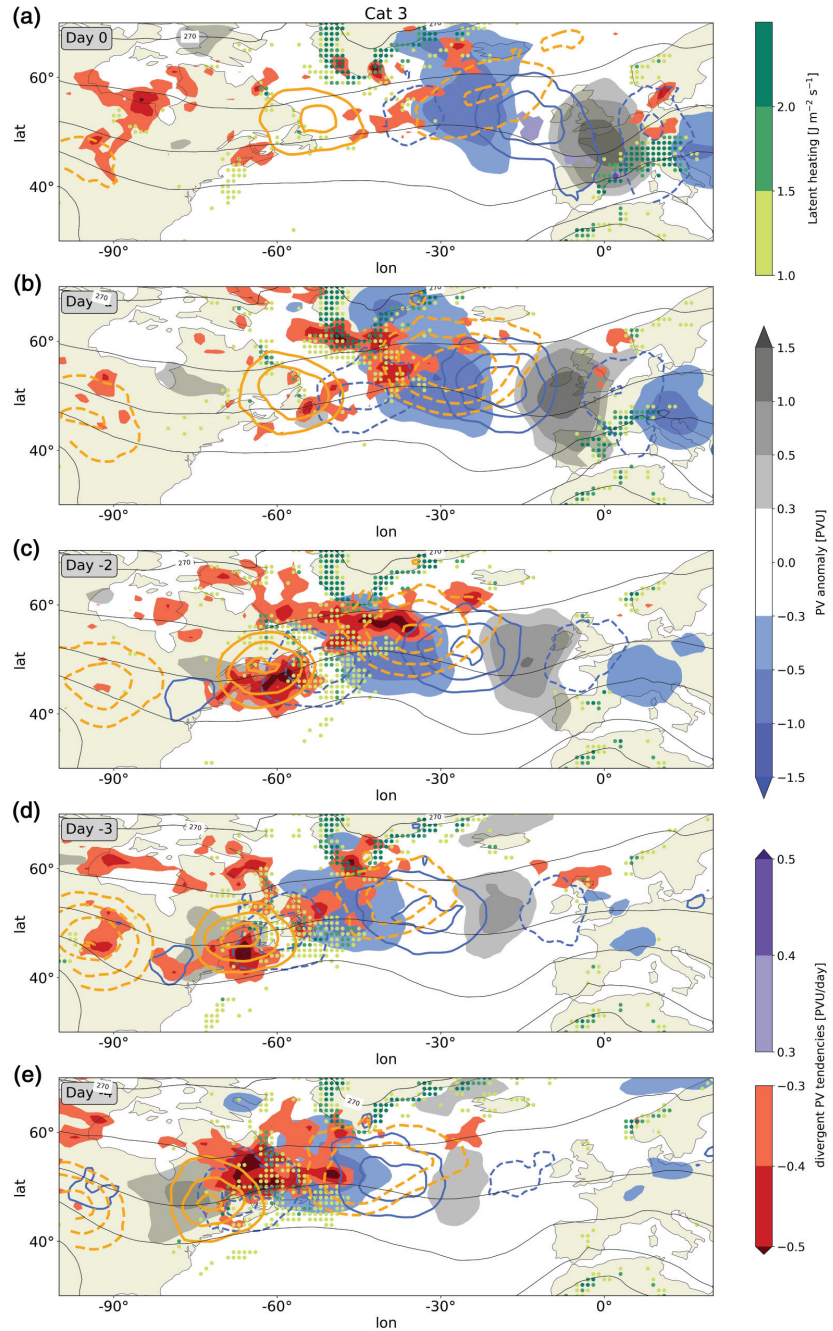
FIGURE 13 (a–e) The same as Figure 12 but for the composite of the 100 representative Cat2 EPEs

LHRproxy values, strong divergent outflow directly above, and negative baroclinic PV tendencies downstream. On the other hand, the pre-existing positive PV anomaly over Europe is amplified by *in situ* positive baroclinic PV tendencies and moves westward. Both the moist-baroclinic development and the amplification and westward shift of the positive PV anomaly over Europe contribute to the fast downstream propagation of the leading edge of the RWP from D-3 to D-2 (negative quasi-barotropic PV tendencies at D-3 around 75°W and positive tendencies at D-2 around 20°W). The peculiar merging of a developing

RWP with remnants of previous RWPs farther downstream could also be identified in the case considered by Teubler and Riemer (2016), which led to a high-impact weather event over Europe. Finally, from D-2 onwards the RWP amplifies further and propagates eastward subject to baroclinic downstream development that is indicated by the phase-shifted quasi-barotropic (blue contours) and baroclinic (orange contours) PV tendencies amplifying both troughs and ridges.

In contrast to the above evolution, the development of T_u and, even more so, the downstream North Atlantic

FIGURE 14 (a–e) The same as Figure 12 but for the composite of the 100 representative Cat3 EPEs



ridge for Cat2 and Cat3 events (Figures 13 and 14) is not triggered by an incoming RWP but appears to be forced locally at the North American east coast. As was also evident in the composite Hovmöller plots (Figure 7), neither Cat2 nor Cat3 events are associated with a precursor RWP signal over the North Pacific. At D-4 (Figure 13e), negative divergent PV tendencies and latent heating (LHRproxy is even stronger at D-5; not shown) are present in an area of negative PV anomaly over Newfoundland that falls in between regions with baroclinic and quasi-barotropic

PV tendencies. At D-3, the negative PV anomaly, the PV tendencies, and latent heating have all increased dramatically in magnitude, such that a large-amplitude RWP starts to develop downstream. On this day, the location of pronounced divergent PV tendency and LHRproxy values relative to the negative PV anomaly is conducive to a strong amplification of the ridge. The subsequent RWP propagation constitutes an archetypal example of downstream baroclinic development as described above with the ridge over the North American east coast being the source:

positive quasi-barotropic PV tendencies at the leading edge (around -35°W) form and intensify the trough downstream, while the ridge amplification is maintained by negative baroclinic and divergent PV tendencies. At D-2, a new positive PV anomaly develops at around 15°E reflecting the downstream propagation of the RWP. It is worth noting, that from D-3 onward a consistent and noticeable phase difference between baroclinic and quasi-barotropic tendencies is evident; a configuration that is particularly favourable to strong baroclinic downstream development.

The evolution of Cat3 events is similar to Cat2, but starts earlier and the PV anomaly and tendency fields have a weaker magnitude. The overall slower RWP propagation is associated with the weaker baroclinicity (grey lines) and jets associated with this category (Figures 8 and 11). Concerning the stronger North Atlantic ridge amplification in Cat2 and Cat3 compared to the corresponding Cat1 evolution, it is worth noting that the simultaneous presence of baroclinic interaction and substantial latent heating induces a particularly intense divergent outflow, leading to strong ridge amplification and high-amplitude RWPs. These findings are supported by the Teubler and Riemer (2020) study which showed, in a statistical sense, that both processes are similarly important for ridge building, and that high latent heat release is on average accompanied by strong baroclinic interaction (and vice versa). The strong IVT anomalies observed in the western North Atlantic in the days preceding Cat2 (Figure 11h) and, slightly less so, Cat3 (Figure 11i) events, along with the weaker jet conditions of the corresponding months, may therefore constitute perfect environmental conditions for strong ridge building and further downstream propagation.

5 | CONCLUSIONS

In this study we analysed the linkage between extreme precipitation events (EPEs) over northern-central Italy and the hemispheric evolution leading to the synoptic-scale wave that provides the dynamical forcing and water vapour transport convergence that are necessary for extreme precipitation over this area. We investigated a large number of EPEs that occurred between 1979 and 2015, subdivided into three categories identified in Part I of this study (Cat1, Cat2, Cat3) according to the thermodynamic and dynamic conditions over the target region. The three categories differ not only locally but also in the evolution of the upstream RWP precursor signal. In particular, the key results of this study can be summarized as follows:

- The three EPE categories have a different monthly distribution and are characterized by distinct spatial

patterns in precipitation, low-level wind, and moisture transport. These analyses add to the results of Part I and provide further insight into the characteristics of the three categories.

- The probability of heavy precipitation events in northern-central Italy increases with increasing waviness in the upper-tropospheric flow. This clear dependence is found for both Cat1 and Cat2 EPEs. In contrast, the probability of Cat 3 EPEs, which are mostly associated with thermodynamic instability and weakly-forced convection, does not increase with the magnitude of waviness.
- Differences in the evolution and characteristic properties of RWPs for the three EPE categories are evident. These differences are not purely explained by differences in the monthly distribution of the three categories, since they are still evident when restricting the analysis to November cases only.
- A comprehensive PV tendency analysis reveals pronounced differences in the dynamical processes leading to the RWP amplification over the North Atlantic that are crucial for the occurrence of Cat1 and Cat2 EPEs. Cat1 EPEs are characterized by (a) an incoming precursor wave signal from the North Pacific, (b) moist-baroclinic development over the North Atlantic, and (c) an interaction with a pre-existing upper-level positive PV anomaly over Europe. This combination leads to rapid downstream propagation of the leading edge of the RWP. In contrast, Cat2 EPEs arise from RWP amplification along the North American east coast, which is strongly invigorated by divergent outflow associated with latent heat release below. The subsequent downstream propagation is characterized by moist-baroclinic development and favoured by the phase difference between baroclinic and quasi-barotropic tendencies, so that a high-amplitude trough develops over western Europe.

These outcomes suggest that the occurrence of northern-central Italy EPEs depends not only on the local conditions, but also on the large-scale upper-tropospheric flow evolution in the days leading to the events. The particular severity of Cat2 EPEs appears to be the result of favourable conditions in both of these respects, that is, a warmer Mediterranean Sea in autumn and a more vigorous RWP amplification over the North Atlantic.

These results improve our understanding of the synoptic-scale dynamical and thermodynamical processes, providing further evidence on the role and properties of the upstream upper-tropospheric flow leading to EPEs. The processes and mechanisms involved in this regard are not only relevant for a better assessment of

the predictability and impact of these events, but also for their long-term trends. For example, all else being equal, a further increase in water vapour transport in the western North Atlantic, induced by global warming, could induce more frequent or stronger ridge building and downstream development of the kind observed in Cat2 EPEs. Consequently, further studies in this direction appear essential for advancing our knowledge on the occurrence of heavy precipitation events at weather and climate time-scales.

ACKNOWLEDGEMENTS

The research leading to these results has been done within the subproject T1, “Development of a predictability index for severe weather events over Europe”, as well as subprojects A8 (FT) and C4 (GF) of the Transregional Collaborative Research Centre SFB/TRR 165 “Waves to Weather” (www.wavestoweather.de) funded by the German Research Foundation (DFG). GF also acknowledges support from DFG under the project FR 4363/1-1. We would like to acknowledge our collaboration partner ARPAE-SIMC (Bologna, Italy) for contributing with data and in particular Gabriele Antolini for assistance in the production of Figure 1. Finally, we are very grateful to Olivia Martius and two anonymous reviewers for their suggestions which helped improve this study.

ORCID

Federico Grazzini  <https://orcid.org/0000-0002-3435-2376>

REFERENCES

- Barton, Y., Giannakaki, P., von Waldow, H., Chevalier, C., Pfahl, S. and Martius, O. (2016) Clustering of regional-scale extreme precipitation events in southern Switzerland. *Monthly Weather Review*, 144, 347–369. <https://doi.org/10.1175/MWR-D-15-0205.1>.
- Boers, N., Goswami, B., Rheinwalt, A., Bookhagen, B., Hoskins, B.J. and Kurths, J. (2019) Complex networks reveal global pattern of extreme-rainfall teleconnections. *Nature*, 566(7744), 373–377. <https://doi.org/10.1038/s41586-018-0872-x>.
- Branstator, G. (2002) Circumglobal teleconnections, the jet stream waveguide, and the North Atlantic Oscillation. *Journal of Climate*, 15(14), 1893–1910. [https://doi.org/10.1175/1520-0442\(2002\)015h1893:CTTJSWi2.0.CO;2](https://doi.org/10.1175/1520-0442(2002)015h1893:CTTJSWi2.0.CO;2).
- Brönnimann, S., Rajczak, J., Fischer, E.M., Raible, C.C., Rohrer, M. and Schär, C. (2018) Changing seasonality of moderate and extreme precipitation events in the Alps. *Natural Hazards and Earth System Sciences*, 18(7), 2047–2056. <https://doi.org/10.5194/nhess-18-2047-2018>.
- Charney, J. (1955) The use of the primitive equations of motion in numerical prediction. *Tellus*, 7, 22–26. <https://doi.org/10.3402/tellusa.v7i1.8772>.
- Davis, C.A. (1992) Piecewise potential vorticity inversion. *Journal of the Atmospheric Sciences*, 49, 1397–1411. [https://doi.org/10.1175/1520-0469\(1992\)049<1397:PPVI>2.0.CO;2](https://doi.org/10.1175/1520-0469(1992)049<1397:PPVI>2.0.CO;2).
- Dee, D.P., Uppala, S.M., Simmons, A.J., Berrisford, P., Poli, P., Kobayashi, S., Andrae, U., Balmaseda, M.A., Balsamo, G., Bauer, P., Bechtold, P., Beljaars, A.C.M., van de Berg, L., Bidlot, J., Bormann, N., Delsol, C., Dragani, R., Fuentes, M., Geer, A.J., Haimberger, L., Healy, S.B., Hersbach, H., Hólm, E.V., Isaksen, I., Kållberg, P., Köhler, M., Matricardi, M., McNally, A.P., Monge-Sanz, B.M., Morcrette, J.-J., Park, B.-K., Peubey, C., de Rosnay, P., Tavolato, C., Thépaut, J.-N. and Vitart, F. (2011) The ERA-Interim reanalysis: configuration and performance of the data assimilation system. *Quarterly Journal of the Royal Meteorological Society*, 137(656), 553–597. <https://doi.org/10.1002/qj.828>.
- Done, J.M., Craig, G.C., Gray, S.L., Clark, P.A. and Gray, M.E.B. (2006) Mesoscale simulations of organized convection: importance of convective equilibrium. *Quarterly Journal of the Royal Meteorological Society*, 132(616), 737–756. <https://doi.org/10.1256/qj.04.84>.
- Eady, E.T. (1949) Long waves and cyclone waves. *Tellus*, 1A, 33–52. <https://doi.org/10.1111/j.2153-3490.1949.tb01265.x>.
- Fragkoulidis, G., Wirth, V., Bossmann, P. and Fink, A.H. (2018) Linking Northern Hemisphere temperature extremes to Rossby wave packets. *Quarterly Journal of the Royal Meteorological Society*, 144(711), 553–566. <https://doi.org/10.1002/qj.3228>.
- Fragkoulidis, G. and Wirth, V. (2020) Local Rossby wave packet amplitude, phase speed, and group velocity: seasonal variability and their role in temperature extremes. *Journal of Climate*, 33, 8767–8787. <https://doi.org/10.1175/JCLI-D-19-0377.1>.
- Ghinassi, P., Fragkoulidis, G. and Wirth, V. (2018) Local finite-amplitude wave activity as a diagnostic for Rossby wave packets. *Monthly Weather Review*, 146(12), 4099–4114. <https://doi.org/10.1175/MWR-D-18-0068.1>.
- Grams, C. and Archambault, H. (2016) The key role of diabatic outflow in amplifying the midlatitude flow: a representative case study of weather systems surrounding western North Pacific extratropical transition. *Monthly Weather Review*, 144(10), 3847–3869. <https://doi.org/10.1175/MWR-D-15-0419.1>.
- Grams, C., Magnusson, L. and Madonna, E. (2018) An atmospheric dynamics perspective on the amplification and propagation of forecast error in numerical weather prediction models: a case study. *Quarterly Journal of the Royal Meteorological Society*, 144(717), 2577–2591. <https://doi.org/10.1002/qj.3353>.
- Grazzini, F. (2007) Predictability of a large-scale flow conducive to extreme precipitation over the western Alps. *Meteorology and Atmospheric Physics*, 95(3–4), 123–138. <https://doi.org/10.1007/s00703-006-0205-8>.
- Grazzini, F., Craig, G., Keil, C., Antolini, G. and Pavan, V. (2020a) Extreme precipitation events over northern Italy. Part I: A systematic classification with machine-learning techniques. *Quarterly Journal of the Royal Meteorological Society*, 146(726), 69–85. <https://doi.org/10.1002/qj.3635>.
- Grazzini, F., Fragkoulidis, G., Pavan, V. and Antolini, G. (2020b) The 1994 Piedmont flood: an archetype of extreme precipitation events in northern Italy. *Bulletin of Atmospheric Science and Technology*, 1–13. <https://doi.org/10.1007/s42865-020-00018-1>.
- Harris, F.J. (1978) On the use of windows for harmonic analysis with the discrete Fourier transform. *Proceedings of the Institute of Electrical and Electronic Engineers*, 66(1), 51–83.
- Hersbach, H., Bell, B., Berrisford, P., Hirahara, S., Horányi, A., Muñoz-Sabater, J., Nicolas, J., Peubey, C., Radu, R., Schepers, D., Simmons, A., Soci, C., Abdalla, S., Abellan, X., Balsamo, G.,

- Bechtold, P., Biavati, G., Bidlot, J., Bonavita, M., De Chiara, G., Dahlgren, P., Dee, D., Diamantakis, M., Dragani, R., Flemming, J., Forbes, R., Fuentes, M., Geer, A., Haimberger, L., Healy, S., Hogan, R.J., Hólm, E., Janisková, M., Keeley, S., Laloyaux, P., Lopez, P., Lupu, C., Radnoti, G., de Rosnay, P., Rozum, I., Vamborg, F., Villaume, S. and Thépaut, J.-N. (2020) The ERA5 global reanalysis. *Quarterly Journal of the Royal Meteorological Society*, 146(730), 1999–2049. <https://doi.org/10.1002/qj.3803>.
- Hoskins, B.J. (1975) The geostrophic momentum approximation and the semi-geostrophic equations. *Journal of the Atmospheric Sciences*, 32(2), 233–242. [https://doi.org/10.1175/1520-0469\(1975\)032%3C0233:TGMAAT%3E2.0.CO;2](https://doi.org/10.1175/1520-0469(1975)032%3C0233:TGMAAT%3E2.0.CO;2).
- Hoskins, B.J., McIntyre, M.E. and Robertson, A.W. (1985) On the use and significance of isentropic potential vorticity maps. *Quarterly Journal of the Royal Meteorological Society*, 111(470), 877–946. <https://doi.org/10.1002/qj.49711147002>.
- Hoskins, B.J. and Ambrizzi, T. (1993) Rossby wave propagation on a realistic longitudinally varying flow. *Journal of the Atmospheric Sciences*, 50(12), 1661–1671. [https://doi.org/10.1175/1520-0469\(1993\)050<1661:RWPOAR>2.0.CO;2](https://doi.org/10.1175/1520-0469(1993)050<1661:RWPOAR>2.0.CO;2).
- Isotta, F., Frei, C., Weigluni, V., Percec Tadic, M., Lassègues, P., Rudolf, B., Pavan, V., Cacciamani, C., Antolini, G., Ratto, S.M., Munari, M., Micheletti, S., Bonati, V., Lussana, C., Ronchi, C., Panettieri, E., Marigo, G. and Vartacnik, G. (2014) The climate of daily precipitation in the Alps: development and analysis of a high-resolution grid dataset from pan-Alpine rain-gauge data. *International Journal of Climatology*, 34, 1657–1675. <https://doi.org/10.1002/joc.3794>.
- Liu, B., Tan, X., Gan, T.Y., Chen, X., Lin, K., Lu, M. and Liu, Z. (2020) Global atmospheric moisture transport associated with precipitation extremes: mechanisms and climate change impacts. *WIREs Water*, 7. <https://doi.org/10.1002/wat2.1412>.
- Loriaux, J.M., Lenderink, G. and Siebesma, A.P. (2017) Large-scale controls on extreme precipitation. *Journal of Climate*, 30, 955–968. <https://doi.org/10.1175/JCLI-D-16-0381.1>.
- Manola, I., Selten, F., de Vries, H. and Hazeleger, W. (2013) “Waveguidability” of idealized jets. *Journal of Geophysical Research: Atmospheres*, 118, 10432–10440. <https://doi.org/10.1002/jgrd.50758>.
- Martius, O., Schwierz, C. and Davies, H.C. (2006b) A refined Hovmöller diagram. *Tellus A*, 58(2), 221–226. <https://doi.org/10.1111/j.1600-0870.2006.00172.x>.
- Martius, O., Schwierz, C. and Davies, H.C. (2008) Far-upstream precursors of heavy precipitation events on the Alpine south-side. *Quarterly Journal of the Royal Meteorological Society*, 134(631), 417–428. <https://doi.org/10.1002/qj.229>.
- Martius, O., Zenklusen, E., Schwierz, C. and Davies, H.C. (2006a) Episodes of Alpine heavy precipitation with an overlying elongated stratospheric intrusion: a climatology. *International Journal of Climatology*, 26(9), 1149–1164. <https://doi.org/10.1002/joc.1295>.
- Moore, B.J., Keyser, D. and Bosart, L.F. (2019) Linkages between extreme precipitation events in the central and eastern United States and Rossby wave breaking. *Monthly Weather Review*, 147(9), 3327–3349. <https://doi.org/10.1175/MWR-D-19-0047.1>.
- Pasquier, J.T., Pfahl, S. and Grams, C.M. (2019) Modulation of atmospheric river occurrence and associated precipitation extremes in the North Atlantic region by European weather regimes. *Geophysical Research Letters*, 46, 1014–1023. <https://doi.org/10.1029/2018GL081119>.
- Pavan, V., Antolini, G., Barbiero, R., Berni, N., Brunier, F., Cacciamani, C., Cagnati, A., Cazzuli, O., Cicogna, A., De Luigi, C., Di Carlo, E., Francioni, M., Maraldo, L., Marigo, G., Micheletti, S., Onorato, L., Panettieri, E., Pellegrini, U., Pelosini, R., Piccinini, D., Ratto, S., Ronchi, C., Rusca, L., Sofia, S., Stelluti, M., Tomozeiu, R. and Malaspina, T.T. (2019) High resolution climate precipitation analysis for north-central Italy, 1961–2015. *Climate Dynamics*, 52(5–6), 3435–3453. <https://doi.org/10.1007/s00382-018-4337-6>.
- Persson, A. (2017) The story of the Hovmöller diagram: an (almost) eyewitness account. *Bulletin of the American Meteorological Society*, 98(5), 949–957. <https://doi.org/10.1175/BAMS-D-15-00234.1>.
- Petrucci, O., Aceto, L., Bianchi, C., Bigot, V., Brázdil, R., Pereira, S., Kahraman, A., Kiliç, Ö., Kotroni, V., Llasat, M.C., Llasat-Botija, M., Papagiannaki, K., Pasqua, A.A., Řehoř, J., Geli, J.R., Salvati, P., Vinet, F. and Zêzere, J.L. (2019) Flood fatalities in Europe, 1980–2018: variability, features, and lessons to learn. *Water*, 11(8), 1682. <https://doi.org/10.3390/w11081682>.
- Piaget, N., Froidevaux, P., Giannakaki, P., Gierth, F., Martius, O., Riemer, M., Wolf, G. and Grams, C.M. (2015) Dynamics of a local Alpine flooding event in October 2011: moisture source and large-scale circulation. *Quarterly Journal of the Royal Meteorological Society*, 141(690), 1922–1937. <https://doi.org/10.1002/qj.2496>.
- Pinto, J., Ulbrich, S., Parodi, A., Rudari, R., Boni, G. and Ulbrich, U. (2013) Identification and ranking of extraordinary rainfall events over northwest Italy: the role of Atlantic moisture. *Journal of Geophysical Research: Atmospheres*, 118, 2085–2097. <https://doi.org/10.1002/jgrd.50179>.
- Pohorsky, R., Röthlisberger, M., Grams, C., Riboldi, J. and Martius, O. (2019) The climatological impact of recurving North Atlantic tropical cyclones on downstream extreme precipitation events. *Monthly Weather Review*, 147(5), 1513–1532. <https://doi.org/10.1175/MWR-D-18-0195.1>.
- Röthlisberger, M., Frossard, L., Bosart, L.F., Keyser, D. and Martius, O. (2019) Recurrent synoptic-scale Rossby wave patterns and their effect on the persistence of cold and hot spells. *Journal of Climate*, 32(11), 3207–3226. <https://doi.org/10.1175/JCLI-D-18-0664.1>.
- Rousseeuw, P.J. (1987) Silhouettes: a graphical aid to the interpretation and validation of cluster analysis. *Computational and Applied Mathematics*, 20, 53–65. [https://doi.org/10.1016/0377-0427\(87\)90125-7](https://doi.org/10.1016/0377-0427(87)90125-7).
- Scoccimarro, E., Gualdi, S. and Krichak, S. (2018) Extreme precipitation events over north-western Europe: getting water from the tropics. *Annals of Geophysics*, 61(4). <https://doi.org/10.4401/ag-7772>.
- Snyder, C., Skamarock, W.C. and Rotunno, R. (1991) A comparison of primitive-equation and semigeostrophic simulations of baroclinic waves. *Journal of the Atmospheric Sciences*, 48(19), 2179–2194. [https://doi.org/10.1175/1520-0469\(1991\)048%3C2179:ACOPEA%3E2.0.CO;2](https://doi.org/10.1175/1520-0469(1991)048%3C2179:ACOPEA%3E2.0.CO;2).
- Sodemann, H. and Zubler, E. (2010) Seasonal and inter-annual variability of the moisture sources for Alpine precipitation during 1995–2002. *International Journal of Climatology*, 30(7), 947–961. <https://doi.org/10.1002/joc.1932>.

- Teubler, F. and Riemer, M. (2016) Dynamics of Rossby wave packets in a quantitative potential vorticity–potential temperature framework. *Journal of the Atmospheric Sciences*, 73(3), 1063–1081. <https://doi.org/10.1175/JAS-D-15-0162.1>.
- Teubler, F. and Riemer, M. (2020) Potential-vorticity dynamics of troughs and ridges within Rossby wave packets during a 40-year reanalysis period. *Weather and Climate Dynamics*. <https://doi.org/10.5194/wcd-2020-52>.
- Trenberth, K.E. and Solomon, A. (1994) The global heat balance: heat transports in the atmosphere and ocean. *Climate Dynamics*, 10, 107–134.
- Wernli, B. and Davies, H. (1997) A Lagrangian-based analysis of extratropical cyclones. I: The method and some applications. *Quarterly Journal of the Royal Meteorological Society*, 123(538), 467–489. <https://doi.org/10.1002/qj.49712353811>.
- Winschall, A., Sodemann, H., Pfahl, S. and Wernli, H. (2014) How important is intensified evaporation for Mediterranean precipitation extremes? *Journal of Geophysical Research: Atmospheres*, 119(9), 5240–5256. <https://doi.org/10.1002/2013JD021175>.
- Wirth, V., Riemer, M., Chang, E.K. and Martius, O. (2018) Rossby wave packets on the midlatitude waveguide: a review. *Monthly Weather Review*, 146(7), 1965–2001. <https://doi.org/10.1175/MWR-D-16-0483.1>.
- Wirth, V. (2020) Waveguidability of idealized midlatitude jets and the limitations of ray tracing theory. *Weather and Climate Dynamics*, 1, 111–125. <https://doi.org/10.5194/wcd-1-111-2020>.
- Zimin, A.V., Szunyogh, I., Patil, D.J., Hunt, B.R. and Ott, E. (2003) Extracting envelopes of Rossby wave packets. *Monthly Weather Review*, 131(5), 1011–1017. [https://doi.org/10.1175/1520-0493\(2003\)131h1011:EEORWPI2.0.CO;2](https://doi.org/10.1175/1520-0493(2003)131h1011:EEORWPI2.0.CO;2).
- Zimmer, M., Craig, G.C., Keil, C. and Wernli, H. (2011) Classification of precipitation events with a convective response timescale and their forecasting characteristics. *Geophysical Research Letters*, 38, L05802. <https://doi.org/10.1029/2010GL046199>.

How to cite this article: Grazzini F, Frangkoulidis G, Teubler F, Wirth V, Craig GC. Extreme precipitation events over northern Italy. Part II: Dynamical precursors. *QJR Meteorol Soc.* 2021;1–21. <https://doi.org/10.1002/qj.3969>

Chapter 4

EPE predictability

Predictability is intimately linked to the particular type of dynamical evolution. The accuracy of the forecast depends on how rapidly separate solutions of the equations of motion diverge (Lorenz, 1969b), a property which is tightly related to the processes. Therefore it is important to study the intrinsic or potential predictability of EPEs conditioned to the processes, in our study represented by the different categories. As we have seen in Section 3.3 (in paper Part II, Fig.6) Cat1 and Cat2 show a closer dependency on the large-scale dynamics so we expect them to be more predictable than Cat3 events dominated by weakly forced convective events. In this chapter we are presenting unpublished results based on the analysis of two potential predictability indexes. The aim is to verify the hypothesis that different EPEs possess different intrinsic predictability.

4.1 Potential predictability

In order to test the hypothesis of different EPE predictability, it is necessary to analyse a sufficiently large number of EPEs to be able to construct a reliable statistic. To do so we made use of a re-forecast of past cases, the ECMWF ensemble reforecast suite, fully described in section 2.3.3. It is a reduced ensemble (only 11 members), compared with 51 members of the operational version, but it has the advantage to be consistently run with the latest IFS model cycle and therefore allows comparing forecasts for EPE over the last 20 years with an up to date and homogeneous forecasting system. This choice allowed to have a statistics based on more than 30 EPE cases for each category and for each forecast-step considered. We have selected two indices for measuring potential predictability: the Normalised Precipitation Spread (NPS) and the Potential Predictability Index (PPI) described in section 2.5 .

With complementary characteristics, both indexes are measuring the dispersion of the ensemble in predicting precipitation for a given case: the NPS provides the average spread computed independently over each case, while for the PPI r^2 refers to the correlation computed over series including all cases and then averaging over ensemble members. The latter therefore is more influenced by outliers and it is a less robust measure than the former.

The stratification of the results per EPE category allows to assess the degree of potential predictability conditioned to the process responsible for a given class of events. Figure 4.1 shows the value of NPS as a function of forecast time step every 24h for Cat1, Cat2 and Cat3. We show three curves: for the whole Northern Central Italy (see the blue box in Fig. 2.1) -all-, for flat and mountain WA respectively. Potential predictability decreases when NPS is increasing. NPS below 1 means good potential predictability since the spread (noise) is much smaller than the median (signal) while values significantly above 1 (beyond 1.5 or greater) are pointing to almost a total loss of predictability. On the contrary PPI values equal to one are indicating a perfect predictability while 0 means no predictability. Lavers et al. (2014) propose to use the threshold 0.5 to separate predictable forecasts.

The first general consideration is that NPS increase rapidly with time but less where significant orography is present. Higher predictability for mountain warning areas is particularly true for Cat3 cases, but also Cat2 which contains deep convection embedded. The prominent role of local direct thermal circulation in maintaining weakly-forced convective precipitation close to the mountains increase the predictability over these regions. This result backs up what has already been found by Bachmann et al. (2020) about convection in Germany. Through a series of idealised perfect model setup experiments and realistic simulations, they find an increased predictability of precipitation close to the orography.

In Cat1, in which the precipitation is tightly related with the position of the front, the difference between flat areas and mountains is very small. Surprisingly we note in Cat1 a faster loss of predictability in the shorter forecast ranges which we think could be attributed to the interaction of the moist airflow associated with a frontal structure or a surface cyclone with the orography, highly dependent on the phase of the incoming wave. In Cat2 the presence of prefrontal deep convection produces events with longer duration and larger area extensions ($10.000km^2$ on average against $5000km^2$ for Cat1, see Fig.7 in Part I) in which phase error might intrinsically reduced. The fast error growth in Cat1 is an unexpected result which contradicts the initial hypothesis that Cat1 and Cat2 should have higher predictability due to their higher linkage with the large-scale dynamics.

A similar behaviour emerge also from the analysis of the PPI index, displayed in Fig. 4.2 although differences amongst categories are smaller. In this metric the difference in predictability between flat and mountain areas is reduced in Cat3 in the medium-range, but still significant up to D+4. While in Cat2 the behaviour is comparable with that observed in NPS. In Cat1 we also observed a vanishing difference between mountain and flat areas and more rapid loss of predictability despite starting from higher absolute levels at D+1. For Cat1 events the limit of potential predictability seems to be reached at D+4 when PPI drops below 0.5. At the same time NPS is about 1.6 for mountains areas and 1.75 for flat areas for Cat1, so already above 1.5 which is the threshold we consider for NPS. The 1.5 value of NPS is reached at about 3.5 days in Cat1. In Cat3 the predictability horizon is about D+3 on the NPS (mountain areas, even shorter for flat areas) and D+4 with PPI index.

Very interestingly in Cat2 we observe, in both metrics, a longer predictability horizon with a gain of almost one day of predictability. In Cat2 PPI drops below 0.5 between D+4 and D+5 while NPS value above 1.5 are reached almost at D+5.

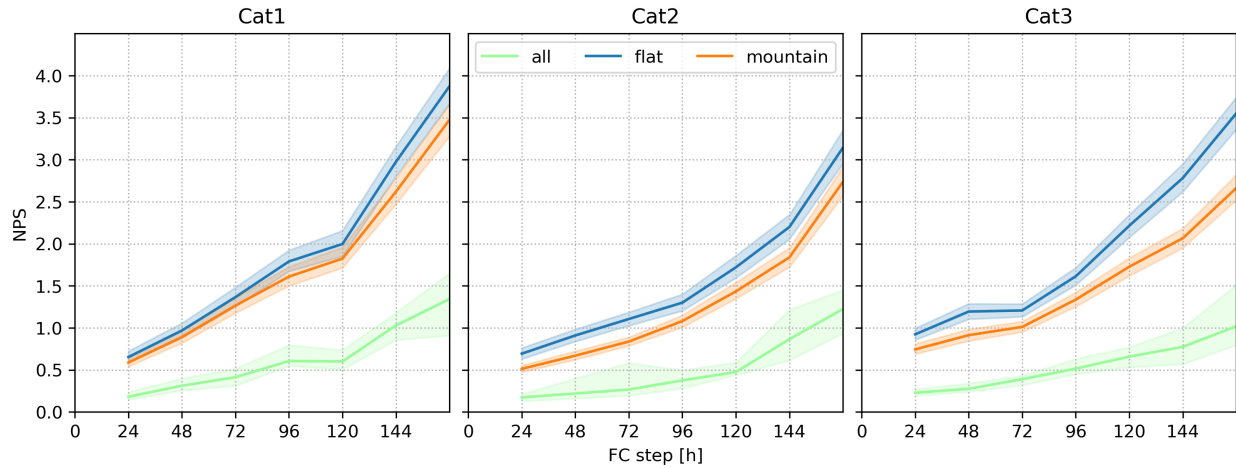


Figure 4.1: Area average Normalised Precipitation Spread (IQR/media) with associated confidence interval. In All the score is computed over the whole Northern Central Italy; Flat and Mountain are respectively the average of the score over all flat and mountain warning areas.

While the flat and mountains curves NPS and PPI are computed over single WA and then averaged, so measuring average potential predictability over single WAs, the green curve (all) show indexes computed averaging precipitation over the whole Northern Central Italy domain. As expected predictability is considerably higher over a such larger domain, indicating that most of the uncertainty regards the correct positioning of the precipitation in each WA, rather than the presence or not of the EPE inside the whole domain. In Fig. 4.1, if we fix for example NPS at 1, we obtain this level of predictability at D+2 for WAs in Cat1 while over the whole domain this is achieved at D+6, and even larger for Cat2. We can interpret the curve -all- as the potential predictability of having an EPE (yes/no) somewhere in the domain, which, according to this index, stays predictable up to the end of the medium range, while less dramatic difference amongst the two groups of curves is evident in the PPI index.

Finally we try to asses the predictability over each single WA to highlight other geographical dependencies in addition to flat versus mountain areas, like the direction of the flow respect to the orography which is changing with the category (see Fig. 2 of Part II: Dynamical precursors). In Fig. 4.3 we display a heatmap of NPS for each WA against forecast time step. The localisation of the WA can be visualised in 2.1. Yellowish colours are marking areas/forecast times in which potential predictability is still good, while dark blue colors are showing an almost total loss of predictability. In Cat2 yellowish colours reach longer forecast steps indicating again, as we have seen in the aggregated plot above, higher predictability for this EPE category compared to Cat1 and Cat3. This is particularly true on the left side of the plot which is showing western northern Italy WAs, while on the potential predictability is general shorter on the eastern areas (right part of the plot).

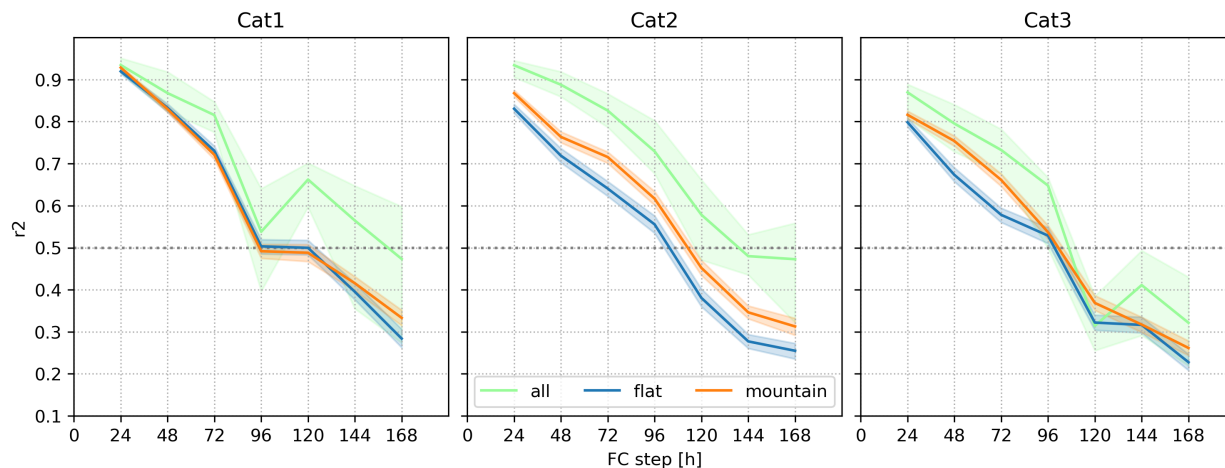


Figure 4.2: Potential Predictability Index (square of pearson corr , between single ens members and ens mean removing the member). In All the score is computed over the whole Northern Central Italy; Flat and mountain are respectively are the average of the score over all flat and mountain warning areas

The longitudinal dependency is also visible in Cat3 while in Cat1 this is not evident. This is confirmed also by the PPI index on a different aggregation on administrative regions (not shown) which confirms substantially higher predictability in the western and eastern Alps and Ligurian Apennines, more exposed to straight meridional flow associated with meridional configurations. Higher predictability in these regions is then attributable to the type of synoptic configuration of Cat2 events characterized by a stronger meridional flow, and even small phase errors in the forecast are not so detrimental due the structure of the orographic barrier which impose particularly strict boundary to the flow coming from the southerly direction.

4.2 Summary

An assessment of potential predictability of Cat1, Cat2 and Cat3 has been conducted analysing the re-forecast of a subsamples of EPEs in the last 20 years. Two indexes were used to evaluate the EPE *potential predictability* on different area aggregations. As expected Cat3 exhibit a faster loss of predictability in the medium-range, and especially over flat areas, due to the presence of weakly forced convection. If the result above was expected, it came as surprise to observe Cat1, starting from higher potential predictability, rapidly loose this advantage, becoming less or equally predictable than Cat2, already after three days. The predictability horizon of Cat2 events is in fact about one longer than Cat1 and Cat3 events, reaching almost two days difference in the NPS score for mountain areas. Being Cat1 characterized by more coherent RWPs, and hence thought to have

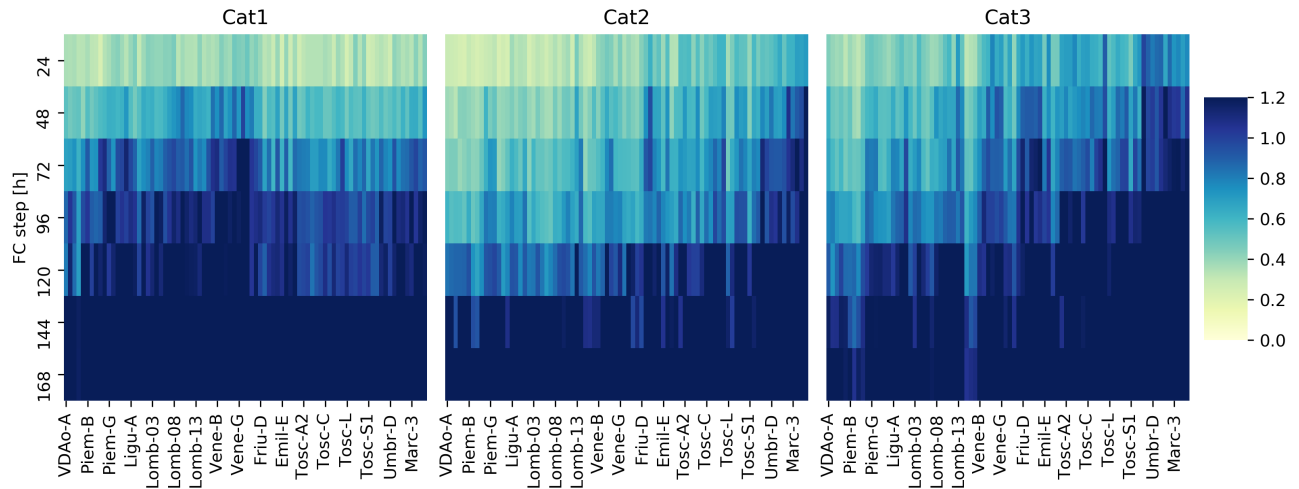


Figure 4.3: Heat map of NPS value for each WA and forecast step

a more predictable precursor, the faster loss of predictability in the shorter comes as a contradiction. One possible explanation is that Cat1 events are associated with a frontal structure or a surface cyclone and the interaction with the orography is highly dependent on the phase of the incoming wave. On the contrary Cat2, which distinguish itself to be more severe due to higher precipitation intensity and longer duration are probably less affected by small phase errors in the positioning of the wave. In that respect, the anchoring of deep convection in the prefrontal part of the system to the orography, can act as more predictable and slowly moving feature. However better predictability in Cat2 may also be linked to their peculiar dynamics and large anomalies of the water vapour transport in the upstream trough described in the third paper. The presence of significant orography, specifically investigated stratifying the results in two categories (flat and mountain areas) it is also important. Orography has a beneficial impact on predictability especially in Cat2 and Cat3 (characterized by the presence of convection) while it is rather marginal for Cat1. In a more detailed investigation of predictability over each area we noted that over western areas, more prone to prefrontal activity, predictability is significantly higher. This west-east difference in predictability is less visible in Cat1. As this anchoring effect is missing in Cat1, since the waves are travelling faster, the rapid growth growth in Cat1 is likely to be attributed to the uncertainty of phase of the frontal (and upper-wave) passage, which is dominating on other factors.

Chapter 5

Conclusions

This research presented in this dissertation contributed to the knowledge of the dynamics and the predictability of extreme precipitation events (EPEs), one of the natural hazards with high impact on human society. The research was specifically designed to provide insights and additional information to forecasters and the scientific community on the physical and dynamical drivers associated with extreme precipitation. To test the rationale behind our approach, we focus on Northern-Central Italy. The choice is motivated by the high frequency of these events on the area and the availability of high-resolution gridded observational dataset. The development of the research led to the publication of three scientific papers which are at the heart of this dissertation which address three different questions. The first important goal was to design an original and objective method to classify EPEs according to the different atmospheric setting and processes in which they originate. This classification is addressed in the first scientific paper (**EPE classification**) but is also used in the rest of project. In the second paper (**The 1994 Piedmont flood**) we revisit a well-known extreme event, which caused enormous losses in Northern Italy, in the context of our new classification methodology, showing that it is falling in the most severe category. Through the analysis of this case we try to identify also possible strategies for the use of real-time classification. The second research question concerns the detailed analysis of different large-scale evolution pathways leading to EPEs. It is explored through the use of composites and PV diagnostic in the third paper (**Dynamical precursors**). This investigation help to breakdown a complex phenomenon in their main components, in the aim to identify recurring large-scale patterns. Finally, the third research question, is addressed in an unpublished part and us about the identification of predictability dependencies on the EPE category and associated and large-scale patterns. It is presented in Chapter 4.

In this closing section, the key results of the papers and from the predictability chapter will be summarised and put in the wider context of current research and challenges of operational weather forecasting.

5.1 EPE classification

Summary: In this article, we describe a methodology for identification and systematic classification of extreme precipitation events (EPEs) over northern–central Italy. EPEs are defined as days when at least in one of the Italian Civil Protection warning-area units the spatially average daily precipitation is greater than the 99th percentile of the daily climatological distribution (1979–2015). The computation is based on a gridded archive built from quality controlled high-resolution regional observation networks. This archive, in combination with ERA-Interim reanalysis data for upper-level atmospheric fields, allows a 10-fold increase in the number of EPEs compared to previous studies; 887 EPEs are found and a subdivision in three predefined categories, with machine-learning, is proposed. According to upper-level predictors, three main scenario generating EPEs are recognized: frontal or mechanical orographic uplift of moist statically stable flow for Cat1, stronger frontal and mechanical uplift of a neutrally moist/warmer stable flow for Cat2, and finally thermally forced deep convective ascent for Cat3. In all categories IVT is anomalously high. EPEs are largely controlled by the intensity of the meridional component of vertically integrated vapour transport (IVT_n) that in turn depends not only on moisture availability but also on a favourable phasing of the upper-level wave with respect to the target area. This confirms IVT as an important large-scale predictor, especially for Cat2 events, shown to be the most relevant category in terms of effects and EPE area extension.

Applications: The proposed classification, based on widely used machine-learning methods, has the advantage that it can be easily applied elsewhere, since no subjective choice of fixed thresholds is necessary. The categorization of precipitation introduces simplifications compared to full complexity of nature, but it is very useful for gaining a clearer picture of the basic processes. This approach can raise forecaster awareness of the origins of high impact weather phenomena and of different kind of EPEs, fostering a more critical interpretation of numerical model output. In addition, moving to research aspects, the study sets the stage to investigate the relation between EPEs and Rossby wave packets. The importance of IVT is here confirmed and opens the way to methods which could exploit the longer predictability of this variable. Focussing on the predictable scales of motion and processes could be a way to push the range of prediction of EPE to longer time scales, while nowadays being limited to maximum a few days due to the intrinsic lower predictability of precipitation.

5.2 The 1994 Piedmont flood

Summary: In this study, we have revisited the dynamical evolution of the 1994 Piedmont flood event with new reanalysis and high-resolution precipitation datasets and in the light of EPE classification approach. We have shown that this event may be considered an archetype for southern Alpine Cat2 EPEs which are able to produce very high river discharges and widespread flooding on small and large river basins due to the combined presence of stratiform precipitation and deep convection. The main triggering factor was a

meridionally elongated upper-level trough, embedded in an incoming Rossby wave packet that originated in the Pacific. The wave packet propagation modulated the transport of a large moisture quantity from the central Atlantic towards the Mediterranean, with a formation of an AR over the central Mediterranean Sea. We also documented the presence of hurricane Florence in the central Atlantic in the days before the events, which interacted with the upstream trough and arguably contributed to strengthen the downstream development of the synoptic wave responsible for the precipitation.

Applications: The detailed reanalysis of this case study was also useful to test a possible practical approach toward an operational classification algorithm of EPE. A comparison of IVT distribution amongst EPEs and noEPE cases, show that EPE have a fairly separate distribution amongst Cat1, Cat2 and Cat3 and all of them are shifted towards large values compared to non EPE cases. This confirm IVT, and in particular of IVT_n, as one of the most important precursors although is to be considered not isolation but in combination of other variables, since considering only water vapour fluxes may lead to higher false alarm rate than using precipitation in the shorter forecast ranges. The analysis of this case showed also the added value of comparing single cases (as the one which could be identified in the forecast applying the classification method) with a catalogue of previous events in which effect, like the mean precipitation intensity, area above EPE thresholds, flooding area are known. Having the possibility of ranking a new forecast event is important for operational practice in order to enrich forecaster knowledge of possible scenarios based on real data.

5.3 Dynamical precursors

Summary: In this final paper we analysed the linkage between EPEs and the hemispheric evolution leading to the synoptic-scale wave that provides the dynamical forcing and water vapour transport convergence needed for these extreme events. We investigated a large number of EPEs that occurred between 1979 and 2015, subdivided into three categories identified in the first paper (Part I), and actualized with ERA5 reanalysis. The three categories differ not only locally but also in the evolution of the Rossby wave packet leading (RWP) to the event. The key results of this study can be summarized as follows:

1) The three EPE categories have a different monthly distribution and are characterized by distinct spatial patterns in precipitation, low-level wind, and moisture transport.

2) The probability of heavy precipitation events in northern-central Italy increases with increasing waviness in the upper-tropospheric flow. This clear dependence is found for both Cat1 and Cat2 EPEs. In contrast, the probability of Cat 3 EPEs, which are mostly associated with thermodynamic instability and weakly-forced convection, does not increase with the magnitude of waviness.

3) Differences in the evolution and characteristic properties of RWPs for the three EPE categories are evident. These differences are not purely explained by differences in the monthly distribution of the three categories, since they are still evident when restricting the analysis to November cases only.

4) A comprehensive PV tendency analysis reveals pronounced differences in the dynamical processes leading to the RWP amplification over the North Atlantic that are crucial for the occurrence of Cat1 and Cat2 EPEs. Cat1 EPEs are characterized by (a) an incoming precursor wave signal from the North Pacific, (b) moist-baroclinic development over the North Atlantic, and (c) an interaction with a pre-existing upper-level positive PV anomaly over Europe. This combination leads to rapid downstream propagation of the leading edge of the RWP. In contrast, Cat2 EPEs arise from RWP amplification along the North American east coast, which is strongly invigorated by divergent outflow associated with latent heat release below. The subsequent downstream propagation is characterized by moist-baroclinic development and favoured by the phase difference between baroclinic and quasi-barotropic tendencies, so that a high-amplitude trough develops over western Europe.

These outcomes suggest that the occurrence of northern-central Italy EPEs depends not only on the local conditions, but also on the large-scale upper-tropospheric flow evolution in the days leading to the events. The particular severity of Cat2 EPEs appears to be the result of favourable conditions in both of these respects, that is, a warmer Mediterranean Sea in autumn and a more vigorous RWP amplification over the North Atlantic.

Applications: These results improve our understanding of the synoptic-scale dynamical and thermodynamical processes, providing further evidence on the role and properties of the upstream upper-tropospheric flow leading to EPEs. The processes and mechanisms involved in this regard are not only relevant for a better assessment of the predictability and impact of these events, but also for their long-term trends. For example, all else being equal, a further increase in water vapour transport in the western North Atlantic, induced by global warming, could induce more frequent or stronger ridge building and downstream development of the kind observed in Cat2 EPEs. This subdivision in different large-scale evolution, open the way to investigate the trends, not only of the EPE but also of their dynamical precursors in the effort to disentangle the contribution coming from the dynamical changes, from the ones due to thermodynamic effect associated with the increase of global temperature.

5.4 Predictability

Summary: An assessment of potential predictability of Cat1, Cat2 and Cat3 has been conducted analysing the ECMWF EPS reforecast on a sample of EPEs in the last 20 years; two indexes are used to evaluate potential predictability on different area aggregations. As expected Cat3 exhibit a faster loss of predictability in the medium-range, and especially over flat areas, due to the presence of weakly forced convection. If the result above was expected, it came as surprise to observe Cat1, starting from higher potential predictability, rapidly loose this advantage already in the short range, becoming less or equally predictable than Cat2, a category in which deep convection is also present, already at D+3. Being Cat1 characterized by more coherent RWPs (as shown in Paper 2), and hence thought to have a more predictable precursor, the faster loss of predictability in the shorter forecast ranges it

is seemingly in contradiction. One possible explanation is that Cat1 events are associated with a frontal structure or a surface cyclone and the interaction with the orography is highly dependent on the phase of the incoming wave. On the contrary Cat2, which distinguish itself to be more severe due to higher precipitation intensity, longer duration, and affecting a large area the 24h accumulated precipitation is less sensible to small phase errors. In this could play a role also the presence of deep convection in the prefrontal part of the system which act as constant feature largely dependent by the interaction of the slowly varying (compared with Cat1) impinging flow and the orography. However better predictability in Cat2 may also be linked to their peculiar dynamics and large anomalies of the water vapour transport in the upstream trough described in the third paper. The presence of orography is investigated stratifying the results in two categories, flat and mountain areas. Orography has a beneficial impact on predictability especially in Cat2 and Cat3 (characterized by the presence of convection) while it is rather marginal for Cat1. For Cat2 is also noticeable a large spread in predictability from western areas more prone to prefrontal activity, where predictability is significantly higher, and eastern areas where is lower. This west-east difference in predictability is not visible in Cat1. This is also suggesting that in Cat1 the uncertainty in the phase of the frontal (and upper-wave) passage is dominating on other factors.

Applications: The concept of different predictability of EPEs can be useful in the field of operational forecasting and for weather warning procedures. Relying on the reanalysis as a training dataset, it is possible to compute the probability of four EPE categories (NoEPE days, EPE days of Cat1, Cat2, Cat3), for each day in real-time forecast, with a random forest classifier algorithm. Once a day is classified, additional information on the deterministic limit over each area and for each category (measured by threshold on selected indexes like the equitable treat score of fractional skill score) obtained from the past verification statistics, can be provided. In this way it possible to contrast the computed EPE probability (event yes/no) against the probability of precipitation exceeding the EPE threshold, while EPE categories probability are confronted against their respective climatological value. This effort towards a greater contextualization of the information allows forecaster a much-informed assessment than simply evaluating the rainfall model output.

Appendix A

Appendix

A.1 Table of Warning Areas thresholds

Cod_DPC	OrogFlag	Area [km ²]	99° [mm]	90° [mm]	70° [mm]
Emil-A	1	2027	46.2	19.5	10.9
Emil-B	0	2409	45.4	18.2	9.4
Emil-C	1	2145	47.5	20.3	11.2
Emil-D	0	4757	36.7	15.8	9
Emil-E	1	3085	45.6	19.6	10.7
Emil-F	0	2384	34.7	16	8.9
Emil-G	1	2672	55.5	23.2	11.9
Emil-H	0	2974	42.4	19.7	10.5
Friu-A	1	2121	84.1	30.9	16
Friu-B	1	2989	87.1	36.4	17
Friu-C	0	2513	58.8	28.2	15.4
Friu-D	0	240	52.2	24	14
Ligu-A	1	1685	70.5	23.4	10.9
Ligu-B	1	796	79.5	31.2	14.9
Ligu-C	1	1459	79.9	31.3	15.9
Ligu-D	1	857	79.3	28.2	13.4
Ligu-E	1	619	88.6	32.3	15.8
Lomb-01	1	464	71.8	26.3	13.2
Lomb-02	1	1594	54.9	22.6	11.5
Lomb-03	1	1137	42.8	16.2	8.5
Lomb-04	1	773	68.6	31.4	16
Lomb-05	1	1743	63.7	28.7	15.3
Lomb-06	1	1405	61.1	26.2	13.9
Lomb-07	1	1429	49.7	20.9	11.3
Lomb-08	1	2284	48	21.8	12
Lomb-09	0	2305	52	24.1	13.1
Lomb-10	0	1608	44.1	20.7	11.5
Lomb-11	0	3191	39.5	17.5	10
Lomb-12	0	3083	40.1	19.6	10.8
Lomb-13	0	2059	36.2	16.4	9
Lomb-14	0	788	44.4	18.9	10.6
Mar-01	1	1221	47.9	19.8	11.1
Mar-02	0	1441	41.7	17.7	9.8
Mar-03	1	1216	43.2	18.4	10.4
Mar-04	0	1909	43.1	17.3	9.6
Mar-05	1	1562	43.7	17.9	10.2
Mar-06	0	2052	41.6	16.5	9.1
Piem-A	1	2383	80	28	12.3
Piem-B	1	1528	79.3	29.4	13.4
Piem-C	1	2081	60.6	21.8	10.2
Piem-D	1	1819	49	17.4	8.6
Piem-E	1	2303	50.7	19.8	9.9
Piem-F	1	2026	55.1	21.1	10.6
Piem-G	0	3078	47.2	20.5	10.7
Piem-H	0	995	53.3	21.5	11.4
Piem-I	0	4252	52	22.8	12.1
Piem-L	0	3198	50.6	22.3	11.3
Piem-M	0	1725	51.9	21.5	11
Tosc-A1	1	826	52.4	21.1	12
Tosc-A2	1	869	43	18.9	11
Tosc-A3	0	770	42.1	18.9	10.7
Tosc-A4	0	1429	45.8	21	12.3
Tosc-A5	0	1418	40.6	18.5	10.7
Tosc-A6	0	410	47	21.4	12.5
Tosc-B	1	816	52.9	24.9	13.7
Tosc-C	0	1536	35.2	16.1	9.6

Tosc-E1	0	2089	43.7	19.5	11.2
Tosc-E2	0	297	43.8	19.3	10.9
Tosc-E3	0	469	43.8	19.6	10.8
Tosc-F1	0	1460	49.6	20.2	11.1
Tosc-F2	0	749	50.4	19.3	10.4
Tosc-I	1	264	51	20.5	11.4
Tosc-L	1	973	76.3	32.1	16.3
Tosc-M	1	961	48.1	21.9	12.5
Tosc-O1	0	1962	41.1	17.5	10.3
Tosc-O2	0	1551	41.3	17.8	10.4
Tosc-O3	0	474	48.3	18.5	10.1
Tosc-R1	1	193	84.9	32.8	16.9
Tosc-R2	1	535	52.5	22.4	12.8
Tosc-S1	1	1355	77.4	33.2	16.3
Tosc-S2	1	397	64.6	29.4	16.3
Tosc-S3	0	192	57	23.6	13.6
Tosc-T	1	673	47.7	20.3	11.5
Tosc-V	1	318	73.5	31.4	16.7
Tren-A	1	7398	36.6	15.5	8.5
Tren-B	1	6207	54.2	21.4	11.2
Umbr-A	1	1909	38.7	17.1	10.1
Umbr-B	0	1186	42.2	18.2	10.9
Umbr-C	1	2044	38.3	17.4	10.2
Umbr-D	1	1467	40.1	18.6	10.6
Umbr-E	0	1054	36.6	16.2	9.5
Umbr-F	0	805	44.4	17.7	10.1
VDAo-A	1	798	39	14.8	8
VDAo-B	1	838	64.5	21.5	10.1
VDAo-C	1	546	44.3	16	8.3
VDAo-D	1	1078	41.2	18	10.2
Vene-A	1	2313	62.5	23.2	11.7
Vene-B	1	2674	64.4	26.3	13.9
Vene-C	1	1728	44.6	21.8	12.1
Vene-D	0	2761	34.9	16.7	9.3
Vene-E	0	3484	42.5	19.5	10.9
Vene-F	0	2279	49.3	21.6	11.8
Vene-G	0	1075	53.8	24	12.9
Vene-H	1	2092	71	27.4	14

Table S1: Table containing warning area codes, presence of significant orography (orogflag), areal extension and high percentile [mm in 24h] daily precipitation calculated only on wet days (average precipitation over warning areas ≥ 1 mm) in the period 1979-2015.

A.2 List of benchmark cases

ref	EPE date	Main Process	Taudmax	Capedmax	lvte	lvtn	Θ_{e850}	TCWV	Cat_STA	Cat_Kmeans6
1	19821108	WCB/orog	1.1	67.0	57.4	261.0	306.1	20.1	1	2
2	20091223	WCB/orog	2.1	114.8	250.0	208.3	302.6	17.5	1	1
3	20140118	WCB/orog	1.6	80.7	163.5	187.3	302.0	15.9	1	1
4	20150205	WCB/orog	2.6	180.6	-97.5	59.6	296.0	11.7	2	1
5	20171211	WCB/orog	1.8	79.0	269.0	302.0	305.0	18.3	1	1
6	19941105	WCB/orog/MCS	3.3	312.1	-56.1	244.2	313.9	21.1	2	2
7	20111025	WCB/orog/MCS	2.4	261.8	94.1	248.8	309.8	21.8	2	2
8	20111104	WCB/orog/MCS	4.2	289.7	69.4	241.9	314.3	23.2	2	2
9	20121110	WCB/orog/MCS	4.5	284.7	160.6	221.3	309.4	21.8	2	2
10	20121026	WCB/orog/MCS	3.8	474.6	100.8	162.6	315.1	22.4	2	2
11	19870825	Cyclone/MCS	15.8	1320.6	95.5	338.9	329.1	30.9	3	3
12	19960619	Isolated MCS	19.8	558.5	127.3	-3.4	321.1	21.0	3	3
13	20140614	MCS	26.3	1787.9	11.2	-46.3	326.6	26.8	3	3
14	20140920	MCS	19.0	1539.7	158.4	151.7	328.4	30.4	3	3
15	20150914	MCS	16.4	1330.7	121.1	203.6	323.2	27.4	3	3

Table S2: List of benchmark extreme precipitation events. Columns indicate a subjective description of the main processes involved, representative predictor values, and categorizations obtained with the two methods. Each of these selected events have been described either in a peer reviewed article (indicated when available), or in technical reports from Italian meteo-hydrological administrations (in Italian). The separation indicated with the background colour reflects the different categories deduced by the description of the events in the literature cited below. The red numbers in the objective categorization columns indicate cases wrongly assigned by STA and K-means methods. Note that the scientific literature has focused on cases with embedded convection while fewer winter EPEs have been investigated. Case n.5 is outside the 1979-2015 period of the present study. However, it is included as a Cat1 benchmark case since it is a clear and documented recent example of EPE attributable to orographically enhanced precipitation.

References for benchmark case studies description

- ¹Annale Idrologico 1982- Parte I Ufficio Idrografico di Parma. Available at: <https://www.arpae.it/cms3/documenti/ cerca doc/meteo/annali idro/annali apat/annali parte i/1973-1987/annale parte i - 1982 - compresso 150 dpi.pdf>
- ²Centro Funzionale Regione Toscana, Report sull'evento alluvionale del 24-25 Dicembre 2009. Available at http://www.cfr.toscana.it/supports/download/eventi/report_evento_alluvionale_serchio_2009-12-25.pdf
- ³ARPAE-SIMC – Regione Emilia-Romagna 2014: Rapporto 2014/02 Evento dal 17 al 19 gennaio 2014. Available at: https://www.arpae.it/cms3/documenti/ cerca doc/meteo/radar/rapporti/rapporto_meteo_20140117-19.pdf
- ⁴ARPAE-SIMC – Regione Emilia-Romagna 2014: Rapporto 2014/02 Evento dal 17 al 19 gennaio 2014. Available at: https://www.arpae.it/cms3/documenti/ cerca doc/meteo/radar/rapporti/rapporto_meteo_20150205-06.pdf
- ⁵ARPAE-SIMC – Regione Emilia-Romagna 2017: Relazione dell'evento meteo dal 8 al 12 dicembre 2017: Available at: https://www.arpae.it/cms3/documenti/ cerca doc/meteo/radar/rapporti/Rapporto_meteo_20171208-12.pdf
- ⁶Cassardo, C., N. Loglisci, D. Gandini, M. W. Qian, G. Y. Niu, P. Ramieri, R. Pelosini, and A. Longhetto, 2002a: The flood of November 1994 in Piedmont, Italy: A quantitative analysis and simulation. *Hydrol. Processes*, **16**, 1275–1299
- ⁷A. Buzzi, S. Davolio, P. Malguzzi, O. Drofa, D. Mastrangelo, 2013: Heavy rainfall episodes over Liguria of autumn 2011: numerical forecasting experiments. *Nat. Hazards Earth Syst. Sci. Discuss.*, 1 (2013), pp. 7093-7135
- ⁷Rebora N., L. Molini, E. Casella, A. Comellas, E. Fiori, F. Pignone, F. Siccardi, F. Silvestro, S. Tanelli, A. Parodi, 2013: Extreme rainfall in the Mediterranean: what can we learn from observations? *J. Hydrometeorol.*, 14, pp. 906-922
- ⁸Fiori E., A. Comellas, L. Molini, N. Rebora, F. Siccardi, D.J. Gochis, S. Tanelli, A. Parodi, 2014: Analysis and hindcast simulations of an extreme rainfall event in the Mediterranean area: the Genoa 2011 case. *Atmos. Res.*, 138 (2014), pp. 13-29
- ⁹Centro Funzionale Regione Toscana, Report eventi meteo-idrologici 10-12 Novembre 2012. Available at http://www.cfr.toscana.it/supports/download/eventi/report_evento_alluvionale_10-11-12_novembre_2012.pdf
- ¹⁰Nuissier, O., Marsigli, C., Vincendon, B., Hally, A., Bouttier, F., Montani, A. and Paccagnella, T., 2016: Evaluation of two convection-permitting ensemble systems in the HyMeX Special Observation Period (SOP1) framework. *Q.J.R. Meteorol. Soc.*, 142: 404–418. doi:10.1002/qj.2859
- ¹¹Isotta, F. A., Frei, C., Weigluni, V., Perčec Tadić, M., Lassègues, P., Rudolf, B., Pavan, V., Cacciamani, C., Antolini, G., Ratto, S. M., Munari, M., Micheletti, S., Bonati, V., Lussana, C., Ronchi, C., Panettieri, E., Marigo, G. and Vertačnik, G. 2014: The climate of daily precipitation in the Alps: development and analysis of a high-resolution grid dataset from pan-Alpine rain-gauge data. *Int. J. Climatol.*, 34:1657–1675. doi:10.1002/joc.3794.
- ¹²Cacciamani C, Cesari D, Grazzini F, Paccagnella T, Pantone M. 2000. Numerical simulation of intense precipitation events south of the Alps: sensitivity to initial conditions and horizontal resolution. *Meteorology and Atmospheric Physics* 72(2–4): 147–159.
- ¹³ARPAE-SIMC – Regione Emilia-Romagna 2014: [Rapporto 2014/13 dell'evento dal 13 al 15 giugno 2014](https://www.arpae.it/dettaglio_documento.asp?id=5169&idlivello=64). Available at : https://www.arpae.it/dettaglio_documento.asp?id=5169&idlivello=64
- ¹⁴ARPAE-SIMC – Regione Emilia-Romagna 2014: Rapporto sull'evento alluvionale del 20 settembre 2014. Available at: https://www.arpae.it/cms3/documenti/ cerca doc/meteo/radar/rapporti/Rapporto_meteo_20140920.pdf
- ¹⁵ARPAE-SIMC – Regione Emilia-Romagna 2015: Rapporto sull'evento alluvionale del 14 settembre 2015. Available at: https://ambiente.regione.emilia-romagna.it/geologia/archivio_pdf/dissesto-idrogeologico/rapporto-evento-alluvionale-14-09-2015

A.3 List of Abbreviations

Acronyms

ARCIS Archivio Climatologico per l'Italia centro-Settentrionale, Climatological Archive for Central-Northern Italy.

CAPE Convective Available Potential Energy.

CIN Convection Inhibition.

E Rossby wave packet amplitude.

ECMWF European Centre for Medium-Range Weather Forecasts.

EPE Extreme Precipitation Events.

IFS ECMWF Integrated Forecast System.

IVT Integrated water Vapour Transport.

IVT_n Integrated water Vapour Transport Meridional component.

MCS Mesoscale Convective System.

NPS Normalised Precipitation Spread.

PPI Potential Predictability Index.

PV Potential Vorticity.

RWPs Rossby Wave Packets.

SIL Silhouette score.

Tau Convective adjustment timescale.

TCWV Total Column Water Vapour.

WA Warning Areas used by the Italian Department of Civil Protection.

Bibliography

- Bachmann, K., C. Keil, G. C. Craig, M. Weissmann, and C. A. Welzbacher, 2020: Predictability of deep convection in idealized and operational forecasts: Effects of radar data assimilation, orography, and synoptic weather regime. *Monthly Weather Review*, **148** (1), 63–81, doi:10.1175/MWR-D-19-0045.1, URL <https://doi.org/10.1175/MWR-D-19->.
- Bauer, P., A. Thorpe, and G. Brunet, 2015: The quiet revolution of numerical weather prediction. Nature Publishing Group, URL <https://www.nature.com/articles/nature14956>, 47–55 pp., doi:10.1038/nature14956.
- Bluestein, H. B. and M. H. Jain, 1985: Formation of Mesoscale Lines of Precipitation: Severe Squall Lines in Oklahoma during the Spring. *Journal of the Atmospheric Sciences*, **42** (16), 1711–1732, doi:10.1175/1520-0469(1985)042<1711:fomlop>2.0.co;2.
- Boers, N., B. Goswami, A. Rheinwalt, B. Bookhagen, B. Hoskins, and J. Kurths, 2019: Complex networks reveal global pattern of extreme-rainfall teleconnections. *Nature*, **566** (7744), 373–377, doi:10.1038/s41586-018-0872-x, URL <http://dx.doi.org/10.1038/s41586-018-0872-x>.
- Bougeault, P., P. Binder, A. Buzzi, R. Dirks, R. Houze, J. Kuettner, R. B. Smith, R. Steinacker, and H. Volkert, 2001: The MAP Special Observing Period. *Bulletin of the American Meteorological Society*, **82** (3), 433–462, doi:10.1175/1520-0477(2001)082<0433:TMSOP>2.3.CO;2.
- Buzzi, A., N. Tartaglione, and P. Malguzzi, 1998: Numerical simulations of the 1994 piedmont flood: Role of orography and moist processes. *Monthly Weather Review*, **126** (9), 2369–2383, doi:10.1175/1520-0493(1998)126<2369:NSOTPF>2.0.CO;2.
- Chang, E. K. M., 1993: Downstream Development of Baroclinic Waves As Inferred from Regression Analysis. *Journal of the Atmospheric Sciences*, **50** (13), 2038–2053, doi:10.1175/1520-0469(1993)050<2038:ddobwa>2.0.co;2.
- Charney, J., 1955: The Use of the Primitive Equations of Motion in Numerical Prediction. *Tellus*, **7** (1), 22–26, doi:10.3402/tellusa.v7i1.8772, URL <https://www.tandfonline.com/action/journalInformation?journalCode=zalb20>.

- Davis, C. A., 1992: Piecewise Potential Vorticity Inversion. *Journal of the Atmospheric Sciences*, **49** (16), 1397–1411, doi:10.1175/1520-0469(1992)049<1397:ppvi>2.0.co;2.
- Dee, D. P., S. M. Uppala, A. J. Simmons, P. Berrisford, P. Poli, S. Kobayashi, U. Andrae, M. A. Balmaseda, G. Balsamo, P. Bauer, P. Bechtold, A. C. Beljaars, L. van de Berg, J. Bidlot, N. Bormann, C. Delsol, R. Dragani, M. Fuentes, A. J. Geer, L. Haimberger, S. B. Healy, H. Hersbach, E. V. Hólm, L. Isaksen, P. Kållberg, M. Köhler, M. Matricardi, A. P. McNally, B. M. Monge-Sanz, J. J. Morcrette, B. K. Park, C. Peubey, P. de Rosnay, C. Tavolato, J. N. Thépaut, and F. Vitart, 2011: The ERA-Interim reanalysis: Configuration and performance of the data assimilation system. *Quarterly Journal of the Royal Meteorological Society*, **137** (656), 553–597, doi:10.1002/qj.828.
- Delrieu, G., V. Ducrocq, E. Gaume, J. Nicol, O. Payrastre, E. Yates, P. E. Kirstetter, H. Andrieu, P. A. Ayrál, C. Bouvier, J. D. Creutin, M. Livet, S. Anquetin, M. Lang, L. Neppel, C. Obled, J. Parent-Du-Châtelet, G. M. Saulnier, A. Walpersdorf, and W. Wobrock, 2005: The catastrophic flash-flood event of 8-9 September 2002 in the Gard Region, France: A first case study for the Cévennes-Vivarais Mediterranean Hydrometeorological Observatory. *Journal of Hydrometeorology*, **6** (1), 34–52, doi:10.1175/JHM-400.1.
- Done, J. M., G. C. Craig, S. L. Gray, P. A. Clark, and M. E. B. Gray, 2006: Mesoscale simulations of organized convection: Importance of convective equilibrium. *Quarterly Journal of the Royal Meteorological Society*, **132** (616), 737–756, doi:10.1256/qj.04.84, URL <http://doi.wiley.com/10.1256/qj.04.84>.
- Ducrocq, V., I. Braud, S. Davolio, R. Ferretti, C. Flamant, A. Jansa, N. Kalthoff, E. Richard, I. Taupier-Letage, P. A. Ayrál, S. Belamari, A. Berne, M. Borga, B. Boudevillain, O. Bock, J. L. Boichard, M. N. Bouin, O. Bousquet, C. Bouvier, J. Chiggiano, D. Cimini, U. Corsmeier, L. Coppola, P. Cocquerez, E. Defer, J. Delanoë, P. Di Girolamo, A. Doerenbecher, P. Drobinski, Y. Dufournet, N. Fourrié, J. J. Gourley, L. Labatut, D. Lambert, J. Le Coz, F. S. Marzano, G. Molinié, A. Montani, G. Nord, M. Nuret, K. Ramage, W. Rison, O. Roussot, F. Said, A. Schwarzenboeck, P. Testor, J. Van Baelen, B. Vincendon, M. Aran, and J. Tamayo, 2014: HyMeX-SOP1: The field campaign dedicated to heavy precipitation and flash flooding in the northwestern mediterranean. *Bulletin of the American Meteorological Society*, **95** (7), 1083–1100, doi:10.1175/BAMS-D-12-00244.1.
- Duffourg, F. and V. Ducrocq, 2013: Assessment of the water supply to Mediterranean heavy precipitation: A method based on finely designed water budgets. *Atmospheric Science Letters*, **14** (3), 133–138, doi:10.1002/asl2.429, URL <http://doi.wiley.com/10.1002/asl2.429>.
- Duffourg, F., K.-O. Lee, V. Ducrocq, C. Flamant, P. Chazette, and P. Di Girolamo, 2018: Role of moisture patterns in the backbuilding formation of HyMeX IOP13 heavy precipitation systems. *Quarterly Journal of the Royal Meteorological Society*, **144** (710), 291–303, doi:10.1002/qj.3201, URL <http://doi.wiley.com/10.1002/qj.3201>.

- European Environment Agency, 2017: Economic Losses from climate-related extremes in Europe. Tech. rep. URL <https://www.eea.europa.eu/data-and-maps/indicators/direct-losses-from-weather-disasters-3/assessment-2>.
- Fragkoulidis, G., V. Wirth, P. Bossmann, and A. Fink, 2018: Linking Northern Hemisphere temperature extremes to Rossby wave packets. *Quarterly Journal of the Royal Meteorological Society*, **144** (711), doi:10.1002/qj.3228.
- Froude, L. S. R., L. Bengtsson, and K. I. Hodges, 2013: Atmospheric predictability revisited. *Tellus A: Dynamic Meteorology and Oceanography*, **65** (1), 19022, doi:10.3402/tellusa.v65i0.19022, URL <https://www.tandfonline.com/doi/full/10.3402/tellusa.v65i0.19022>.
- Grazzini, F., 2007: Predictability of a large-scale flow conducive to extreme precipitation over the western Alps. *Meteorology and Atmospheric Physics*, **95** (3-4), 123–138, doi:10.1007/s00703-006-0205-8, URL <http://link.springer.com/10.1007/s00703-006-0205-8>.
- Grazzini, F. and L. Isaksen, 2002: North America Increments. OD/RD Memo. Tech. rep., ECMWF, 40 pp., Reading.
- Grazzini, F. and G. Van der Grijn, 2003: Central European floods during summer 2002. *ECMWF Newsletter*, **96** (Winter 2002/2003), URL <https://www.ecmwf.int/sites/default/files/elibrary/2002/14628-newsletter-no96-winter-200203.pdf>.
- Grazzini, F. and F. Vitart, 2015: Atmospheric predictability and Rossby wave packets. *Quarterly Journal of the Royal Meteorological Society*, **141** (692), doi:10.1002/qj.2564.
- Harris, F. J., 1978: On the use of windows for harmonic analysis with the discrete Fourier transform. *Proceedings of the Institute of Electrical and Electronic Engineers*.
- Hersbach, H., B. Bell, P. Berrisford, S. Hirahara, A. Horányi, J. Muñoz-Sabater, J. Nicolas, C. Peubey, R. Radu, D. Schepers, A. Simmons, C. Soci, S. Abdalla, X. Abellan, G. Balsamo, P. Bechtold, G. Biavati, J. Bidlot, M. Bonavita, G. Chiara, P. Dahlgren, D. Dee, M. Diamantakis, R. Dragani, J. Flemming, R. Forbes, M. Fuentes, A. Geer, L. Haimberger, S. Healy, R. J. Hogan, E. Hólm, M. Janisková, S. Keeley, P. Laloyaux, P. Lopez, C. Lupu, G. Radnoti, P. Rosnay, I. Rozum, F. Vamborg, S. Villaume, and J. Thépaut, 2020: The ERA5 Global Reanalysis. *Quarterly Journal of the Royal Meteorological Society*, qj.3803, doi:10.1002/qj.3803, URL <https://onlinelibrary.wiley.com/doi/abs/10.1002/qj.3803>.
- Hewson, T. D. and F. M. Pilloso, 2020: A new low-cost technique improves weather forecasts across the world. *arXiv*, URL <http://arxiv.org/abs/2003.14397>.
- Hohenegger, C., D. Lüthi, and C. Schär, 2006: Predictability mysteries in cloud-resolving models. *Monthly Weather Review*, **134** (8), 2095–2107, doi:10.1175/MWR3176.1.

- Holton, J. R. and G. J. Hakim, 2012: *An introduction to dynamic meteorology: Fifth edition*, Vol. 9780123848. 1–532 pp., doi:10.1016/C2009-0-63394-8.
- Hoskins, B. J., M. E. McIntyre, and A. W. Robertson, 1985: On the use and significance of isentropic potential vorticity maps. *Quarterly Journal of the Royal Meteorological Society*, **111** (470), 877–946, doi:10.1002/qj.49711147002.
- IPCC, 2014: Summary for Policymakers. *Climate Change 2013 - The Physical Science Basis*, Intergovernmental Panel on Climate Change, Ed., Cambridge University Press, Cambridge, 1–30, doi:10.1017/CBO9781107415324.004, URL https://www.cambridge.org/core/product/identifier/CB09781107415324A009/type/book_part.
- Isotta, F. A., C. Frei, V. Weigluni, M. Perčec Tadić, P. Lassègues, B. Rudolf, V. Pavan, C. Cacciamani, G. Antolini, S. M. Ratto, M. Munari, S. Micheletti, V. Bonati, C. Lussana, C. Ronchi, E. Panettieri, G. Marigo, and G. Vertačnik, 2014: The climate of daily precipitation in the Alps: Development and analysis of a high-resolution grid dataset from pan-Alpine rain-gauge data. *International Journal of Climatology*, **34** (5), 1657–1675, doi:10.1002/joc.3794.
- Jansa, A., P. Alpert, P. Arbogast, A. Buzzi, B. Ivancan-Picek, V. Kotroni, M. C. Llasat, C. Ramis, E. Richard, R. Romero, and A. Speranza, 2014: MEDEX: a general overview. *Natural Hazards and Earth System Sciences*, **14** (8), 1965–1984, doi:10.5194/nhess-14-1965-2014, URL <https://www.nat-hazards-earth-syst-sci.net/14/1965/2014/>.
- Keil, C., L. Chabert, O. Nuissier, and L. Raynaud, 2020: Dependence of predictability of precipitation in the northwestern Mediterranean coastal region on the strength of synoptic control. *Atmospheric Chemistry and Physics*, **20** (24), 15 851–15 865, doi:10.5194/acp-20-15851-2020, URL <https://acp.copernicus.org/articles/20/15851/2020/>.
- Keil, C., F. Heinlein, and G. C. Craig, 2014: The convective adjustment time-scale as indicator of predictability of convective precipitation. *Quarterly Journal of the Royal Meteorological Society*, **140** (679), 480–490, doi:10.1002/qj.2143, URL <http://doi.wiley.com/10.1002/qj.2143>.
- Kober, K., G. C. Craig, and C. Keil, 2014: Aspects of short-term probabilistic blending in different weather regimes. *Quarterly Journal of the Royal Meteorological Society*, **140** (681), 1179–1188, doi:10.1002/qj.2220.
- Krichak, S. O., J. Barkan, J. S. Breitgand, S. Gualdi, and S. B. Feldstein, 2015: The role of the export of tropical moisture into midlatitudes for extreme precipitation events in the Mediterranean region. *Theoretical and Applied Climatology*, **121** (3-4), 499–515, doi:10.1007/s00704-014-1244-6.

- Lavers, D. A., F. Pappenberger, and E. Zsoter, 2014: Extending medium-range predictability of extreme hydrological events in Europe. *Nature Communications*, **5**, 1–7, doi:10.1038/ncomms6382, URL <http://dx.doi.org/10.1038/ncomms6382>.
- Lavers, D. A. and G. Villarini, 2015: The relationship between daily European precipitation and measures of atmospheric water vapour transport. *International Journal of Climatology*, **35** (8), 2187–2192, doi:10.1002/joc.4119.
- Lorenz, E. N., 1963: Deterministic Nonperiodic Flow. *Journal of the Atmospheric Sciences*, **20** (2), 130–141, doi:10.1175/1520-0469(1963)020<0130:dnf>2.0.co;2, URL https://journals.ametsoc.org/view/journals/atasc/20/2/1520-0469_1963_020_0130_dnf_2_0_co_2.xml.
- Lorenz, E. N., 1969a: The predictability of a flow which possesses many scales of motion. *Tellus*, **21** (3), 289–307, doi:10.1111/j.2153-3490.1969.tb00444.x, URL <http://tellusa.net/index.php/tellusa/article/view/10086>.
- Lorenz, E. N., 1969b: Three Approaches to Atmospheric Predictability. *Bulletin of the American Meteorological Society*, **50** (5), 345–349, URL <http://www.jstor.org/stable/26252553>.
- Loriaux, J. M., G. Lenderink, and A. Pier Siebesma, 2017: Large-scale controls on extreme precipitation. *Journal of Climate*, **30** (3), 955–968, doi:10.1175/JCLI-D-16-0381.1, URL http://journals.ametsoc.org/jcli/article-pdf/30/3/955/4671277/jcli-d-16-0381_1.pdf.
- Martius, O., C. Schwierz, and H. C. Davies, 2008: Far-upstream precursors of heavy precipitation events on the Alpine south-side. *Quarterly Journal of the Royal Meteorological Society*, **134** (631), 417–428, doi:10.1002/qj.229, URL <http://doi.wiley.com/10.1002/qj.229>.
- Massacand, A. C., H. Wernli, and H. C. Davies, 1998: Heavy precipitation on the Alpine southside : An upper-level precursor. *Geophysical Research Letters*, **25** (9), 1435–1438, doi:10.1029/98GL50869.
- Messori, G., R. Caballero, F. Bouchet, D. Faranda, R. Grotjahn, N. Harnik, S. Jewson, J. G. Pinto, G. Rivière, T. Woollings, and P. Yiou, 2018: An interdisciplinary approach to the study of extreme weather events: Large-scale atmospheric controls and insights from dynamical systems theory and statistical mechanics. *Bulletin of the American Meteorological Society*, **99** (5), ES81–ES85, doi:10.1175/BAMS-D-17-0296.1.
- Molini, L., A. Parodi, N. Rebora, and G. C. Craig, 2011: Classifying severe rainfall events over Italy by hydrometeorological and dynamical criteria. *Quarterly Journal of the Royal Meteorological Society*, **137** (654), 148–154, doi:10.1002/qj.741.

- Nuissier, O., B. Joly, A. Joly, V. Ducrocq, and P. Arbogast, 2011: A statistical downscaling to identify the large-scale circulation patterns associated with heavy precipitation events over southern France. *Quarterly Journal of the Royal Meteorological Society*, **137** (660), 1812–1827, doi:10.1002/qj.866, URL <http://doi.wiley.com/10.1002/qj.866>.
- Orlanski, I. and J. P. Sheldon, 1995: Stages in the energetics of baroclinic systems. *Tellus, Series A*, **47 A** (5-1), 605–628, doi:10.3402/tellusa.v47i5.11553.
- Paprotny, D., A. Sebastian, O. Morales-Nápoles, and S. N. Jonkman, 2018: Trends in flood losses in Europe over the past 150 years. *Nature Communications*, **9** (1), 1–12, doi:10.1038/s41467-018-04253-1.
- Parsons, D. B., S. P. Lillo, C. P. Rattray, P. Bechtold, M. J. Rodwell, and C. M. Bruce, 2019: The role of continental mesoscale convective systems in forecast busts within global weather prediction systems. *Atmosphere*, **10** (11), doi:10.3390/atmos10110681.
- Pavan, V., G. Antolini, R. Barbiero, N. Berni, F. Brunier, C. Cacciamani, A. Cagnati, O. Cazzuli, A. Cicogna, C. De Luigi, E. Di Carlo, M. Francioni, L. Maraldo, G. Marigo, S. Micheletti, L. Onorato, E. Panettieri, U. Pellegrini, R. Pelosini, D. Piccinini, S. Ratto, C. Ronchi, L. Rusca, S. Sofia, M. Stelluti, R. Tomozeiu, and T. Torrigiani Malaspina, 2019: High resolution climate precipitation analysis for north-central Italy, 1961–2015. *Climate Dynamics*, **52** (5-6), 3435–3453, doi:10.1007/s00382-018-4337-6.
- Pedregosa, F., G. Varoquaux, A. Gramfort, V. Michel, B. Thirion, O. Grisel, M. Blondel, P. Prettenhofer, R. Weiss, V. Dubourg, J. Vanderplas, A. Passos, D. Cournapeau, M. Brucher, M. Perrot, and Duchesnay, 2011: Scikit-learn: Machine Learning in Python. *Journal of Machine Learning Research*, **12** (85), 2825–2830, URL <http://jmlr.org/papers/v12/pedregosa11a.html>.
- Persson, A., 2017: The story of the hovmöller diagram: An (almost) eyewitness account. American Meteorological Society, 949–957 pp., doi:10.1175/BAMS-D-15-00234.1.
- Piaget, N., P. Froidevaux, P. Giannakaki, F. Gierth, O. Martius, M. Riemer, G. Wolf, and C. M. Grams, 2015: Dynamics of a local Alpine flooding event in October 2011: Moisture source and large-scale circulation. *Quarterly Journal of the Royal Meteorological Society*, **141** (690), 1922–1937, doi:10.1002/qj.2496.
- Plaut, G. and E. Simonnet, 2001: Large-scale circulation classification, weather regimes, and local climate over France, the Alps and Western Europe. *Climate Research*, **17** (3 SPECIAL 9), 303–324, doi:10.3354/cr017303, URL <http://www.int-res.com/abstracts/cr/v17/n3/p303-324/>.
- Poletti, M. L., A. Parodi, and B. Turato, 2017: Severe hydrometeorological events in Liguria region: calibration and validation of a meteorological indices-based forecasting operational tool. *Meteorological Applications*, **24** (4), 560–570, doi:10.1002/met.1653, URL <http://doi.wiley.com/10.1002/met.1653>.

- Rebora, N., L. Molini, E. Casella, A. Comellas, E. Fiori, F. Pignone, F. Siccardi, F. Silvestro, S. Tanelli, and A. Parodi, 2013: Extreme rainfall in the mediterranean: What can we learn from observations. *Journal of Hydrometeorology*, **14** (3), 906–922, doi:10.1175/JHM-D-12-083.1.
- Rezaeian, M., A. R. Mohebalhojeh, F. Ahmadi-Givi, and M. Nasr-Esfahany, 2016: A wave-activity view of the relation between the Mediterranean storm track and the North Atlantic Oscillation in winter. *Quarterly Journal of the Royal Meteorological Society*, **142** (697), 1662–1671, doi:10.1002/qj.2760, URL <http://doi.wiley.com/10.1002/qj.2760>.
- Rodwell, M., D. Richardson, and T. Hewson, 2010: A new equitable score suitable for verifying precipitation in NWP. (615), 35, doi:10.21957/h886wj14, URL <https://www.ecmwf.int/node/11988>.
- Rodwell, M. J., L. Magnusson, P. Bauer, P. Bechtold, M. Bonavita, C. Cardinali, M. Diamantakis, P. Earnshaw, A. Garcia-Mendez, L. Isaksen, E. Källén, D. Klocke, P. Lopez, T. McNally, A. Persson, F. Prates, and N. Wedi, 2013: Characteristics of occasional poor medium-range weather forecasts for Europe. *Bulletin of the American Meteorological Society*, **94** (9), 1393–1405, doi:10.1175/BAMS-D-12-00099.1.
- Romero, R., C. A. Doswell, and C. Ramis, 2000: Mesoscale Numerical Study of Two Cases of Long-Lived Quasi-Stationary Convective Systems over Eastern Spain. *Monthly Weather Review*, **128** (11), 3731–3751, doi:10.1175/1520-0493(2001)129<3731:mnsotc>2.0.co;2.
- Sénési, S., P. Bougeault, J.-L. Chèze, P. Cosentino, and R.-M. Thepenier, 1996: The Vaison-La-Romaine Flash Flood: Mesoscale Analysis and Predictability Issues. *Weather and Forecasting*, **11** (4), 417–442, doi:10.1175/1520-0434(1996)011<0417:tvlrff>2.0.co;2.
- Sodemann, H. and E. Zubler, 2010: Seasonal and inter-annual variability of the moisture sources for alpine precipitation during 1995–2002. *International Journal of Climatology*, **30** (7), 947–961, doi:10.1002/joc.1932, URL <http://doi.wiley.com/10.1002/joc.1932>.
- Teubler, F. and M. Riemer, 2016: Dynamics of Rossby wave packets in a quantitative potential vorticity-potential temperature framework. *Journal of the Atmospheric Sciences*, **73** (3), 1063–1081, doi:10.1175/JAS-D-15-0162.1.
- Teubler, F. and M. Riemer, 2020: Dynamical Evolution of Troughs and Ridges within Rossby Wave Packets: A Composite Study. (Submitted).
- Trigo, I. F., T. D. Davies, and G. R. Bigg, 1999: Objective Climatology of Cyclones in the Mediterranean Region. *Journal of Climate*, **12** (6), 1685–1696, doi:10.1175/1520-0442(1999)012<1685:ococit>2.0.co;2.

- Turato, B., O. Reale, and F. Siccardi, 2004: Water Vapor Sources of the October 2000 Piedmont Flood. doi:10.1175/1525-7541(2004)005<0693:WVSOTO>2.0.CO;2, URL <http://journals.ametsoc.org/doi/pdf/10.1175/1525-7541>.
- Vallis, G. K., 2017: *Atmospheric and oceanic fluid dynamics: Fundamentals and large-scale circulation, second edition*. Cambridge University Press, 1–946 pp., doi:10.1017/9781107588417, URL <https://www.cambridge.org/core/books/atmospheric-and-oceanic-fluid-dynamics/41379BDDC4257CBE11143C466F6428A4>.
- Vitart, F., G. Balsamo, J.-R. Bidlot, S. Lang, I. Tsonevsky, D. Richardson, and M. Alonso-Balmaseda, 2019: Use of ERA5 to Initialize Ensemble Re-forecasts. (841), doi:10.21957/w8i57wuz6, URL <https://www.ecmwf.int/node/18872>.
- Vries, A. J. D., 2020: A global climatological perspective on the importance of Rossby wave breaking and intense moisture transport for extreme precipitation events. *Weather and Climate Dynamics*, (September), URL <https://wcd.copernicus.org/preprints/wcd-2020-44/>.
- Winschall, A., H. Sodemann, S. Pfahl, and H. Wernli, 2014: How important is intensified evaporation for Mediterranean precipitation extremes? *Journal of Geophysical Research: Atmospheres*, **119** (9), 5240–5256, doi:10.1002/2013JD021175, URL <http://doi.wiley.com/10.1002/2013JD021175>.
- Wirth, V., M. Riemer, E. K. Chang, and O. Martius, 2018: Rossby wave packets on the midlatitude waveguide-A review. *Monthly Weather Review*, **146** (7), 1965–2001, doi:10.1175/MWR-D-16-0483.1.
- Zhang, F., Y. Qiang Sun, L. Magnusson, R. Buizza, S. J. Lin, J. H. Chen, and K. Emanuel, 2019: What is the predictability limit of midlatitude weather? *Journal of the Atmospheric Sciences*, **76** (4), 1077–1091, doi:10.1175/JAS-D-18-0269.1, URL www.ametsoc.org/PUBSReuseLicenses.
- Zimin, A. V., I. Szunyogh, D. J. Patil, B. R. Hunt, and E. Ott, 2003: Extracting envelopes of Rossby wave packets. *Monthly Weather Review*, doi:10.1175/1520-0493(2003)131<1011:EEORWP>2.0.CO;2.
- Zimmer, M., G. C. Craig, C. Keil, and H. Wernli, 2011: Classification of precipitation events with a convective response timescale and their forecasting characteristics. *Geophysical Research Letters*, **38** (5), 1–6, doi:10.1029/2010GL046199.

Danksagung (Ringraziamenti)

A scientific contribution, such as a paper and even more a PhD dissertation, is never an individual undertaking but rather a collective one. For this reason, I would start to thank my supervisor George Craig, who enthusiastically supported this research and suggested the right framework to realize this study. The working environment is also important for successful research, and the one that I found in the LS-Craig group was excellent and inclusive. Many thanks to my roommates of A230 (the nosiest room in the Institute) Florian, Yvonne and Philipp for their support and friendship, as well as all the others closer colleagues in the faculty: Christian, Mirjam, Leonhard, Audine, Robert, Matthias, Tobi. While promoting scientific discussions, seminars and mountain trips, and during Covid virtual coffee (sigh...), they contributed to build a team spirit, which is so essential to keep motivation high. On this point, a special thanks goes to Theresa and the Italian-German tandem. With conversations going beyond scientific issues, this initiative added colour and further motivation to the long isolation caused by the pandemic. Many people outside the LMU also need to be mentioned, beginning with my colleagues at ARPAE with whom I carried out this research (Valentina, Gabriele, Tommaso) and especially Sandro Nanni, Carlo Cacciamani and Tiziana Paccagnella, respectively my direct ARPAE manager and the two directors that allowed me to focus my interests here in Munich. The same goes for my colleagues at JGU Mainz Volkmar, Franziska and Georgios for their essential contribution. As special thank to Georgios with whom I have established a great collaboration. Last but not least my family. A mention to my two sons, Giulio and Michele, which have become my "new" colleagues in this last year of home-office, and Giovanna, the real driving force behind this whole adventure. Finally, I am undoubted grateful the UBG Risiko Verein for keep me physically active and overcome mental fatigue, with a typical regenerating weekend mountain trip. Thanks to all !